Chapter 7
He II Heat and Mass Transfer

Chapter 6 emphasized the physics of He II including heat transport in the laminar flow and the turbulent mutual friction regimes. These mechanisms are fundamental to the behavior of He II, although that discussion mostly described idealized behavior. In the present chapter we will build on the fundamental understanding of He II to treat practical heat and mass transfer problems that may occur in He II systems. In doing so, the concepts already developed must be extended into regimes that are more usable in engineering calculations. To be more specific, the emphasis of Chap. 6 has been to understand the interactive mechanisms and the two fluid nature of He II. Thus, of principal concern is the behavior of the transport properties including mainly the normal fluid viscosity μ_n and the turbulent state with the associated mutual friction parameter A_{GM}. Of interest now is to use these concepts in understanding such phenomena as the maximum heat flux, q^*, the maximum energy deposition, ΔE^*, and the corresponding temperature difference, which can be either within the fluid or across a solid-fluid interface. The goal of the present chapter is to establish a connection between the engineering parameters q^*, ΔE^*, and ΔT and the physical properties of the fluid and solid-fluid boundaries. In establishing this connection there are a number of subjects of practical interest which must be addressed. These include steady-state heat transport, transient heat transport, forced flow pressure drop and heat transport, surface Kapitza boundary conductance, and film boiling. Some of these phenomena are also important in pool boiling He I heat transfer, which is the subject of Chap. 5.

Before delving into these individual subjects, it is worth describing, in a general way, the surface heat transfer character of liquid He II. This character in actuality is quite similar qualitatively to that of He I or other conventional fluids, although as we will see the numerical values and physical explanations are considerably different. Figure 7.1 shows a typical steady-state heat transfer curve for a metal surface at the end of a duct containing He II, see Fig. 7.2. As is discussed below, the duct also may contain a temperature difference ($T_m - T_b$). Figure 7.1 is intended only to display the regions of heat transfer. As is demonstrated in what follows, actual numerical values of these regimes are strongly dependent on geometry, temperature, pressure, and surface conditions. That the heat transfer surface is

S.W. Van Sciver, *Helium Cryogenics*, International Cryogenics Monograph Series,
DOI 10.1007/978-1-4419-9979-5_7,

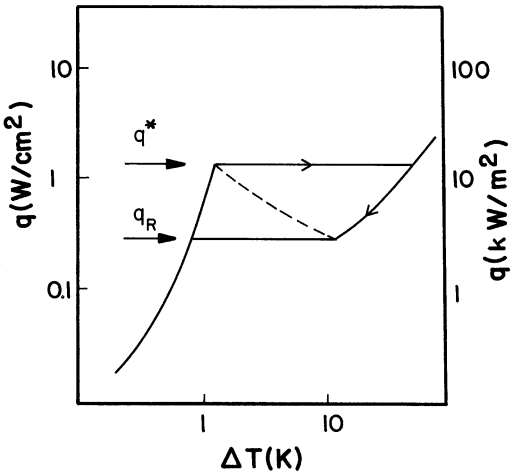

Fig. 7.1 A typical steady-state beat transfer curve for a metal surface at the end of a duct containing He II

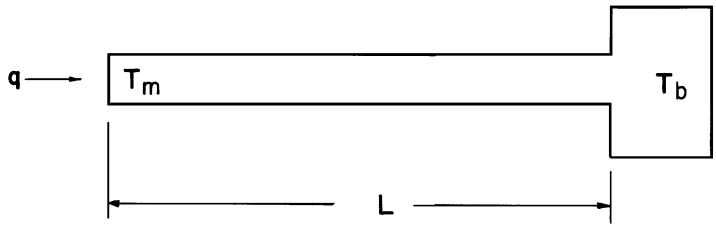

Fig. 7.2 Schematic of a horizontal duct of length L containing He II

located at the end of a channel rather than in an open bath is also important in determining critical values. As we will see, the very high effective thermal conductivity of He II results in a thermal boundary layer that can take on the dimensions of the duct, thus controlling much of the heat transfer process.

For small q up *to* q^*, the surface temperature difference, ΔT_s, is governed by interfacial phenomena having more to do with the character of the solid than that of the liquid helium. This is called the Kapitza regime. In this regime, there is no surface boiling, rather the temperature difference is a result of thermal impedance between the two dissimilar materials, the metal or insulating solid and liquid He II. Also, the maximum heat flux q^* is strongly geometry and helium state dependent and is characterized by the point where the helium adjacent to the interface exceeds the local boiling point. The maximum heat flux is also time dependent, achieving very high values for short-duration heat pulses. Once this maximum is exceeded, the heat transfer transitions to a film boiling process where a film consisting of either He I, vapor, or both blankets the surface. Finally, in some configurations there is

observed a hysteresis in the heat transfer curve exemplified by the requirement to reduce q below q^* in order to return to the Kapitza regime. This process is reasonably well understood in He I and other classical fluids, being described by a hydrodynamic instability which leads to an engineering correlation. However, in He II the problem is more complex and has received less attention, owing to the experimental difficulty of achieving steady state and strong variations with configuration. It is the physical understanding of this heat transfer curve that is the goal of the present chapter. The description is based heavily on the physics of heat transport in He II contained in Chap. 6.

7.1 Steady-State He II Heat Transport in Wide Channels

The first question to ask is: What are the limitations to heat transport in a channel containing He II? Since the heat transport equations for He II have already been developed, it should be straightforward to apply this theory to determine practical heat transfer limitations. In doing so, it is assumed that the heat transport equations can be applied over finite temperature differences simply by taking into consideration the temperature dependence of the fluid properties. Note that He II cannot exist above the λ-transition, 2.177 K at SVP, which at least establishes liquid temperature boundaries to the heat transfer problem. For a channel of finite length L, as shown in Fig. 7.2, subjected to a constant heat flux q, there is a temperature difference established across its length, that is $\Delta T_{He\ II} = T_m - T_b$. In general, this temperature difference occurs because of two loss mechanisms discussed in Chap. 6: (1) the normal fluid viscous interactions with the channel walls and (2) the mutual friction between the two fluid components. We therefore consider here two classes of problems. The first concerns the heat and mass transfer in large systems such as occur in superconducting magnets and particle accelerators. In this case, the channel diameters and heat fluxes are sufficiently large to allow the mutual friction term to dominate the heat flow process. Thus, for this class of problems, the normal fluid viscous contribution to the temperature and pressure gradient can be neglected. The second class of problems which we will discuss subsequently involve heat and mass transfer through very small diameter capillaries or porous media. This heat transfer regime is mostly of interest in space applications and small scale cooling channels such as occur in some high current density magnets. In this latter case, at low heat fluxes, the flow is ideal and the pressure and temperature gradients obey London's equation with viscous flow dominating the normal fluid. At moderate to high heat fluxes, both laminar and turbulent contributions must be included in the analysis. Problems in this regime are the most complex to analyze.

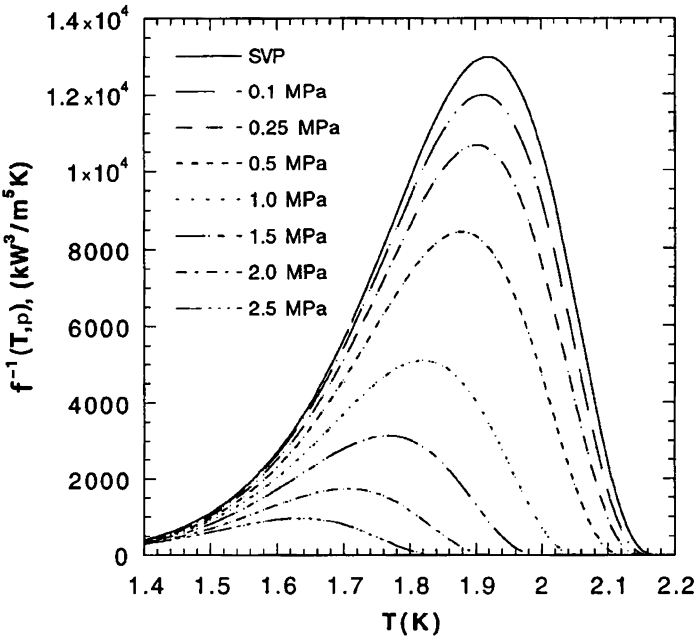

Fig. 7.3 Heat conductivity function for turbulent He II

7.1.1 He II Heat Conductivity Function

For wide channels, the normal fluid viscous term can generally be neglected so that the He II temperature gradient equation (6.101) may be simplified in one dimension as,

$$\frac{dT}{dx} = -f(T, p)q^m \tag{7.1}$$

where we define $f(T, p) = A_{GM}\rho_n/(\rho_s s^4 T^3)$ with A_{GM} being the mutual friction parameter and ρ_n and ρ_s are the normal and superfluid densities, respectively. According to theory $m \sim 3$; however, experimentally m has been shown to vary from about 3 to nearly 4 as the temperature approaches T_λ [1, 2]. A good mean value for practical calculations is to set $m = 3.4$, which is consistent with experiment over the temperature range from 1.7 K to T_λ [3–5]. The physics behind (7.1) is discussed extensively in Sect. 6.5. The quantity $f^{-1}(T, p)$ behaves much like a thermal conductivity in that it is a fluid property that controls the temperature gradient in the presence of a heat flux. It is therefore of interest to understand the variation of $f^{-1}(T, p)$ with state variables. Plotted in Fig. 7.3 is this function as it depends on temperature and pressure between 1.4 K and T_λ and $p =$ SVP and 2.5 MPa for the case where $m = 3$. Note that the temperature dependence is quite strong with a maximum occurring around $T \approx 1.9$ K at SVP. The pressure dependence is weaker.

In the data presented in Fig. 7.3, Vinen's [1] values for the Gorter-Mellink parameter have been used. Furthermore, it has been assumed that $A_{GM} \sim \rho\rho_n^2/\rho^3$ which is based on theory [6]. Then based on an empirical fit to the Gorter-Mellink parameter, it is possible to write an analytic expression for the heat conductivity function,

$$f^{-1}(T,p) = g(T_\lambda)\left[t^{5.7}(1-t^{5.7})\right]^3 \tag{7.2}$$

where $g(T_\lambda) = \rho^2 s_\lambda^4 T_\lambda^3/A_\lambda$, $t = T/T_\lambda$, $S_\lambda = 1559$ J/kg·K, and $A_\lambda = A_{GM}(T_\lambda) \simeq 1450$ m·s/kg. Note the maximum in (7.2) occurs at t = 0.885, which is 1.929 K at SVP. The values presented in Fig. 7.3 are good to about ±10% at saturated vapor pressure and have been compared to experiment up to about 0.7 MPa. Numerical values for $f^{-1}(T, p)$ are listed in Appendix A.3.

Recently, Sato et al. [7–10] performed extensive measurements of the average heat conductivity in turbulent He II over a wider range of temperatures and pressures up to 1.5 MPa. This work confirmed that the best fit to the heat conductivity function follows a power law $m = 3.4 \pm 0.1$. This extensive set of data was then used by Sato to develop an improved correlation for the turbulent heat conductivity function. The form of this correlation is similar to (7.1) where $m = 3.4$ and the heat conductivity function is written as a product of two terms,

$$f^{-1}(T,p) = h(t)g_{peak}(p) \tag{7.3}$$

where the reduced temperature $t = T/T_\lambda$ and $h(t,p)$ and $g_{peak}(p)$ are empirical functions. The normalized empirical function $h(t, p)$ is shown in Fig. 7.4 indicating a high quality correlation. This function has a peak at $t_{peak} = 0.882$.

Sato fit this quantity to a polynomial function,

$$h(t) = 1 + \left(t - t_{peak}\right)^2 \sum_{n=0}^{9} \{a_n(t-1)^n\} \tag{7.4}$$

where the polynomial coefficients are given in Table 7.1

The pressure dependent function was also fit to a polynomial as,

$$g_{peak}(p) = \exp\left(a + bp + cp^2\right) \tag{7.5}$$

where the coefficients (a, b and c) and the fit are shown in Fig. 7.5. This correlation is clearly an improvement over (7.2) and Fig. 7.3 and is recommended for more accurate numerical calculations. However, for approximate calculations particularly when they involve analytic solution, it is often more convenient to use the simplified form and keep the value of $m = 3$.

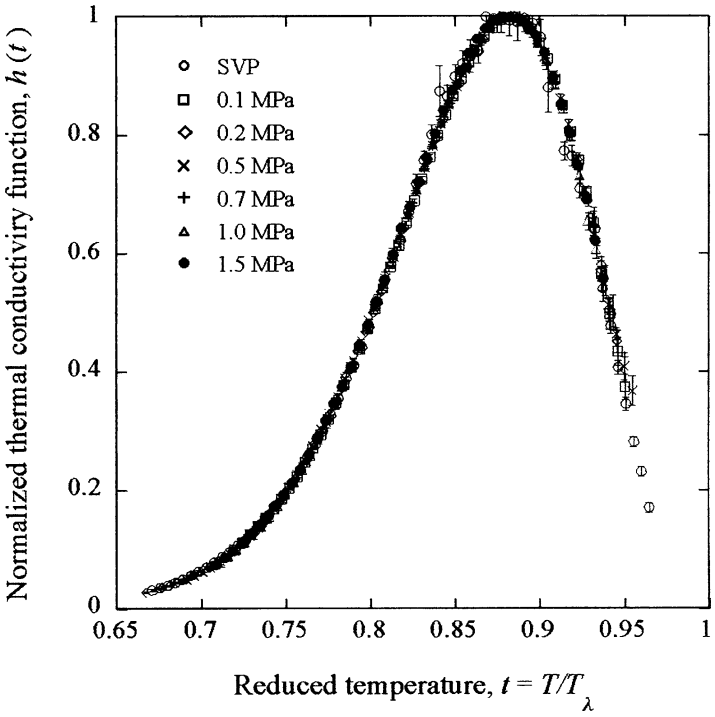

Fig. 7.4 Normalized thermal conductivity function at various pressures (Sato [6])

Table 7.1 Polynomial coefficients for (7.4) (Sato [6])

$a_0 = -71.818$	$a_1 = 1.2172617 \times 10^3$
$a_2 = -1.4992321 \times 10^4$	$a_3 = -3.9491398 \times 10^5$
$a_4 = -2.9716249 \times 10^6$	$a_5 = -1.2716045 \times 10^7$
$a_6 = -3.8519949 \times 10^7$	$a_7 = -8.6644230 \times 10^7$
$a_8 = -1.2501488 \times 10^8$	$a_9 = -8.1273591 \times 10^7$

7.1.2 Peak Heat Flux in Wide Channels

We now consider the limits to steady state heat transport in a finite-length channel. For a given steady heat flux, it is possible to determine the corresponding ΔT by integration of (7.1) (or the more refined Sato correlation, 7.3) for specified boundary conditions, e.g. T_b = constant. The maximum heat flux q^* is then established according to the maximum allowable temperature difference the channel, which for a given bath temperature T_b is $\Delta T_m \sim (T_\lambda - T_b)$. It follows that for a channel of length L

$$q^* = \left(\frac{1}{L} \int_{T_b}^{T_\lambda} \frac{dT}{f(T,p)} \right)^{1/m} \tag{7.6}$$

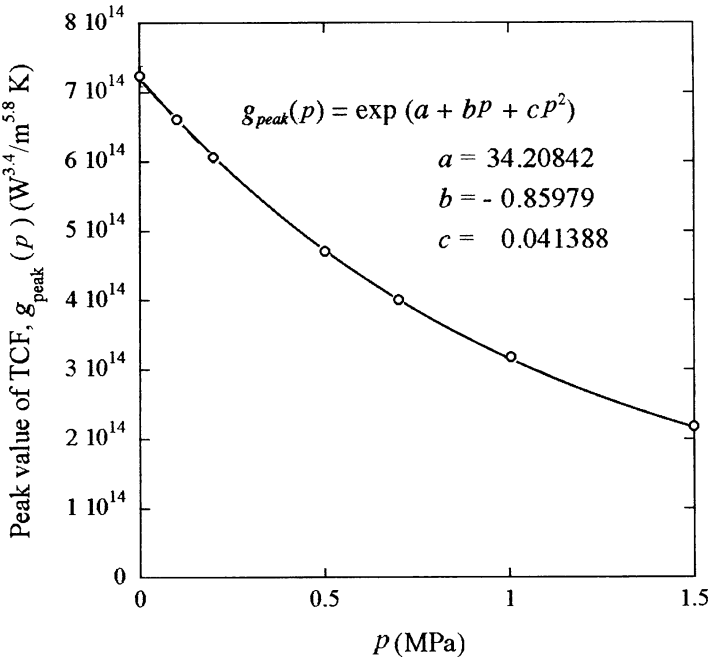

Fig. 7.5 Pressure dependence of the peak value of the thermal conductivity function (Sato [6])

This integral is mostly a function of T_b and only weakly dependent on other factors such as pressure. The integrated heat conductivity function is then defined as,

$$q^* L^{1/m} \equiv Z(T_b) = \left(\int_{T_b}^{T_\lambda} \frac{dT}{f(T,p)} \right)^{1/m} \tag{7.7}$$

which should be independent of channel length. Plotted in Fig. 7.6 are experimentally determined peak heat fluxes q^* for different channel lengths varying everywhere from 0.1 to 3 m. Two different correlations of the data are displayed: $Z'(T_b)$ for $m = 3$ and $Z(T_b)$ the other for $m = 3.4$. In either case, the agreement between data and correlation is acceptable.

By a similar analysis it is possible to determine the pressure dependence of the maximum heat flux q^*. Integration of the corresponding heat conductivity function $f^{-1}(T, p)$ predicts a decreasing maximum heat flux with elevated pressure. By analytic integration of (7.2), a prediction can be made for the behavior of q^* with pressure. The results of this analysis for four bath temperatures are displayed in Fig. 7.7. Also displayed are experimentally observed [4, 12] maximum heat fluxes for short channels up to 0.3 MPa. The agreement is again reasonable for the available data. As discussed above, an improved correlation can be obtained by using $m = 3.4$ and the Sato form for the heat conductivity function.

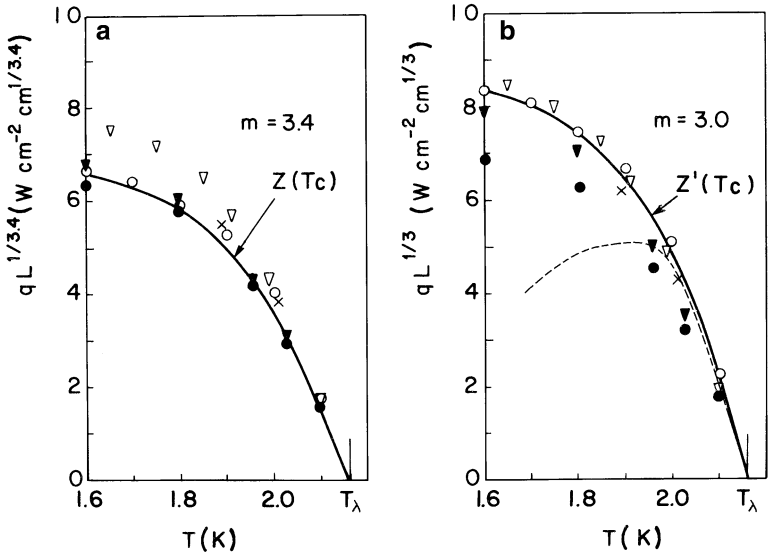

Fig. 7.6 Generalized steady-state limiting heat flux in He II (as compiled by Seyfert [11]). (**a**) is for the case where $m = 3.4$; (**b**) for the case with $m = 3$. The *dashed line* in (**b**) corresponds to near saturation boiling for a hydrostatic head of 0.1 m

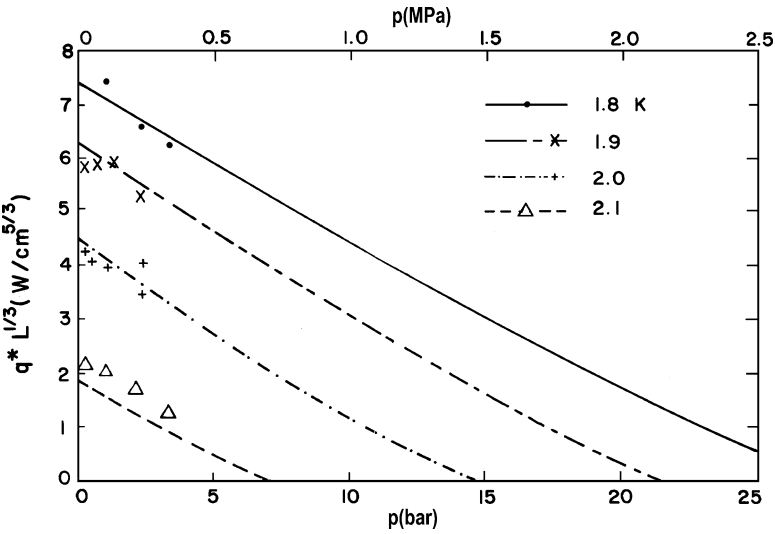

Fig. 7.7 Maximum heat flux in a He II-containing channel as a function of pressure (Data from Refs. [4] and [12])

It should be kept in mind that the form and physical explanation for heat transport in He II place no fundamental limit to the maximum steady state value for q^*. Everything depends on the allowable temperature difference. For example, with $T_b = 1.8$ K and $m = 3$, Fig. 7.4 predicts a product $q^*L^{1/3} = 7.4$ W/cm$^{5/3}$. Therefore, for a channel of length 10 μm, this analysis would predict a q^* in excess of 70 W/cm^2 (700 kW/m^2) truly a remarkable heat flux for liquid helium temperatures.

Example 7.1

Consider a 1 m long, 1 cm^2 cross section channel (see Fig. 7.2) containing He II at 2 K but pressurized to 0.5 MPa. Calculate the maximum heat flux in the He II channel.

To calculate the maximum heat flux, one needs to integrate the function. We use the simplified correlation with $m = 3$.

$$q^*L^{1/3} \equiv Z(T_b) = \left(\int_{T_b}^{T_\lambda} \frac{dT}{f(T,p)} \right)^{1/3}$$

Between 2 K and T_λ (p = 0.5 MPa). Since the channel is pressurized to 0.5 MPa, however, the appropriate form for $f^{1}(T,p)$ must be used, see Fig. 7.3. Fortunately, this integration has already been performed in Fig. 7.7. At 2 K and 0.5 MPa, $q^*L^{1/3} = 3$ W/cm$^{5/3}$. Thus, the a 1 m long, 1 cm^2 cross section channel, Q* = 0.65 W.

7.1.3 Peak Heat Flux in Saturated He II

In the discussion above, it has been assumed arbitrarily that the peak heat flux q^* is determined by the condition where the helium adjacent to the heater surface reaches the λ-point. This limit is not always met particularly in He II near its saturated vapor pressure for reasons having to do with the helium temperature distribution and the phase diagram, displayed in Fig. 7.8. We begin with the assumption that due to the high effective thermal conductivity of He II, the helium within the heat transfer region obeys equilibrium thermodynamics. This assumption allows the state of the helium everywhere in an experiment or engineering system to be described by a point on the equilibrium phase diagram.

Now consider a simple example, that of the heat transfer process occurring at the bottom of a vertical channel containing saturated liquid helium at 1.8 K, 1.6 kPa (12.5 torr). The heat transfer process is occurring at a certain depth, h, below the liquid-vapor interface; see Fig. 7.9. Thus, without any heat being applied, the state of the helium at the bottom of the channel can be described by location ① on the phase diagram in Fig. 7.8. The pressure applied at the heat transfer surface is therefore $p = p_0 + \rho gh$, where h is the hydrostatic head of the liquid helium. If heat

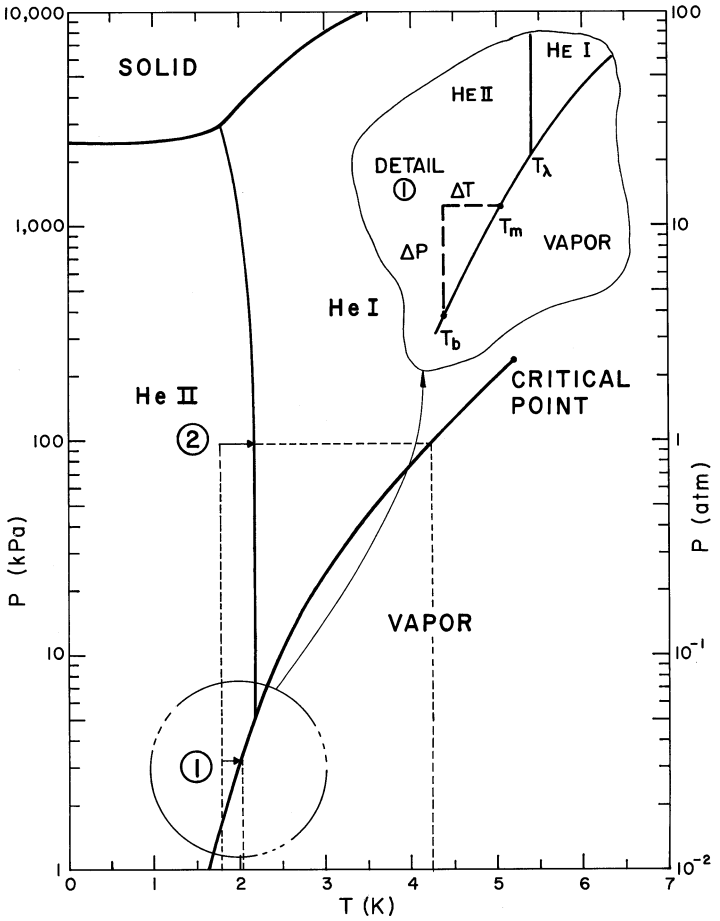

Fig. 7.8 Phase diagram of helium showing condition ① of near saturation and condition ② of subcooled helium to p = 100 kPa

is applied to induce heat transfer in the system, there will be a local temperature excursion ΔT that is determined by heat flow mechanisms as discussed above. The local temperature increases but the pressure is fixed, unless the experimental configuration is small enough for the thermomolecular effect to make a significant contribution. Neglecting this complication for the time being, as an increasing heat flux is applied, the temperature at the bottom of the channel will increase following a horizontal line as shown in the inset of Fig. 7.8 until at a certain heat flux it meets the liquid-vapor interface at which point boiling commences.

The value of the maximum temperature excursion is determined by the slope of the vapor pressure curve such that for finite ΔT,

$$\Delta T_m = \int_{p_0}^{p_0+pgh} \left(\frac{dT}{dp}\right) dp \tag{7.8}$$

Fig. 7.9 Vertical channel containing in near saturated He II

The slope of the pressure curve, $(dT/dp)_{sat}$ can be obtained from helium property tables or database codes. However, it is also known from thermodynamics through the Clausius-Clapeyron equation,

$$\left.\frac{dp}{dT}\right|_{sat} = \frac{h_{fg}}{T\Delta v} \approx \frac{h_{fg}}{Tv_g} \tag{7.9}$$

which can be further simplified by assuming the helium vapor to be an ideal gas, that is $v_g = RT/p$. This results in an approximate form for the allowable temperature increase,

$$\Delta T_m \simeq \frac{RT^2}{h_{fg}} \ln\left(1 + \frac{\rho g h}{p_0}\right) \tag{7.10}$$

This expression is suitable for $\Delta T_m \ll T_b$. For larger values of ΔT it is better to evaluate the saturation temperature at the pressure corresponding to the given hydrostatic head.

Under saturation conditions, this means that the maximum ΔT_m the He II can sustain may be less than that in pressurized liquid where $T_m = T_\lambda$. How does this impact the maximum heat flux? Returning to (7.6) and replacing T_λ with T_m, we note that the peak heat flux, q^* will be suppressed relative to the results shown in Fig. 7.6 with the amount of suppression dependent on h, the hydrostatic head. Considering the example above and let $h = 0.1$ m, we can recalculate the quantity $q^*L^{1/3}$ for is case. The result as a function of bath temperature is shown by the dashed line in Fig. 7.6b. Note that the magnitude of the suppression is small near T_λ, but becomes significant at lower temperatures since in that case, the maximum temperature, T_m is well below T_λ.

It is worth noting that the pressure corresponding to the λ-point is $p_\lambda = 4.97$ kPa (37 torr), which is equivalent to a column of helium about 3.55 m high. This fact is important because if a saturated vapor pressure He II system with vertical dimension larger than several meters is constructed, it would experience a heat transfer limitation determined by T_λ rather than the saturation line.

Example 7.2

Consider a 0.1 m long vertical channel (see Fig. 7.9) containing He II boiling at 1.638 kPa corresponding to a saturated vapor pressure at 1.8 K. Thus, the liquid free surface is at 1.8 K. If a heat flux is applied to the bottom of the channel, the temperature at that point will increase until it reaches local saturation at which point local boiling will occur. Calculate the maximum temperature of the He II at the bottom of the channel.

Since the liquid level is not very large, we can use the approximate expression for ΔT_m (7.10),

$$\Delta T_m \cong \frac{RT^2}{h_{fg}} \ln\left(1 + \frac{\rho g h}{p_0}\right)$$

Substituting values, $h = 0.1$ m, $h_{fg} = 23$ kJ/kg, the resulting $\Delta T_m = 0.025$ K and $T_m = 1.825$ K. As indicated, this is an approximate result. The more accurate result would be obtained by calculating the saturation temperature, T_s, corresponding to the pressure $p = p_0 + \rho gh = 1{,}638$ Pa + 145 kg/m^3 × 9.8 m/s^2 × 0.1 m = 1,780 Pa. Then referring to a data base code, one obtains T_s (p = 1780 Pa) = 1.824 K. These values are very close, since the head is not large. The result would not be as good if the level were significantly larger.

Alternatively, it is possible to create a subcooled liquid condition whereby the pressure at the heat transfer surface is higher than that due to the hydrostatic head. This condition can occur, for example, in a closed volume He II region cooled by a saturated bath heat exchanger. In this case, the pressure on the closed volume can take on any value between saturation and the solid line at 2.5 MPa. The subcooled He II state is shown on the phase diagram, Fig. 7.8, by position ②. Here it is assumed that the applied pressure is 100 kPa. A similar argument to that presented above applies when determining the temperature excursion; however, in the subcooled case the maximum temperature is governed by the λ-transition (at $p = 100$ kPa, $T_\lambda = 2.168$ K). In this case, the limit on maximum temperature relatively well fixed and only weakly dependent on applied pressure.

The conditions that exist once the maximum heat flux is exceeded are of great importance to understanding the heat transfer in this regime, a topic which is discussed more extensively in Sect. 7.6. Generally, there are two cases that can

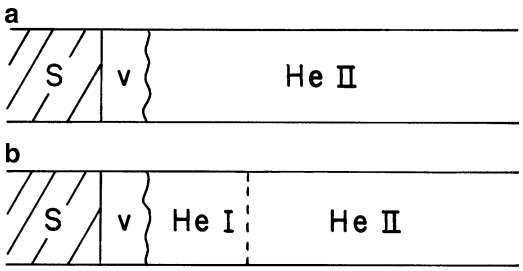

Fig. 7.10 Schematic of boiling in He II: (**a**) saturation condition and (**b**) subcooled condition

occur, each of which is associated with one of the two conditions indicated on the phase diagram in Fig. 7.8. For the saturation case, which applies to position ①, q^* corresponds to the helium adjacent to the interface achieving saturation conditions. A schematic representation of the resulting physical condition for $q > q^*$ is shown in Fig. 7.10a. Displayed is a solid heat transfer surface blanketed by a vapor film which in turn is bounded by the He II at local saturation temperatures. This phase boundary is defined clearly because the He II-vapor transition is first order.

The alternative film boiling heat transfer situation occurs whenever q^* is exceeded under subcooled conditions, such as ② in Fig. 7.8. For this case the phase transition is between He II and normal liquid He I. Since, with rare exception, the maximum heat flux in He I is substantially less than that in He II, exceeding q^* under subcooled conditions invariably results in a double transition, first creating a film of liquid He I followed by boiling of the He I to form a vapor film. This triple-phase phenomenon brings all three helium states in close proximity to the heat transfer interface. A schematic representation of this process is shown in Fig. 7.10b. Through the He II–He I interface, shown as a dotted line in the figure, the density ρ and temperature T should be continuous. Visualization experiments of boiling in saturated and subcooled He II have observed the interfaces between the vapor-He I and the He I-He II phases [13]. This result is shown in Fig. 7.11. Being able to observe the He I – He II phase boundary is particularly significant since the physical properties of helium should be continuous through the phase transition.

7.1.4 He II Heat Transfer in Cylindrical Geometries

Besides the simple linear geometry represented by a one-dimensional tube with constantheat flux, there has been considerable work carried out on cylindrical geometries consisting of a heated cylinder or wire immersed in a large bath of He II [14–16]. It is easy to show, by assuming that the Gorter-Mellink equations

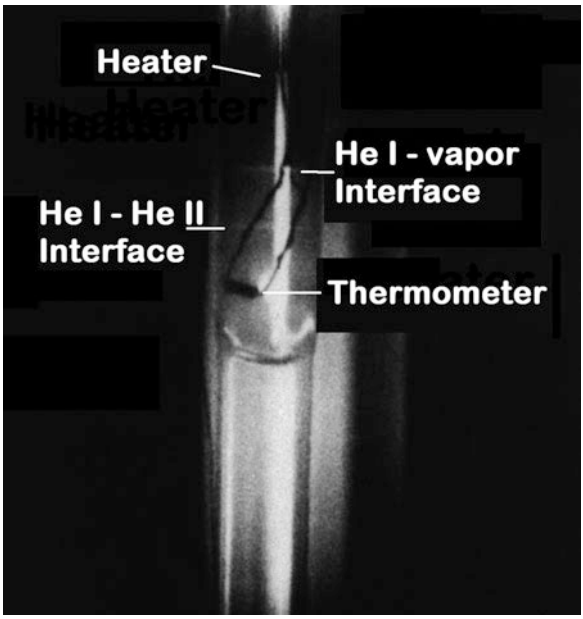

Fig. 7.11 Subcooled He II boiling showing the He I-vapor and He II – He I phase boundaries [13]

apply in cylindrical geometry, that the steady-state heat transport equation can be written as

$$\frac{dT}{dr} = -f(T)q_0^m\left(\frac{r_0}{r}\right)^m \tag{7.11}$$

where q_0 is the heat flux per unit area of the heated cylinder of radius r_0. The difference in (7.11) occurs because the heat flux decreases as the radius increases. Comparison of (7.11) with experiment has given reasonable agreement, with essentially the same heat conductivity function as applies in linear geometries [17, 18]. In a similar fashion to that applied to (7.3), integration of (7.11) leads to the maximum heat flux,

$$q_0^* = \left(\frac{m-1}{r_0}\int_{T_b}^{T_\lambda}\frac{dt}{f(T)}\right)^{1/m} \tag{7.12}$$

The important observation to make about (7.12) is that the peak heat flux q_0^* has as its scaling length r_0 rather than L as in the linear system. This means that, provided the radius of the container is much larger than that of the heater, the boundary conditions far from the heater should not affect q^* significantly. This is certainly contrary to the behavior in linear geometries.

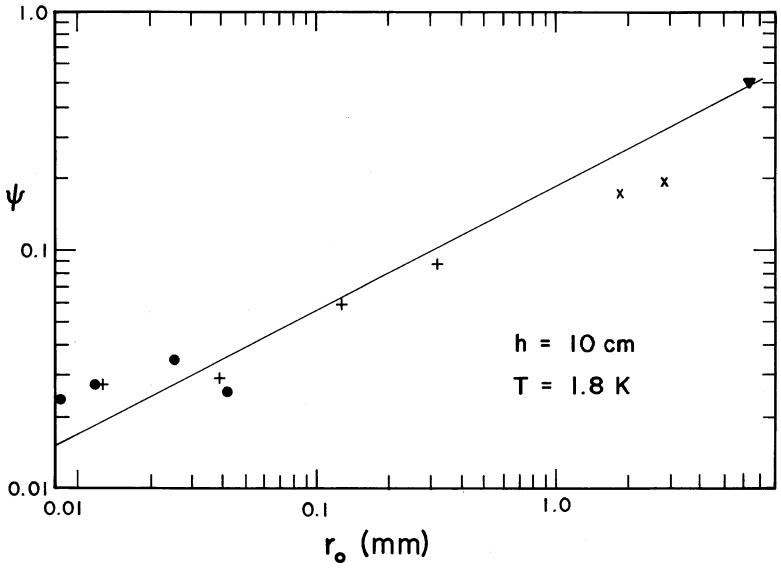

Fig. 7.12 Empirical correlating function for heat transfer in cylindrical geometries [17, 18]

Unlike the linear one-dimensional system, there have been fewer attempts to correlate the peak heat transport in cylindrical geometries with that of (7.12). This is due in part to the lack of reliable data, which are more difficult to obtain in cylindrical geometries. In one experiment, data were fit for small temperature differences $\Delta T \approx 10$ mK in the range of $T_b = 1.8$ K [17, 18]. It was found that the expression given by (7.11) is not entirely suitable to correlate the experimental values of q_0^* without introducing a radius-dependent quantity Ψ defined by

$$q_0^* = \left(\frac{2\Psi}{r_0} \int_{T_b}^{T'} \frac{dT}{f(T)} \right)^{1/3} \tag{7.13}$$

where $T' \simeq T_b + 0.01$ K. Ψ was found empirically to depend on radius, being roughly proportional to $r_0^{1/2}$. The results of this correlation are shown in Fig. 7.12. Note that Ψ is always less than 1, indicating that the peak heat flux is always less than that predicted by the idealized theory. This fact is somewhat surprising because the temperature gradients appear to be given accurately by (7.11).

7.1.5 Static Bath He II Heat Exchangers

He II heat exchangers are indispensable components for superconducting magnets and other systems cooled with pressurized He II. However, because of the unusual properties of He II, specifically the high effective heat conductivity and strong

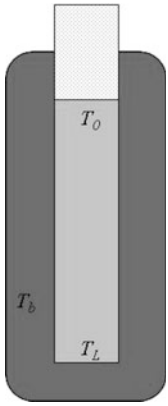

Fig. 7.13 Schematic of a simple static He II heat exchanger

temperature dependent heat capacity, conventional heat exchanger design methods, such as effectiveness or NTU, are not suitable. In this section, we discuss the design of He II heat exchangers based on the available transport equations.

There have been a number of He II heat exchangers designed and developed for applications. The most common of these is the static bath type system, shown schematically in Fig. 7.13. The principal component of this system is a saturated He II reservoir of active length L and cross section A in thermal contact through its surface to a surrounding pressurized He II reservoir. Any heat generated in the pressurized He II reservoir must be transferred through the solid wall to the saturated bath where it is removed by evaporation of the liquid. For this type of system, there are three design criteria:

1. The surface area of the heat exchanger must be large enough to transfer the heat with minimal ΔT between the two reservoirs. Normally, the surface heat transfer process is controlled by the Kapitza conductance of the heat exchanger material and possibly thermal conduction through the solid wall. These quantities combine into an overall heat transfer coefficient, U. It is important to make the heat exchanger of copper or other high conductivity material to avoid a significant conduction thermal resistance.
2. Boiling in the bulk liquid within the heat exchanger should be avoided. This means that the liquid should be subcooled by the hydrostatic head enough to avoid surface boiling which could degrade performance.
3. There must be sufficient He II cross section in the saturated bath to transport the heat by counterflow with a small temperature gradient.

The beginning point for the analysis of a static He II heat exchanger is the steady state He II heat equation with surface heat transfer,

$$\frac{d}{dx}\left(f(T)^{-1}\frac{\partial T}{\partial x}\right)^{\frac{1}{3}} - \frac{PU}{A}(T - T_b) = 0 \tag{7.14}$$

where $f(T)^{-1}$ is the He II heat conductivity function appropriate for fully developed turbulent conditions and T is the temperature of He II within the heat exchanger. U is the overall heat transfer coefficient between the two reservoirs. Equation (7.14) can be simplified by making the following change of variables:

$$\Theta = \frac{T_b - T}{T_b - T_0} \tag{7.15a}$$

and

$$m_{HeII} = \left[\frac{PU(T_b - T_0)^{2/3}}{f^{-\frac{1}{3}}A}\right]^{\frac{3}{4}} \tag{7.15b}$$

With the constant properties assumption the following dimensionless equation results,

$$\frac{d}{dx}\left(\frac{d\Theta}{dx}\right)^{1/3} - m_{HeII}^{\frac{4}{3}}\Theta = 0 \tag{7.15c}$$

Equation (7.15a) is analogous to the classical fin equation in conduction heat transfer except for the non-linear thermal conduction feature of the He II. However, the solution to (7.15a) is similar and can be preformed semi-analytically depending on boundary conditions [19]. Just as in the case of the fin equation, the boundary condition at the end of the heat exchanger determines the exact form of the solution.

If we define the origin at the surface of the He II, the boundary condition at $x = 0$ is $\Theta = 1$ by definition. The fluid temperature increases away from the free surface. The boundary condition at the bottom of the heat exchanger ($x = 1$) can have difference cases:

1. Convection heat transfer: $\left(f^{-1}\frac{d\Theta}{dx}\right)^{\frac{1}{3}} = U\Theta_L(T_b - T_0)^{\frac{2}{3}}$
2. Adiabatic: $\left(\frac{d\Theta}{dx}\right)_L^{\frac{1}{3}} = 0$
3. Prescribed temperature: $\Theta(x = L) = \Theta_L$
4. Infinite length: $\Theta(x = L) \xrightarrow{L=\infty} 0$

and $m_{HeII}L$ is dimensionless fin length. Each case has a slightly different form for the solution. Typically, in a good design $m_{HeII}L \sim 1$; however, it can take on any value. If $m_{HeII}L >> 1$, then the heat transfer process is only weakly affected by the boundary condition at $x = L$ and the infinite length solution is a good approximation for all cases.

To calculate the total heat transfer through the heat exchanger, one integrates (7.15c) one time to obtain the temperature gradient, $d\Theta/dx$. This quantity is then evaluated at x = 0 such that,

$$Q = -A\left(f^{-1}\frac{dT}{dx}\right)_{x=0}^{\frac{1}{3}} \tag{7.16}$$

Table 7.2 Coefficients of (7.17) for different boundary conditions: $\beta = AU^3(T_b - T_0)^2/2Pf^{-1}$ (From Ref. [19])

Boundary condition	γ	Θ_L^2
Convection heat transfer	$\Theta_L^2 - \beta\Theta_L^2$	$\frac{1}{2\beta} - \left[\frac{1}{4\beta^2} - \frac{1-(Q/M_{Hell})^4}{\beta}\right]^{1/2}$
Adiabatic	Θ_L^2	$1 - (Q/M_{Hell})^4$
Prescribed temperature	†	†
Infinite length	0	0

†Value is determined by implicit solution

The result of this calculation is an expression for the total heat transfer,

$$Q = M_{HeII}(1-\gamma)^{\frac{1}{4}} \tag{7.17}$$

Where $M_{HeII} = 1.19A[m_{HeII} f^{-1}(T_b - T_0)]^{1/3}$ which is analogous to the total heat transfer expression obtained from the fin equation. The dimensionless quantity γ is a function of the particular boundary conditions imposed at $x = L$. The corresponding form for γ is listed in Table 7.2. Note that if $\gamma << 1$, the total heat transfer is only a weak function of the boundary conditions at $x = L$ and the infinite length heat exchanger is a good approximation with $Q = M_{HeII}$.

The temperature profile along the heat exchanger can be further calculated by integrating (7.15c) a second time. This solution depends on the choice of boundary condition at $x = L$. The resulting general solution for the temperature profile is obtained by solving the integral,

$$\int_{\Theta_L}^{1} \frac{d\Theta}{\left(\Theta^2 - \gamma\right)^{\frac{3}{4}}} = 1.68 m_{HeII} x \tag{7.18}$$

For all boundary conditions except the infinite heat exchanger, the solution of (7.18) requires numerical methods. For the special case of the infinite channel, $\gamma = 0$ and $Q_L = 0$, which leads to the closed form solution,

$$\Theta(x) = \left[\frac{1}{0.84 m_{HeII} x + 1}\right]^2 \tag{7.19}$$

One can compare the numerical solution for fixed boundary conditions at $x = L$ to that of the infinite channel. The results for adiabatic solution are shown in Fig. 7.14.

The performance of a He II heat exchanger can also be treated in a fashion similar to that of ordinary fins. Using the conventional expression for the effectiveness of a fin, we obtain

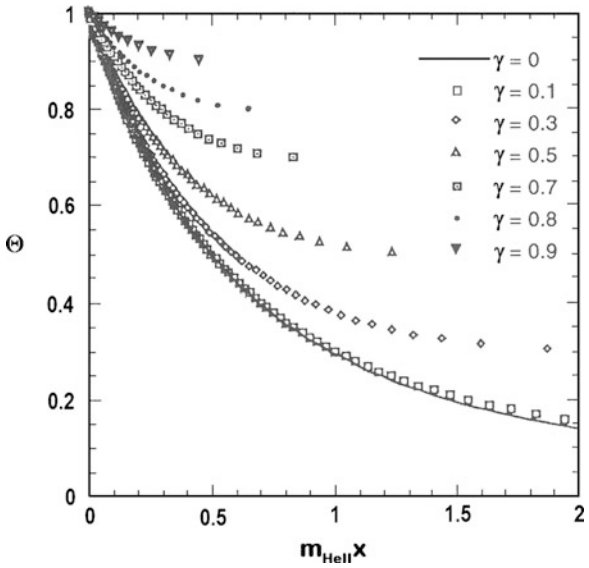

Fig. 7.14 Dimensionless temperature profile along a He II heat exchanger. The data points are obtained by numerical solution of (7.15) for adiabatic boundary conditions with different values of γ. Also shown by the solid line is the analytic solution for $\gamma = 0$ (7.19)

$$\varepsilon_f = \frac{Q_{actual}}{UA(T_b - T_0)} = \left[\frac{2Pf^{-1}(1-\gamma)}{U^3A(T_b - T_0)^2}\right]^{\frac{1}{4}} \tag{7.20}$$

Note that for typical values, $f^{-1} = 10{,}000\ \mathrm{kW^3/m^5\ K}$, $U = 2\ \mathrm{kW/m^2\ K}$ and $(T_b - T_0) = 50$ mK we obtain $\varepsilon_f \sim 30\ (P/A)^{1/4}$ in SI units. Therefore, for all reasonable geometries, $\varepsilon_f >> 1$. For short heat exchangers with $\Theta_L \sim 1$, ε_f is simply equal to the ratio of the actual surface area to the base area. For long heat exchangers, where $\Theta_L << 1$, the effectiveness is still generally much greater than unity because of the high effective thermal conductivity of the He II.

In a similar fashion, the fin efficiency can be defined as,

$$\eta_f = \frac{Q}{UA_{fin}(T_b - T_0)} = \varepsilon_f \left(\frac{A}{A_{fin}}\right) \tag{7.21}$$

This quantity is almost always of order unity unless $\Theta_L << 1$. Typically, $\eta_f \sim 1$ unless $m_{HeII}L > 1$.

Before leaving the subject of He II heat exchangers, it is important to comment on one of the other limitations to the performance of static saturated bath heat exchangers. This is related to item 2 above in the list of design considerations. For a heat exchanger to perform well, the heat transfer process should be only governed by Kapitza conductance at the heat exchange surface. However, if boiling occurs

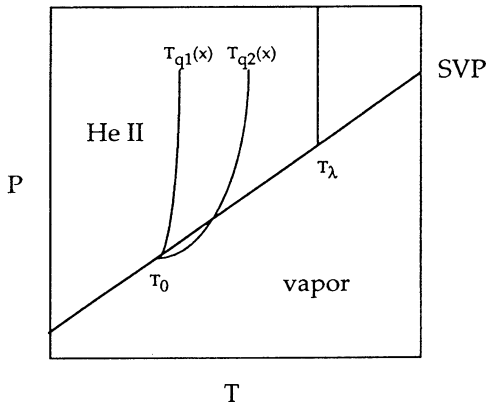

Fig. 7.15 Localized region of the He II phase diagram illustrating the boiling condition that can occur in a static, saturated bath heat exchanger

within the heat exchanger, it is possible that the performance will be degraded. To avoid bulk boiling in the bath, we therefore need to ensure that nowhere the heat exchanger does the He II reach saturation conditions. Such conditions can occur at various points within the heat exchanger due to the non-linear temperature profile and varying heat flux within the He II column.

Figure 7.15 illustrates this situation. The free surface of the heat exchanger is assumed to be fixed at T_0, while below that point the liquid is subcooled by the hydrostatic head (ρgh). With no heat load, the temperature in the heat exchanger is uniform at T_0. However, with a heat load, the temperature below the surface increases due to the Gorter-Mellink heat transfer. The temperature profile is steepest at the surface of the liquid due to the accumulation of heat flux ($q(x)$) along the channel. Two representative temperature profiles are shown in the figure. Boiling will occur if the predicted temperature profile crosses the saturation line, see $T_{q2}(x)$. In this case, the slope of the temperature profile at the surface is steeper than the slope of the saturated vapor curve allowing the bulk liquid to boil locally. If the heat flux is increases, the boiling region will expand within the heat exchanger.

The critical condition for boiling can be made more quantitative by equating the slope of the temperature profile at the free surface ($x = 0$) to the slope of the saturated vapor pressure line,

$$\left.\frac{dT}{dx}\right|_{x=0} = \rho_l g \left.\frac{dT}{dp}\right|_{svp} \tag{7.22}$$

As before, the slope of the saturated vapor pressure line is given by the Clausius-Clapeyron equation as,

$$\left.\frac{dp}{dT}\right|_{svp} = \frac{h_{fg}}{T\Delta v} \approx \frac{h_{fg}p}{RT^2} \tag{7.23}$$

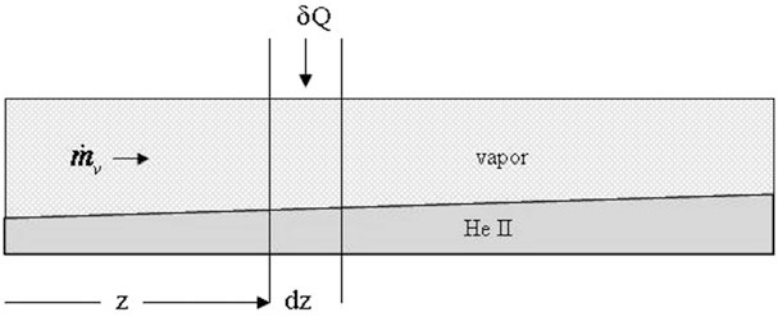

Fig. 7.16 Schematic of He II-vapor two phase flow system

where the last approximate form results from assuming the saturated helium vapor obeys the ideal gas law. Substituting the form for the counterflow heat transport in the He II (7.1) and assuming for simplicity that $m = 3$, the following expression occurs,

$$q_{\max} = \left(\frac{\rho_l g R T^2 f^{-1}}{h_{fg} p_0} \right)^{\frac{1}{3}} \tag{7.24}$$

This expression has a peak near 1.87 K at $q_{max} = 14$ kW/m^2. It decreases from the peak dominated by the temperature dependence of the heat conductivity function, $f^{-1}(T, p)$.

7.1.6 He II Two Phase Heat Transfer and Flow

In recent years, applications have emerged that use of He II in a horizontal tube in co-existence with its saturated vapor. The first of these involves the use of a near horizontal He II – vapor heat exchanger to cool subcooled He II for the LHC accelerator magnets [20]. The other recent application involves the use of horizontal two phase He II – vapor lines in large RF cavity accelerators [21]. Proper design of these systems depends on a thorough picture of the relevant helium hydrodynamics.

We begin by considering a long, horizontal tube that is partially filled with near static He II, see Fig. 7.16. In such a system, there are three basic heat transfer mechanisms: (1) Gorter-Mellink counterflow in the bulk liquid; (2) forced convection mass transport in the vapor phase; and (3) mass exchange by evaporation or condensation between the two phases. The addition of the mass transfer between the two phases makes the heat transfer process in two-phase He II far more complex problem than that of single-phase He II.

We first discuss the semi-analytic solution to this problem for which several simplifying assumptions required. First, the liquid within the tube is assumed to be in a stratified flow condition with a near horizontal interface between the liquid and vapor. This is a reasonable assumption based on experiments. Next, thermal gradients normal to the axis of the tube are assumed to be negligible so that the problem becomes that of two coupled one-dimensional systems. Finally, the liquid is assumed to be in local thermodynamic equilibrium with its vapor so that $T_L(z) = T_v(z)$, where z is the axial dimension coordinate. The goal is to construct a model to predict the behavior of the temperature profile, $T(z)$, liquid level or void fraction ($\alpha = A_v/A$), and liquid, vapor mass flow rates, $\dot{m}_l, \dot{m}_v$ and total heat transfer, Q.

For most cases of interest the liquid is nearly static so that the pressure drop along the tube is determined primarily by friction in the vapor phase, which is given by the expression,

$$\frac{dp}{dz} = -\frac{2f_F}{\rho_v D_H}\left(\frac{\dot{m}_v}{\alpha A}\right)^2 \tag{7.25}$$

where f_F is the Fanning friction factor, α is the void fraction and A is the total cross section of the tube. In (7.25), $\dot{m}_v$ and α will in general be functions of z so that dp/dz is not a constant. In a stratified flow system, α is directly related to the liquid level.

At any point along the channel, the total heat flux is a combination of two terms: the flux of vapor due to evaporation and the counterflow heat flux through the He II. These two terms sum directly,

$$Q(z) = \dot{m}_v h_{fg} - (1-\alpha)A\left(f^{-1}\frac{dT}{dz}\right)^{\frac{1}{3}} \tag{7.26}$$

where the first term on the right is the heat carried by convection of the vapor and the second is the liquid counterflow heat transport. h_{fg} is the heat of vaporization. In (7.26) there are three unknowns: $\dot{m}_v$, α and dT/dz.

Since the He II and vapor are in thermodynamic equilibrium, it follows that the pressure gradient may be written in terms of the derivative along the saturation line of He II and the local temperature gradient,

$$\frac{dp}{dz} = \left.\frac{dp}{dT}\right|_{svp}\frac{dT}{dz} \approx \frac{\rho_v h_{fg}}{T}\frac{dT}{dz} \tag{7.27}$$

where use has been made of the Clausius-Clapeyron equation, $dp/dT)_{svp} = \Delta s/\Delta v \approx \rho_v h_{fg}/T$ for an ideal gas which approximates low density helium vapor. Combining (7.25) and (7.27), we obtain a relation for the temperature gradient in terms of the vapor mass flux,

$$\frac{dT}{dz} = \frac{-2f_D T}{\rho_v^2 h_{fg} D_H}\left(\frac{\dot{m}_v}{\alpha A}\right)^2 \tag{7.28}$$

which is again a relationship between three unknowns dT/dz, $\dot{m}_v$ and α.

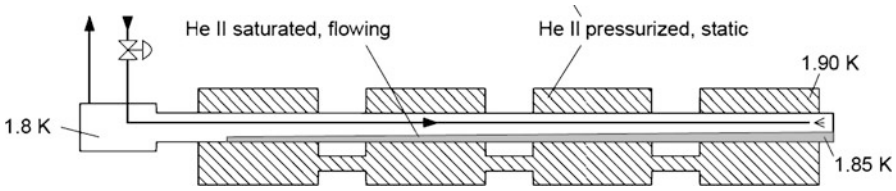

Fig. 7.17 Configuration of the He II bayonet heat exchanger [24]

The third relationship between the unknowns in the problem is obtained by considering the He II to be essentially static, $v_l \approx 0$ and using the hydrostatic head condition on the pressure. In this case with the saturation condition, we can state that the pressure at the bottom of the channel is a sum of the saturation pressure plus the hydrostatic head, $p_0 = p_s(T) + \rho g y$ where y is the liquid level. Taking p_0 to be a constant and differentiating, it follows that the pressure gradient is directly proportional to the void fraction gradient or slope in the liquid/vapor interface,

$$\frac{dp}{dz} = -\rho_l g \frac{dy}{dz} \tag{7.29}$$

Again making use of the chain rule and Clausius-Clapeyron equation for an ideal gas, we obtain a relationship between the temperature and void fraction gradient,

$$\frac{dy}{dz} = -\frac{\rho_v h_{fg}}{\rho_l g T} \frac{dT}{dz} \tag{7.30}$$

Equation (7.30) suggests that a large temperature gradient will result in a large slope of the liquid/vapor interface as indicated in Fig. 7.16.

The above expressions has an analytic solution for a rectangular cross section channel with a constant heat flux [22], which simplifies the problem of relating the liquid level (y) to the void fraction, α. The results of the analysis were successfully compared to experiment. An important outcome of the analysis was to show that for typical geometries of horizontal He II heat exchangers, the heat transported by the coexisting vapor is roughly ten times as efficient as that carried by counterflow. Thus, the benefits of horizontal two phase He II cooling systems are evident. Numerical studies of near horizontal two phase He II-vapor systems has been performed in the context of RF cavity accelerator development [23]. The goal of this work was to be able to model the temperatures, flow rates and liquid levels in existing cryogenic facilities. Such a modeling effort has been sufficiently successful to add credence to the belief that similar two phase He II systems can be designed and successfully operated.

An important application of a near horizontal He II – vapor system is the so called bayonet heat exchanger developed for the LHC, shown schematically in Fig. 7.17 [24]. This unique design uses a corrugated tube partially filled with He II to extract the heat loads from the accelerator magnets. The two phase liquid from

the refrigerator is expanded into the far end of the heat exchanger with the vapor returning above the stratified liquid. The heat exchanger works by a similar principle as discussed above, but in this case the heat flux is determined by the heat exchange through the wall of the tube into the saturated two phase flow.

The heat transfer rate is determined by the overall heat transfer coefficient of the heat exchanger, which is equal to the series thermal resistance of the two surface heat transfer coefficients and the thermal resistance of the corrugated tube. Since the saturated bath side of the heat exchanger is only partially filled with liquid, the wetted surface area is not well defined. However, experiments have shown that a combination of He II film flow and liquid droplet entrainment in the vapor provides a very effective heat exchange process even for high void fraction [25].

A simplified analysis [24] of the bayonet heat exchanger is based on similar assumptions as were discussed above in two phase He II flow modeling. In the case of the heat exchanger, the following assumptions are made. First, the void fraction is sufficiently high that the pressure drop is determined entirely by the vapor flow rate,

$$\frac{dp}{dz} = -\frac{2f_D}{\rho_v D_H}\left(\frac{\dot{m}_v}{A}\right)^2 \tag{7.31}$$

Second, that the total heat transfer, $Q = qL$, determines the overall change in the vapor mass flow rate,

$$Q = qL = h_{fg}(\dot{m}_{out} - \dot{m}_{in}) \tag{7.32}$$

where $q = UP(T_o - T_i)$, the heat removed per unit length of the heat exchanger. Third, the vapor quality, $\chi = \dot{m}_v/\dot{m}_{out}$ at the outlet is assumed to be unity, pure vapor flow and $\chi_0 = \dot{m}_{in}/\dot{m}_{out}$. For these conditions, (7.31) can be integrated over the length of the heat exchanger assuming a circular cross section tube of diameter D, to yield the total pressure drop,

$$\Delta p = \frac{32f_D}{3\pi^2}\frac{q^2}{\rho_v h_{fg}^2}\frac{L^3}{D^5}\left(\frac{1-\chi_0^3}{(1-\chi_0)^3}\right) \tag{7.33}$$

This equation establishes the minimum diameter that meets the pressure drop requirements. In addition, a criterion is suggested on the maximum vapor velocity of 5 m/s to ensure that the flow is stratified. This leads to,

$$A \geq \frac{qL}{h_{fg}\rho_v v_{\max}}\frac{1}{1-\chi_0} \tag{7.34}$$

Depending on boundary conditions, the two criteria based on (7.33) and (7.34) yield similar constraints on the heat exchanger design. For example, a 100 m long bayonet heat exchanger with a 1 W/m heat load would need to have diameter of

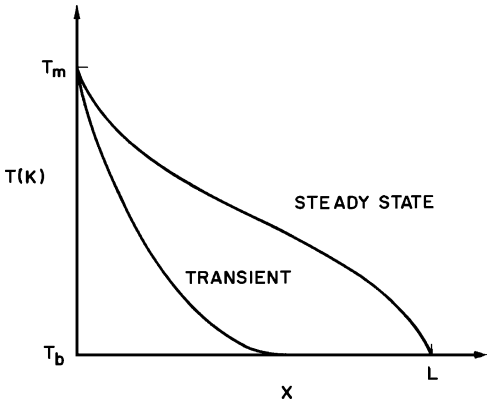

Fig. 7.18 Schematic temperature distributions in He II under steady-state and transient conditions

about 50 mm for a ΔT of 50 mK. This is to be compared to 180 mm diameter tube that would be required to carry the same heat load over the same temperature difference in pure thermal counterflow in bulk He II.

7.2 Transient Heat Transport in Wide Channels

A thorough understanding of the time evolution of the temperature distribution in He II is of the utmost importance to fully describe the heat transfer process. Up until this point, the assumption has been made that the heat transfer is steady-state and can be interpreted by using equilibrium thermodynamic models and the helium phase diagram. This assumption is certainly an oversimplification because there are a number of time-dependent phenomena that affect the heat transport properties of He II. To determine the relative significance of transient phenomena in a heat transfer problem, the following questions must be asked: At what point in time does a system exposed to some change in the heat flux reach steady state? What are the physical processes that control this time development? To answer these questions it is necessary to take account of the energy scales associated with heat transport in He II.

We begin by considering a one-dimensional channel of length L cooled by a constant temperature bath at one end, see Fig. 7.2. Initially, the temperature of this system is uniform at T_b. However, if a heat flux is applied at the end away from the bath, a temperature distribution will evolve until eventually a steady-state condition is achieved with the temperature at the heated end being $T_m > T_b$. Typical transient and steady-state temperature distributions are shown schematically in Fig. 7.18.

There are a number of energy inputs required to achieve the steady-state temperature distribution in He II. The first of these we may associate with the acceleration of the two fluid components, normal and superfluid, to v_n and v_s, respectively. Since the fluids are initially at rest, it is necessary to apply sufficient kinetic energy for steady-state counterflow to be established. For typical heat

fluxes, the normal fluid and superfluid velocities are of the order of a few tens of mm/s. This value leads to a kinetic energy density of considerably less than 1 J/m^3, which we will see is very small on the scale of interest.

Since the He II is initially in the non-turbulent state, a second energy flux which must be applied to the system is that necessary to create the turbulence. This process has been described physically in Chap. 6 with an expression for the time required to create turbulence in a channel being,

$$\tau = aq^{-3/2} \tag{6.109}$$

The coefficient a is a temperature-dependent function of the order of 10^5 W$^{3/2}$·s/m^3. Equation (6.109) has no length dependence, presumably because the growth of turbulence travels at the velocity of second sound and therefore would be essentially uniform in a short channel at moderate heat flux. Rearranging (6.109) we can determine the energy required to produce turbulence as,

$$q\tau = aq^{-1/2} \tag{7.35}$$

which for heat fluxes in the range of a few tens of kW/m^2 gives an estimated value of about 1 kJ/m^2. For a channel having a length of the order of 1 m, the energy density associated with the creation of turbulence works out to be $q\tau \approx 1$ kJ/m^3.

Also of concern is the energy carried by the second sound pulse itself. This mechanism is probably most important at the highest values of heat flux. Second sound shock was discussed in Chap. 6 and it was shown that depending on conditions, an energy as large as 100 J/m^2 can propagate along a channel in advance of the turbulent front. For very short times, this can be the dominant mechanism for heat transfer and as was mentioned above is probably the mechanism for turbulence propagation. Still this is not a large amount of energy compared to the heat content of the He II itself.

The final principal energy input required to create the steady-state temperature distribution in Fig. 7.18 is that of the enthalpy content of the He II itself. The heat capacity of liquid helium is very large, particularly near the λ-transition where on a volumetric basis it is of the order of 1 MJ/m^3 K. Therefore to establish the steady-state temperature distribution sufficient heat must be applied to increase the fluid temperature from that of the bath to its local steady-state value $T(x)$. In practical systems this increase is of the order of 0.1 K. The required energy density needed to achieve a given temperature distribution can be written

$$\varepsilon_C = \frac{\rho}{A_0 L}\int_0^L dx \int_{T_b}^{T(x)} C_p(T)dT \tag{7.36}$$

which is of the order of 100 kJ/m^3. Furthermore, as the length of the channel increases the dominance of this term increases, particularly for long channels with $L \gtrsim 1$ m. Because the enthalpy profile dominates the transient heat input, other

energies associated with this problem rarely are considered. Therefore, it is assumed that at least for engineering systems experiencing moderate heat fluxes ($q \sim 10$ kW/m^2), the transient temperature distribution is controlled by heat transport and enthalpy considerations. As a result, a diffusion like model has been shown to describe the problem effectively.

7.2.1 He II Diffusion Equation

For background, we consider the time dependent heat transport in a conductive solid. This process is described by a well-known diffusion equation, which in one dimension is,

$$\frac{\partial T}{\partial t} = D_{th} \frac{\partial^2 T}{\partial x^2} \tag{7.37}$$

where $D_{th} = k/\rho C$ is the thermal diffusivity having units of m^2/s. The form of (7.37) has the inherent assumption of constant properties, k, ρ, and C. Otherwise, the equation is somewhat more complex. Equation (7.37) has been solved for a wide variety of boundary conditions with non-dimensional results applicable to many of the problems. However, without going through a specific solution for a particular set of conditions, some physical discussion of its implications can be made. In particular, it is possible to construct a characteristic time, called the diffusion time τ_D, which is obtained by non-dimensionalizing (7.37) and has the form

$$\tau_D = \frac{L^2}{D_{th}} \tag{7.38}$$

where the length L is the total length of the conduction path. For the case of the one-dimensional rod heated at one end, L is the overall length. The diffusion time is a measure of the thermal relaxation of the system. In most diffusion problems, the solution is scaled in terms of the dimensionless Fourier number,

$$Fo = \frac{t}{\tau_D} \tag{7.39}$$

Since the conduction is dominated by exponential terms, τ_D is not the actual relaxation time but is proportional to the time required to reach the steady state. For $Fo >> 1$, the problem is essentially in steady state, while for $Fo \lesssim 1$, the full diffusion equation must be considered.

To achieve a high rate of heat diffusion it is necessary to have a high thermal diffusivity. Solids possessing the largest values of D_{th} are high-conductivity metals at low temperatures, where not only if k large, but the specific heat C is small.

For example, high-purity copper near 4 K has $\rho C \approx 1$ kJ/m^3 and a thermal conductivity $k \approx 1$ kW/m K which gives $D_{th} \approx 1$ m^2/s. For high-purity metals at low temperatures the diffusion time constant, assuming a characteristic length $L \approx 1$ m, is of the order of seconds.

Although He II clearly does not obey the simple diffusion equation (7.37), it is useful nonetheless for physical understanding to make some order-of-magnitude comparisons. Since turbulent He II in one dimension obeys the nonlinear heat flow equation given by (7.1), it is possible to define an effective thermal conductivity, albeit dependent on heat flux,

$$k_{\text{eff}} = \frac{1}{f(T,p)q^2} \tag{7.40}$$

As can be seen in Fig. 7.3, the quantity, $f^{-1}(T, p)$ typically has a value around 10,000 kW^3/m^5 K near 1.8 K and saturated pressure. Therefore, for a heat flux $q = 10$ kW/m^2, the effective thermal conductivity is of order 100 kW/m K, which is about two orders of magnitude larger than for high-purity metals at low temperatures. Of course, the heat flux dependence of k_{eff} works against the transport of large heat fluxes. At 100 kW/m^2, k_{eff}, is reduced by two orders of magnitude to around 1 kW/m K, which is comparable to that of copper in the same temperature range.

The effective thermal diffusivity of He II, D_{eff}, can also be defined according to the analogy with solid conduction. Around 1.9 K, $\rho C \approx 0.5$ MJ/m^3 K, which gives a value for $D_{\text{eff}} \approx 0.2$ m^2/s. For a characteristic length of 1 m, this effective thermal diffusivity leads to a characteristic time constant $\tau_D \approx 5$ s. Furthermore, since the diffusion time goes as the square of the characteristic dimension, larger systems have time constants that can be very long compared to other time constants in the problem.

To properly treat transient heat transfer problems in He II; however, it is necessary to use a general heat diffusion equation. The derivation of the equation is analogous to that of the ordinary diffusion equation although the thermal conduction relationship must be replaced with the nonlinear Gorter-Mellink expression (7.1). The result may be written in the form of a one-dimensional heat diffusion-like equation,

$$\rho C_p \frac{\partial T}{\partial t} = \frac{\partial}{\partial x}\left(\frac{1}{f(T)}\frac{\partial T}{\partial x}\right)^{1/3} \tag{7.41}$$

where again we assume for simplicity that $m = 3$ in the counterflow heat conduction term. This expression has a very similar appearance to the ordinary diffusion equation, with the one exception that it involves an unusual power of the temperature gradient. Because of the nonlinear character of (7.41), it is apparent that extraordinary efforts are needed to solve this equation. There are in fact several methods available to treat this equation, here we will only consider approximate analytic solutions. Numerical solution of the He II energy equation will be discussed in a subsequent section.

We begin by casting (7.41) into a dimensionless form by introducing the variables,

$$\Theta^* = \frac{T - T_b}{T_\lambda - T_b} \tag{7.42a}$$

and

$$x^* = \frac{x}{L} \tag{7.42b}$$

$$\tau \equiv \frac{t}{f^{1/3}\rho C(T_\lambda - T_b)^{2/3}L^{4/3}} \tag{7.42c}$$

Which then reduces (7.41) to dimensionless form as,

$$\frac{\partial \Theta^*}{\partial \tau} = \frac{\partial}{\partial x^*}\left[\left(\frac{\partial \Theta^*}{\partial x^*}\right)^{1/3}\right] \tag{7.43}$$

By analogy to (7.37) one can interpret the quantity $D_{HeII} = 1/f^{1/3}\rho C(T_\lambda - T_b)^{2/3}$ like a thermal diffusivity for He II with the characteristic diffusion time being proportional to $L^{4/3}$. This is a notable difference from classical heat diffusion. In that case, doubling the characteristic length increases the thermal relaxation time by a factor of four, while in He II the increase is by a factor of $2^{4/3} = 2.52$.

7.2.2 *Analytic Solution Methods*

One solution method for the nonlinear heat transport equation (7.43) employs a technique known as similarity solutions [26–28]. This approach makes use of changes of variables which reduce the nonlinear partial differential equation (7.43) to a nonlinear ordinary differential equation that is inherently easier to solve. Then making the approximation that the heat conductivity function and specific heat are constant over the range of interest (7.43) can be integrated to obtain the solution. Note that the constant properties assumption is only a good approximation for $\Theta^* << 1$.

The similarity solution method uses what are termed stretching transformations which leave the partial differential equation unchanged. The solution of (7.43) is then determined by choice of boundary conditions. We considered here two problems of interest. The first problem concerns the application of a constant heat flux q at $x = 0$, which is referred to as the clamped flux problem. It leads to boundary conditions of the form

$$\left.\frac{\partial \Theta^*}{\partial x^*}\right|_{x=0} = -\frac{q^3 f L}{T_\lambda - T_b} \quad \text{for all } t \tag{7.44a}$$

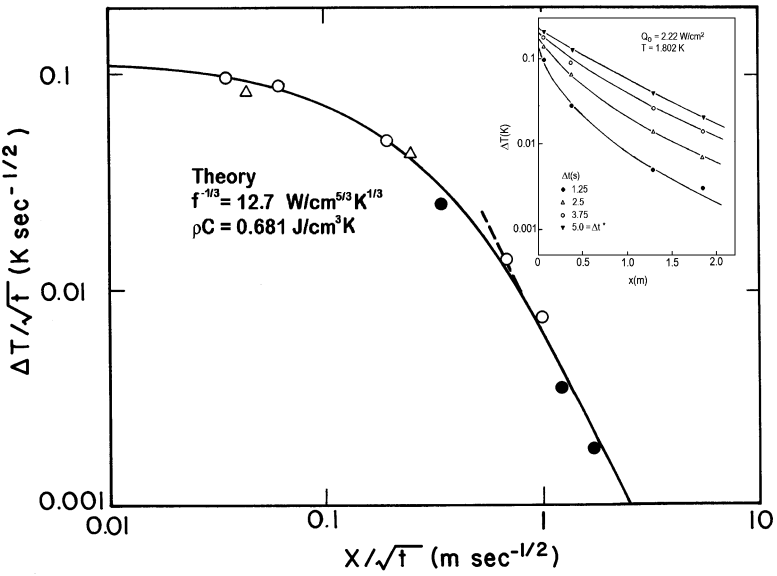

Fig. 7.19 Calculated normalized temperature profile for clamped flux in He II at $T_b = 1.8$ K and $q = 22$ kW/m^2 model by Dresner [26] compared to experimental data (inset) [29]

and

$$\Theta^*(x, 0) = 0 \tag{7.44b}$$

$$\Theta^*(\infty, \tau) = 0 \tag{7.44c}$$

The first of these conditions originates from the requirement that the heat flux q obey the nonlinear heat conductivity equation at $x = 0$.

It can be shown that the general solution for the temperature distribution should take a functional form [26],

$$\Theta/\tau^{1/2} = y(x/\tau^{1/2}) \tag{7.45}$$

Therefore, a plot of experimental data in this form should provide a universal curve representing the function y. Displayed in Fig. 7.19 are interpolated results from the long one-dimensional channel described earlier. The data do in fact follow a universal curve. In addition, the magnitude of the general solution can be determined to have a simple form when evaluated at $x = 0$, that is

$$\left.\frac{\Delta T}{t^{1/2}}\right|_{x=0} = a^2 q^2 \left(\frac{f}{\rho C}\right)^{1/2} \tag{7.46}$$

where a is a proportionality constant of order unity. At large values of x, the result approaches an asymptotic dependence such that

$$\left.\frac{\Delta T}{t^{1/2}}\right| = \left(\frac{4\sqrt{3}}{9}\right)\left(\frac{1}{\rho C}\right)^{3/2}\left(\frac{1}{f}\right)^{1/2}\frac{t}{x^2} \tag{7.47}$$

This expression is exemplified by the linear region on a log-log plot for large $x/\tau^{1/2}$.

The above analysis is also able to predict the critical energy flux ΔE^* beyond which the heat transfer enters film boiling. For the clamped flux problem, this quantity has been measured experimentally by detecting the time to film boiling, Δt^*, for a given heat flux. A relationship that fits the experimental data has the simple form

$$\Delta t^* = \kappa q^{-4} \tag{7.48}$$

where κ is a temperature-dependent function [29]. The same relationship also follows from the above theoretical analysis, and κ is predicted to take the form

$$\kappa = \frac{\rho c(T_\lambda - T_b)^2}{f a^4} \tag{7.49}$$

where a is the same numerical coefficient as given in (7.46). By inserting average values for the heat conductivity function and the volumetric specific heat into (7.49), the predicted coefficient κ agrees with experiment to within about 20%.

The other problem of interest in one-dimensional transient heat transfer is the determination of the temperature profile resulting from a given energy deposition. This pulsed-source problem, which can also be solved by the similarity solution method, must obey the boundary conditions

$$\int_{-\infty}^{\infty} \rho C(T - T_b)dx = \Delta E \quad \text{for all time} \tag{7.50a}$$

$$\Theta(x, 0) = 0 \tag{7.50b}$$

$$\Theta(\infty, \tau) = 0 \tag{7.50c}$$

where $\Delta E = q\Delta t$ is the total thermal energy applied per unit channel area. Again using the similarity solution method, it can be shown that the pulsed-source problem has a general solution of the form [27],

$$\Theta\tau^{3/2} = y'(x/\tau^{3/2}) \tag{7.51}$$

where y' is another undetermined function. As in the clamped flux problem, (7.51) is a powerful result because it indicates the form in which to plot data. Plotted in terms of these variables, the experimental data should follow a universal curve.

By substitution of (7.51) into (7.43), a solution to the temperature distribution can be obtained with the simplifying assumption of constant properties. The resulting equation takes the form

$$\Delta T\ t^{3/2} = \frac{4}{3\sqrt{3}} \Delta E \left(\frac{f}{\rho C}\right)^{1/2} \left(\frac{1}{Z^4 + b^4}\right)^{1/2} \tag{7.52a}$$

where

$$Z = x\Delta E(\rho C f)^{1/2} t^{-3/2} \tag{7.52b}$$

and

$$b = \frac{2\left[\Gamma\left(\frac{1}{4}\right)\right]^2}{3\sqrt{3}\pi} = 2.855 \tag{7.52c}$$

That this solution fits the original heat conductivity equation can be verified by the reader.

Experimental verification of the above analysis is displayed in Fig. 7.20. The inset shows the time variation of the temperature distribution after a discrete energy pulse is applied. These data, plotted in the form suggested by the similarity solution, map out the universal curve given by (7.52a). The universal curve plotted in the figure has as its necessary input average values for the heat conductivity function and heat capacity, but when ΔT is small, these properties do not vary substantially over the range of interest. The agreement between experiment and theory is entirely adequate for engineering applications.

7.2.3 *Numerical Solution of the He II Diffusion Equation*

The above analytical treatment is useful for providing a physical description of the problem as well as developing scaling relationships to correlate data. However, a complete solution including the temperature dependence of the physical parameters is only possible by numerical methods. The usual approach is to apply finite difference methods. Here the exact differentials in T, x, and t are replaced by finite differences with an appropriate choice of mesh size. These in turn lead to a set of simultaneous equations for the temperature at the nodes in the mesh. Solutions of this type have been carried out for two different boundary conditions [30]. In both cases the clamped heat flux condition at $x = 0$ is assumed. However, different

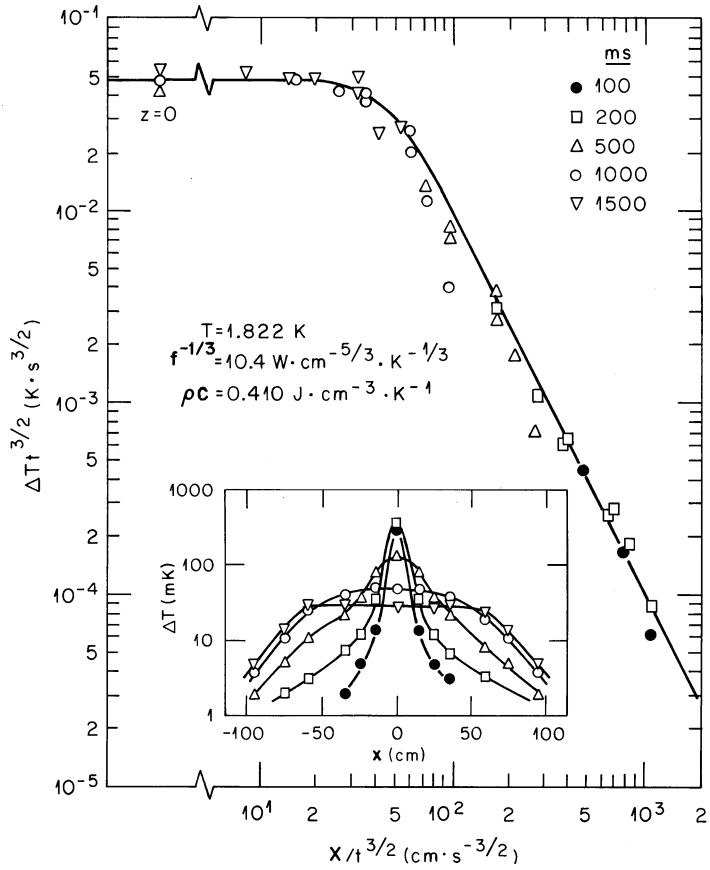

Fig. 7.20 Normalized temperature distribution for the helium channel subjected to a pulsed heat source (From Dresner [27])

boundary conditions are applied at $x = L$ where the channel contacts the reservoir. These conditions have two forms,

$$\left.\frac{d\Theta}{dx}\right|_{x=L} = 0 \quad \text{adiabatic end} \tag{7.53a}$$

and

$$\Theta|_{x=L} = 0 \quad \text{isothermal end} \tag{7.53b}$$

Particularly for the first case, it is useful to scale the data in terms of a ratio of energies ($\Delta E^*/\Delta E_0$), where these quantities are defined individually as

$$\Delta E^* = q\ \Delta t^* \tag{7.54}$$

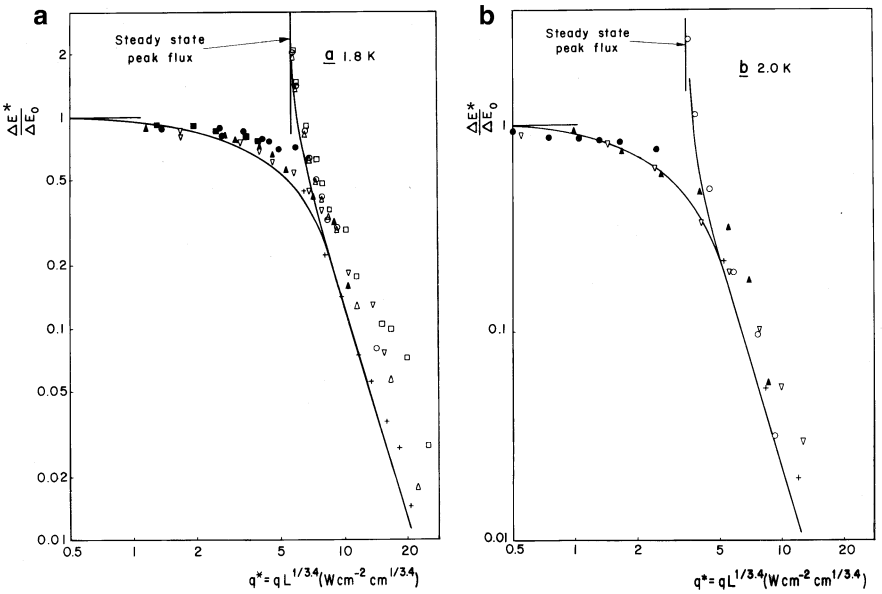

Fig. 7.21 Maximum energy flux for a step-function heat pulse. Steady-state peak heat flux represents the open-channel solution. $\Delta E^*/\Delta E_0 \leq 1$ is the closed-channel solution: (**a**) 1.8 K and (**b**) 2.0 K (as compiled by Seyfert et al. [30])

and

$$\Delta E_0 = L\int_{T_b}^{T_\lambda} \rho C_p \, dT \tag{7.55}$$

Therefore, (7.55) represents the energy applied through the heat transfer surface which is necessary to reach film boiling at Δt^*. The other energy, ΔE_0, represents the total enthalpy available within the constant cross section channel of length L. Obviously, for the adiabatic end condition, the ratio $\Delta E^*/\Delta E_0 \leq 1$. For short, high-energy heat pulses such that the heat diffusion length is much shorter than the total channel length L, the solution is independent of choice of boundary condition established at $x = L$.

Plotted in Fig. 7.21 are the numerical solutions to the one-dimensional heat transfer problem for two different bath temperatures, 1.8 and 2.0 K. In either case the ratio of energy is plotted versus the scaling parameter $qL^{1/m}$, where in this case $m = 3.4$ by selection of the authors [30]. The data give comparable agreement for $m = 3$. Note that for values of $qL^{1/.34}$ in excess of 10 at 1.8 K and 5 at 2.0 K, there is no significant difference between the two boundary conditions at $x = L$. The steady-state limit corresponds to the results presented in Sect. 7.1.2.

In conclusion, a general comment is in order concerning transient heat transfer in He II. As noted above the time constant to establish the steady state can be quite

large, particularly in long one-dimensional system. Although this fact may be surprising considering the extremely high effective thermal conductivity of He II, it is due to the large heat capacity of He II resulting in a finite thermal diffusivity. Therefore, care should be exercised when applying steady-state heat transfer models. It is best first to estimate the thermal diffusion time to determine whether the system is actually in the steady state. For transient problems, the heat diffusion model is generally suitable. Unfortunately, it is not known whether there are limits of this model, and extrapolation beyond the regions where experimental data exist should be avoided.

7.3 Forced Convection Heat Transport in Wide Channels

We now extend the topic of turbulent He II heat transport to include the effect of forced convection or net flow velocity. This subject is a somewhat more general heat transport problem than has been considered so far because it includes an additional variable, the net flow velocity, v. Forced convection was introduced in Chap. 6 as part of the two-fluid model applied to He II heat transport.

A general configuration for a forced flow heat transfer problem is shown in Fig. 7.22. A channel of constant cross section and length L connects two reservoirs at temperatures T_1 and T_2. A steady state or transient heat q flux is applied in this case at one end of the channel and the temperature gradient within the fluid is established. Breakdown of heat transfer occurs at a peak heat flux, q^*, which depends on a number of factors including the fluid velocity. In fact, this configuration is not easily obtainable because a temperature difference normally corresponds to a pressure difference under saturation conditions. However at least in principle, it is possible to create the appropriate conditions with a frictionless piston that forces the liquid from volume 1 to volume 2 at velocity v. Alternatively, one could establish these conditions by forcing He II to flow through a channel of length $2L$ with both ends in thermal contact with a reservoir at temperature T_2.

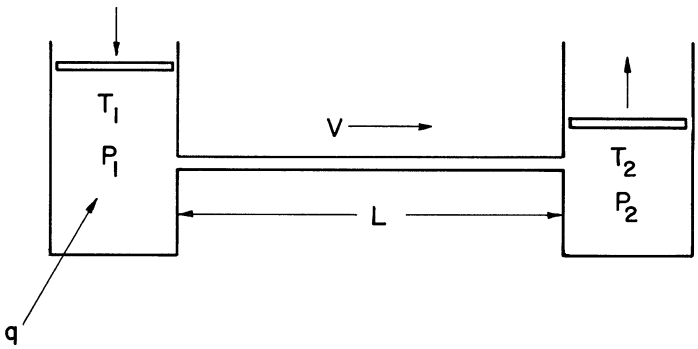

Fig. 7.22 Schematic representation of configuration required to obtain forced flow He II

7.3.1 He II Energy Equation

We begin by developing the heat balance equation that describes the forced flow He II system [31]. In developing this equation, two fundamental assumptions are made about the physical behavior of He II**.** These assumptions are not proved here but are justified by the analysis of experimental data.

The first assumption is that the heat flow by internal convection mechanisms is not affected by the net velocity of the fluid. This point has been discussed as part of the two-fluid model in Chap. 6. As an aside, it is possible to understand physically the invariance to velocity by analogy to an ordinary heat conduction mechanism. In the latter case, heat transported by conduction in a moving medium is no different from that of the medium at rest provided $v \ll c$, the speed of sound. Furthermore, by making the normal set of simplifications to reduce the problem to one-dimensional heat flow in turbulent He II**,** the nonlinear heat conductivity equation can be used to describe the heat conducted by internal convection,

$$q_{ic} = -\left(f(T,p)^{-1}\frac{dT}{dx}\right)^{1/3} \tag{7.56}$$

where $f^{-1}(T,p)$ is the same temperature-dependent heat conductivity function. The power law dependence of (7.56) has been assumed to be 1/3 although the analysis follows essentially the same procedure if a different coefficient is assumed.

The second assumption is that the heat carried by ordinary convection mechanisms can be described by the flow of enthalpy between two points in the system,

$$q_{fc} = \rho \mathbf{v}\ \Delta h \tag{7.57}$$

where $dh = h_1 - h_2$ represents the specific enthalpy difference between temperatures T_1 and T_2. For simplicity (7.57) assumes the fluid density to be constant, which is a reasonably good approximation for He II.

The above two assumptions lead to an equation that is appropriate for analyzing the temperature profile in forced flow He II. This is achieved by combining differential forms of (7.56) and (7.57) and equating them to the time rate of change of the local enthalpy. The resultant equation is similar to the time-dependent heat equation for static He II except that it contains the extra convection term. In one dimension this expression takes the form,

$$\rho\frac{\partial h}{\partial t} - \frac{\partial}{\partial x}\left[\left(\frac{1}{f}\frac{\partial T}{\partial x}\right)^{1/3}\right] + \rho\mathbf{v}\frac{\partial h}{\partial x} = q_0 \tag{7.58}$$

where the temperature and pressure dependence of the heat conductivity function is implied. This equation is sometimes referred to as the He II energy equation.

Given the boundary conditions for a channel containing He II, it is a straightforward problem to integrate (7.58) and thus determine the temperature profile as a function of flow velocity and time. Unfortunately, a general solution to (7.58) requires numerical methods because the equation is nonlinear and the functions such as h and f have rather strong temperature dependencies.

7.3.2 Steady State Heat Transport: Analytic Solution

A good approximate solution to the steady-state problem, $\partial h/\partial t = 0$, can be obtained by assuming constant properties, f and C_p, and neglecting pressure drop effects such that $dh = C_p\, dT$. This approximation leads to an exactly soluble one dimensional differential equation. Making the following change of variables,

$$\Theta^* = \frac{T - T_2}{T_1 - T_2} \tag{7.59a}$$

$$x^* = \frac{x}{L} \tag{7.59b}$$

and defining the dimensionless variable,

$$K_v = \rho C_p \mathbf{v} (fL)^{1/3} (T_1 - T_2)^{2/3} \tag{7.59c}$$

an exactly soluble form of the Bernoulli equation results,

$$-\frac{d}{dx^*}\left[\left(\frac{d\Theta^*}{dx^*}\right)^{1/3}\right] + K_v \frac{d\Theta^*}{dx^*} = 0 \tag{7.60}$$

where $q_0 = 0$ has been assumed. Equation (7.60) coupled with the appropriate boundary conditions can determine the steady-state temperature profile in a one-dimensional channel.

Before proceeding to the solution, the physical interpretation of the dimensionless number K_v deserves some comment. As it represents the ratio of the heat carried by forced convection, $\rho C_p v \Delta T$, to that carried by counterflow, $(f^1 \Delta T/L)^{1/3}$, K_v is analogous to the classical Peclet number, $Pe = \rho C_p v L/k$, that is the ratio of forced convection to thermal conduction in classical liquids. Therefore, $K_v \sim 1$ marks the boundary between thermal counterflow dominated heat transfer and forced convection dominated heat transfer in He II.

The results of integrating (7.60) for a channel of length $2L$ with its center at T_1 and ends fixed at T_2 are displayed in Fig. 7.23. The left-hand side of the figure can be interpreted as the case where the velocity of flow is in the opposite direction to the heat flow by counterflow while the right-hand side refers to these quantities working in parallel. Note that the limitations of to the accuracy of this solution are

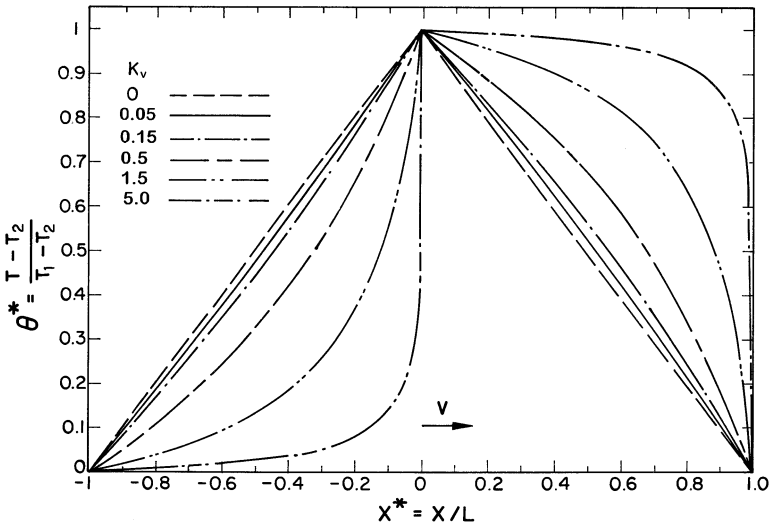

Fig. 7.23 Normalized temperature distribution in forced flow He II with fixed temperature boundary conditions $K_v = \rho C_p \mathbf{v}(fL)^{1/3}(T_1 - T_2)^{2/3}$

primarily in terms of the temperature dependence of the heat capacity C_p and heat conductivity function $f^{-1}(T,p)$. The solution should be quite good for small $\Delta T = T_1 - T_2$ such that $\Delta T/T \ll 1$. The impact of this approximation is seen in the zero velocity profile ($K_v = 0$) which is linear, while in fact for large ΔT the profile has considerable curvature. Also note that the nonzero velocity profiles for positive and negative K_v are symmetric about the line corresponding to $K_v = 0$.

There have been several reports of measured temperature profiles within forced flow He II which have been compared to numerical analyses based on the theory described above [32–34]. In general, these measurements have shown temperature profiles analogous to those displayed in Fig. 7.23. In those cases, (7.60) was solved numerically and compared to experimental data with good agreement.

Given the solution to the temperature profile it is straightforward to determine the total heat transport, $q = q_{fc} + q_{ic}$, by integration of (7.60). This result can be normalized to the form

$$\frac{q}{q_0} = -\left(\frac{d\Theta^*}{dx^*}\right)^{1/3} + K_v\Theta^* \tag{7.61}$$

where K_v is defined above and

$$q_0 \equiv \left(\frac{T_1 - T_2}{fL}\right)^{1/3} \tag{7.62}$$

which represents the heat carried by the internal convection mechanisms for He II having zero velocity ($K_v = 0$). The results of this calculation are shown by the solid

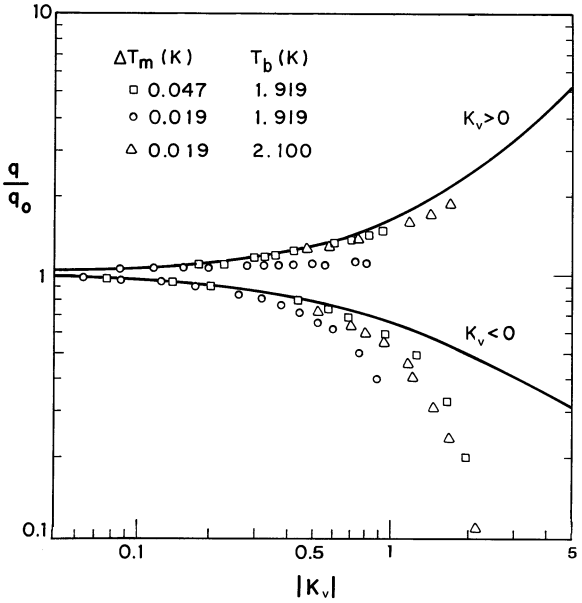

Fig. 7.24 Normalized peak heat flux for forced flow He II with $K_v = \rho C_p \mathbf{v}(fL)^{1/3} (T_1 - T_2)^{2/3}$ (Data from Jones and Johnson [34])

curves in Fig. 7.24. The data points are from an experiment by Johnson and Jones [34]. Although there is considerable enhancement of heat transport in the direction of flow even for small K_v, values of K_v greater than unity are required before the total heat transport is enhanced significantly in a midpoint heated channel of length $2L$. This result occurs because forced flow suppresses the total heat transport when the velocity and heat flux are anti-parallel.

7.3.3 Pressure Drop in Turbulent He II

The above solution to the steady state He II energy equation neglected any effect due to the pressure drop along the channel thus allowing the simplification, $dh = C_p\, dT$. However, in forced flow He II, there can be a significant pressure drop associated with flow. The pressure drop in fully turbulent He II has been measured for a variety of channel geometries with the most notable feature of these measurements being the similarity of friction factor to that for classical fluids. In other words, the pressure drop may be correlated with the expression,

$$\Delta p = 2 f_F \rho v^2 \left(\frac{L}{D}\right) \tag{7.63}$$

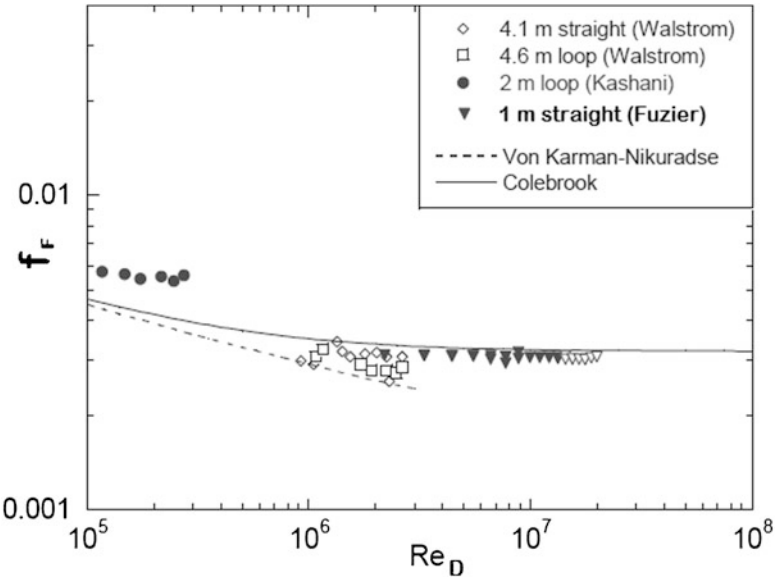

Fig. 7.25 Friction factor for He II forced flow compared to classical correlations (Fuzier [35])

where the Fanning friction factor, f_F, is similar to that observed for classical fluids. For example, for a smooth tube, the friction factors for He II in the Reynolds number regime $\mathrm{Re}_D > 2 \times 10^4$ appear to be fairly well described by the von Karman-Nikuradse correlation,

$$\frac{1}{f_F^{\frac{1}{2}}} = -1.737 \ln\left(\frac{1.25}{\mathrm{Re}_D f_F^{\frac{1}{2}}}\right) \tag{7.64}$$

where the Reynolds number is defined by $\mathrm{Re}_D = \rho v D/\mu_n$. At high Reynolds number, the tube surface roughness begins to play a role in the observed friction factor tending to an almost constant value. In this regime, the Colebrook correlation is preferred,

$$\frac{1}{f_F^{\frac{1}{2}}} = -1.737 \ln\left(\frac{k}{3.7D} + \frac{1.25}{\mathrm{Re}_D f_F^{\frac{1}{2}}}\right) \tag{7.65}$$

Note that both these correlations were discussed in Chap. 4 in the context of pressure drop in classical helium flow. For non circular cross section channels, present evidence suggests that the friction factor may also be correlated by classical correlations based on the Reynolds number.

Figure 7.25 shows measurements of the turbulent friction factor for He II compared to the classical correlations above [35]. Similar results have been obtained for other geometries [36–39]. One can easily see that the agreement is reasonable.

This result can be understood in terms of the two fluid model. In relatively high Reynolds number flows, both fluid components can be assumed to be fully turbulent with the superfluid component containing a very high vortex line density that interacts with the normal fluid component. In this case, the two fluids are strongly coupled together in motion. On the other hand in the viscous boundary layer, the normal fluid velocity profile is what controls the wall friction. Thus, the friction factor should scale with the classical Reynolds number with the relevant density and velocity being that of the total fluid while the viscosity scale is that of the normal fluid component, μ_n.

The above development for the most part assumes that the helium flow is fully developed and turbulent. This allows both the use of the turbulent pressure drop correlations and the turbulent heat transport relation. More complex phenomena can occur particularly in flow systems consisting of narrow channels in laminar flow, which can lead to fountain effect driven flows. We return to this topic in a later section.

7.3.4 He II Joule Thomson Effect

Walstrom considered the problem of steady state forced flow He II with pressure drop [40]. In this case, the enthalpy gradient must include the pressure terms,

$$\frac{\partial h}{\partial x} = \left(\frac{\partial h}{\partial T}\right)_p \left[\frac{\partial T}{\partial x} - \left(\frac{\partial T}{\partial p}\right)_h \left(\frac{\partial p}{\partial x}\right)\right] = C_p \left(\frac{\partial T}{\partial x} - \mu_j \frac{\partial p}{\partial x}\right) \tag{7.66}$$

where $\mu_j = \frac{\beta T - 1}{\rho C_p}$ is the Joule Thomson coefficient with β being the bulk expansivity. For He II, β is relatively small and negative ($\beta \sim -0.01$ K^{-1}) so that μ_j is negative and dominated by the incompressible term. In addition, since the pressure gradient may be large in this case, it is no longer possible to neglect that contribution to the He II two fluid equations (6.98) and (6.99). If one further makes the assumption that the pressure gradient can be replaced by $\Delta p/L$ and replace μ_j by $-1/\rho C_p$, then the full energy equation results,

$$\rho C_p \frac{\partial T}{\partial t} - \frac{\partial}{\partial x}\left[\frac{1}{f}\left(\frac{1}{\rho s}\frac{\Delta p}{L} + \frac{\partial T}{\partial x}\right)\right]^{\frac{1}{3}} + \rho v C_p \frac{\partial T}{\partial x} - v\frac{\Delta p}{L} = q_0 \tag{7.67}$$

The full solution to this equation requires numerical methods.

Before discussing the solution to (7.67), it is instructive to gauge the relative importance of the pressure and temperature gradient terms. Obviously, if the pressure drop is small, then (7.67) reduces to (7.58). On the other hand, if the pressure drop approaches $\Delta p \sim \rho C_p \Delta T$, then its impact must be considered. A typical value for $\rho C_p \sim 1$ MJ/m^3 K and $\Delta T \sim 0.1$ K. Therefore, as long as $\Delta p << 100$ kPa (1 atm)

the impact on the temperature profile will be small. For high velocity flows or very long channels, this condition is not met and one must use the full energy equation.

In steady state He II flow, the above expression predicts a monatonically increasing temperature profile along the channel. Walstrom solved the steady state problem analytically by making the following substitutions,

$$T_0 = \frac{1}{\rho C_p}\left(\frac{q_0 L}{v} + \Delta p\right) \tag{7.68a}$$

$$x^* = \frac{x}{L} \tag{7.68b}$$

$$\tau = \frac{T}{T_0} \tag{7.68c}$$

$$\beta = fL\left(\rho v C_p\right)^3 T_0^2 \tag{7.68d}$$

and

$$c = \frac{C_p/s}{(1 + q_0 L/v\Delta p)} \tag{7.68e}$$

Note that according to the empirical fit to the heat capacity of He II (6.29b), the numerator in (7.68e) can be approximated by a constant, $C_p/s \approx 5.6$.

Consider the case where $q_0 = 0$, such that the resulting temperature gradient is entirely due to friction. In classical non-conductive fluids, this condition results in a continuous temperature increase with the slope of the temperature profile is directly proportional to the Joule-Thomson coefficient, μ_j. Figure 7.26 shows the calculated temperature profile for fixed temperature boundary conditions.

7.3.5 *Transient Heat Transport in Forced Flow He II: Numerical Solution*

There have been a number of efforts at modeling transient heat transport in forced flow He II [41–44]. In the present context, there is insufficient space to discuss the methods in detail and the reader is encouraged to consult the original references for more information. Here we summarize the methods used by Fuzier to model this problem [44].

The principal challenge to the numerical solution of (7.67) is the non-linear nature of the partial differential equation. In particular, the fractional power to the

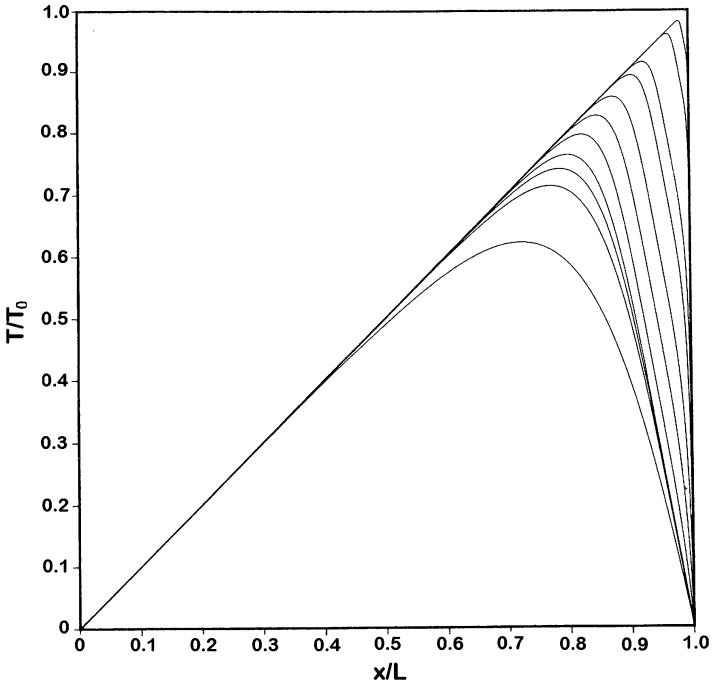

Fig. 7.26 Dimensionless temperature profile due to the Joule Thomson effect in He II forced flow with constant temperature boundary conditions. In this case, $q_0 = 0$ and $T_0 = \Delta p/\rho C_p$ (From Walstrom [40])

heat conductivity function must be handled with care to avoid numerical instabilities. Fuzier used a semi-implicit finite difference scheme to discretize the energy equation:

$$\rho C_i^n \frac{T_i^{n+1} - T_i^n}{\Delta t} - \frac{1}{\Delta x}\left[\frac{1}{f_{i+1/2}^n{}^{\frac{1}{3}} \left| \frac{\Delta P}{\rho s_{i+1/2}^n L} + \frac{T_{i+1}^n - T_i^n}{\Delta x} \right|^{\frac{2}{3}}} \left(\frac{\Delta P}{\rho s_{i+1/2}^n L} + \frac{T_{i+1}^{n+1} - T_i^{n+1}}{\Delta x} \right) \right.$$
$$\left. - \frac{1}{f_{i-1/2}^n{}^{\frac{1}{3}} \left| \frac{\Delta P}{\rho s_{i-1/2}^n L} + \frac{T_i^n - T_{i-1}^n}{\Delta x} \right|^{\frac{2}{3}}} \left(\frac{\Delta P}{\rho s_{i-1/2}^n L} + \frac{T_i^{n+1} - T_{i-1}^{n+1}}{\Delta x} \right) \right]$$
$$+ \rho v C_i^n \frac{T_{i+1}^{n+1} - T_{i-1}^{n+1}}{2\Delta x} = Q_0 + v\frac{\Delta P}{L} \tag{7.69}$$

where X_i^n represents the value of X at the node i after n time intervals. This scheme is first order accurate in time and second order accurate in space. This model was used to compare to transient heat transfer measurements on a 0.86 m long, 10 mm ID channel at fluid velocities up to 20 m/s. A uniform grid consisting of 8,000 nodal

points was used to represent the length of the test section. Time steps of order 10 μs were typically used for the solution. The initial condition before the generation of the pulse corresponds to the steady-state, linearly increasing temperature profile in the test section due to the Joule-Thomson effect.

A heat pulse that is deposited locally in a channel containing forced flow He II will produce a temperature rise that propagates along the channel at approximately the net flow velocity, v. As the thermal pulse moves along the channel, it will experience an overall increase in its background temperature due to the Joule Thomson effect. For example, at a velocity of 10 m/s and T = 1.7 K, forced flow He II increases its temperature at about 30 mK/m of channel length. In addition, the pulse temperature profile will broaden due to diffusion in the He II. The time scale for this process is similar to that discussed in Sect. 7.2, but is not generally dependent on the fluid velocity.

As an example, Fig. 7.27 displays two cases of transient heat transfer experimental results compared to the numerical model. Both are for the same base temperature, $T_b = 1.7$ K and the same heat pulse, 99 kW/m^2 for 20 ms. The only difference is the fluid velocity which is 2 m/s in Fig. 7.26a and 16 m/s in Fig. 7.26b. It is quite apparent that the He II energy equation does a good job of modeling the shape and propagation of the heat pulse. One should note that this level of agreement is not always achieved. In particular, at intermediate velocities (4 m/s $< v <$ 14 m/s), the model deviates from the experimental results. At present, this observation appears to be the result of the formulation of the solution. In the case where there is significant pressure drop, the heat flux in the He II is given by,

$$q = -\left[\frac{1}{f}\left(\frac{1}{\rho s}\frac{\Delta p}{L} + \frac{\partial T}{\partial x}\right)\right]^{\frac{1}{3}} \tag{7.70}$$

The problem occurs when the pressure drop and temperature gradient are of roughly equal magnitude and opposite sign, which can occur in regions on the trailing edge of the pulse. This is a physically unrealistic aspect of the model.

7.4 Heat and Mass Transfer in Porous Media

7.4.1 Steady Laminar Heat Transport in He II

The problem of He II heat and mass flow through porous media is significantly different from flow in wide channels. In particular, much of the porous media fluid dynamics is in the laminar regime and the transition to turbulence. Further, the geometry of porous media is not well characterized as one has with a one-dimensional channel and involves multidimensional flow. Thus, we need to consider issues of how to model the geometry of the porous media. These issues are similar to those appropriate for classical fluids in porous media, a subject introduced in Sect. 4.4.

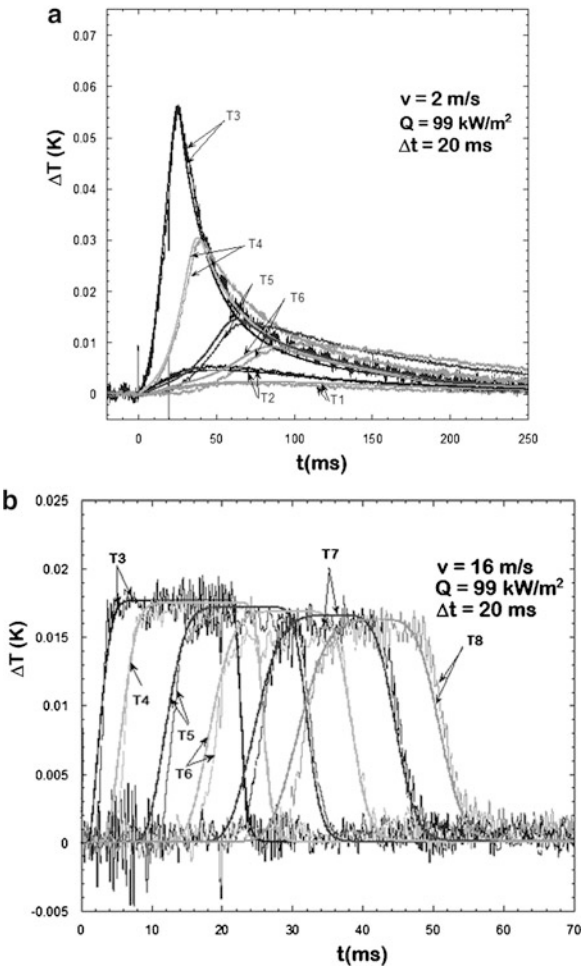

Fig. 7.27 Experimental and numerical time evolution of the temperature profile at various locations in a 0.86 m long, 10 mm ID channel. The smooth lines correspond to the numerical model. A 20 m long, rectangular heat pulse of power density 99 kW/m^2 was generated at t = 0. T_b = 1.7 K. The flow velocity: (**a**) 2 m/s, (**b**) 16 m/s [44]

As was discussed in Chap. 6, laminar flow conditions occur in He II whenever the fluid velocity is below the critical velocity. These conditions can occur even in static He II, since heat transport causes a relative velocity of the two fluid components. In He II there are two relevant critical velocities: $\mathbf{v}_{sc}$ which is associated with the onset of turbulence in the superfluid component and $\mathbf{v}_{nc}$ for the normal fluid component. $\mathbf{v}_{sc}$ depends strongly on the method by which it is measured. To remind the reader from Chap. 6, most experimental data are correlated to the empirical relationship,

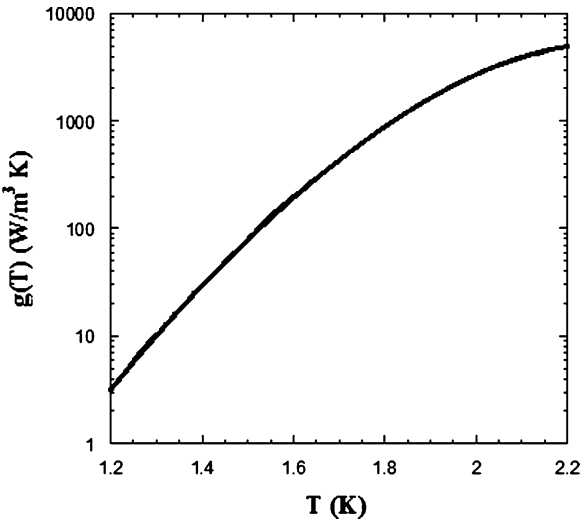

Fig. 7.28 Proportionality function in the He II laminar flow equation

$$\mathbf{v}_{sc} \simeq d^{-1/4} \quad \text{in cgs units} \tag{6.86}$$

where d is the characteristic diameter of the channel. On the other hand, the normal fluid critical velocity is interpreted in terms of classical turbulent onset such that,

$$\mathbf{v}_{nc} \approx \frac{\mu_n \mathrm{Re}_c}{\rho d} \tag{6.88}$$

where the critical Reynolds number is $Re_c \approx 1{,}200$. Note that this relationship involves the normal fluid viscosity but the total density.

Laminar heat flow in He II, which occurs for low normal fluid velocities in narrow channels, the heat conductivity equation may be written in a form similar to Fourier's law although the function of proportionality varies as the square of the diameter,

$$q = -\frac{(\rho s d)^2 T}{\beta \eta_n} \frac{dT}{dx} = -g(T) \frac{d^2}{\beta} \frac{dT}{dx} \tag{7.71}$$

where $g(T) = (\rho s)^2 T/\mu_n$. β is a numerical coefficient that depends on channel geometry; $\beta = 12$ for parallel plates and $\beta = 32$ for circular tubes. The laminar flow heat conductivity function, $g(T)$, increases strongly with temperature dominated by the dependence of $(\rho s)^2 T \sim T^{12}$. Figure 7.28 displays $g(T)$ between 1.2 K and T_λ. Appendix A.3 gives numerical values for this coefficient at saturated vapor pressure.

In the laminar flow regime, due to the isentropic nature of the system, the pressure drop due to flow is related to the temperature gradient through London's Equation,

$$\frac{dp}{dx} = \rho s \frac{dT}{dx} \tag{7.72}$$

The Fountain Effect, a unique feature of He II, can be understood in terms of this expression. Specifically, in ideal superflow, a temperature gradient induces a pressure gradient, which in practice can lead to net mass flow of the fluid.

In the laminar flow regime, the heat flow induced pressure gradient is related to the temperature gradient through London's equation. The result is given by,

$$q = -\frac{\rho s d^2 T}{\beta \mu_n} \frac{dp}{dx} = -g(T) \frac{d^2}{\rho s \beta} \frac{dp}{dx} \tag{7.73}$$

where β is the same geometrical factor as in (7.71). This relationship can be easily integrated over finite lengths and temperature difference to give practical results.

7.4.2 He II Heat and Mass Transfer Through Porous Media

In porous media, the geometry is not as well defined and the characteristic dimension, d, is more difficult to know. In laminar (Darcy) flow, the pressure gradient is related to the permeability K_D of the medium,

$$\frac{dp}{dx} = -\frac{\mu}{K_D} U \tag{7.74}$$

where U is the average approach velocity. K_D is proportional to the square of the pore diameter times the porosity, α. For a typical pore diameter $d_p = 1$ μm and porosity of 10%, that means the $K_D \sim 10^{-13}$ m^2. By analogy in the case of He II flow through porous media, one can write the laminar flow equation as,

$$\frac{dp}{dx} = -\omega \frac{\mu_n}{K_{Dn}} U_n \tag{7.75}$$

where U_n is the normal fluid velocity averaged over the sample cross section. This equation also contains the tortuosity factor, ω, to account for the increase in effective path length compared to the overall thickness of the sample. By definition, $U_n = \alpha v_n$, where v_n is the normal fluid velocity in the pores. In pure counterflow, $q = \rho s T v_n$, so one can substitute for the normal fluid velocity,

$$\frac{dp}{dx} = -\omega \frac{\mu_n}{K_{Dn}} \left(\frac{\bar{q}}{\rho s T} \right) \tag{7.76}$$

where as written $\bar{q}$ is the heat flux averaged over the sample area, $\bar{q} = \alpha q$.

In the laminar regime, He II obeys London's equation (7.72), so the temperature gradient may simply be written,

$$\frac{dT}{dx} = -\omega \frac{\mu_n}{K_{Dn}} \left(\frac{\bar{q}}{(\rho s)^2 T} \right) \tag{7.77}$$

which can be rearranged to,

$$\bar{q} = -g(T) \frac{K_{Dn}}{\omega} \frac{dT}{dx} = -\frac{g(T)}{\rho s} \frac{K_{Dn}}{\omega} \frac{dp}{dx} \tag{7.78}$$

where K_{Dn} is the permeability for the normal fluid and $g(T)$ is the temperature dependent function in Fig. 7.27.

Equation (7.78) can be used to measure the permeability of a porous medium by recording either the pressure or temperature difference across a sample subjected to a heat flux [45, 46]. Note that the the value of K_{Dn}/ω may be different from the permeability measured by other methods due to the unique properties of He II. Baudouy et al. [47] even found K_{Dn} to be temperature dependent.

Above the critical velocity, the flow through the porous media is no longer ideal and mutual friction begins to contribute to the temperature gradient. In that case, the temperature gradient through the material should be described by a modified version of (7.1),

$$\frac{dT}{dx} = -f(T,p)q^3$$

which becomes,

$$\frac{dT}{dx} = -\omega f(T,p) \left(\frac{\bar{q}}{\alpha} \right)^3 \tag{7.79}$$

where x is the dimension measured through the sample.

Equations (7.77) and (7.79) probably oversimplify the difficulty in calculating the temperature gradient in He II counterflow through porous media. The quantities, K_{Dn}, α and ω are at best approximately known and depend on the method of measurement. In the turbulent regime, the situation is even more complex due to the non-linear heat equation (7.1). In the porous medium, the channel cross section can vary significantly through out the material. Since the temperature gradient is proportional to q^3, regions that constrict the flow will have an even larger effect on the temperature difference. In fact, there is not much known about the behavior of the Gorter-Mellink equation in regions of high gradient. Thus, this is a topic worthy of continued study.

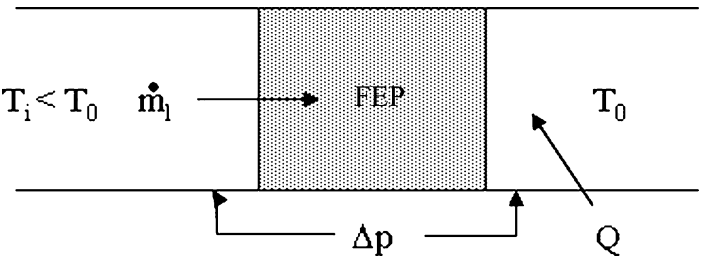

Fig. 7.29 Schematic of a Fountain effect pump

7.4.3 He II Fountain Pumps

Fountain Effect Pumps (FEPs), shown schematically in Fig. 7.29, are unique to He II. Essentially, this type of pump uses the Fountain Effect to force He II to flow through a porous plug. A heater at the outlet of the pump provides the chemical potential difference to drive the fluid flow. Such a device, which has been developed and demonstrated for space based applications, usually consists of a sintered ceramic disk or plug with a heater located on the downstream side. Typical pore size of the material is of order 0.1 μm.

An ideal fountain pump obeys the London Equation and produces a pressure head corresponding to the temperature difference produced by a heater downstream of the flow. If one integrates the London equation (7.72) along lines of constant chemical potential the corresponding static pressure head is given in Fig. 7.30. Thus, for an ideal fountain pump, the maximum pressure head is about 50 kPa for a bath at 1.8 K. Higher pump heads can be accomplished by running several pumps in series. However, the pump head decreases significantly with increasing mass flow rate.

For an ideal fountain pump, the corresponding mass flow rate is given by the relationship,

$$Q = \dot{m} S_o T_o \tag{7.80}$$

where the subscript o applies to the conditions at the pump outlet. This relationship suggests that the pump flow rate can be increased by simply adding more heat downstream, but there are limitations [49]. In a FEP, the addition of heat increases the temperature of the helium on the upstream side of the pump due to the removal of the superfluid component. This heat must be extracted by a He II refrigeration system to maintain low temperature at the pump inlet. Another important limit is the onset of turbulence above the superfluid critical velocity. To avoid this limit the design a fountain pump must have sufficient cross sectional area to ensure that the velocity within the pores does not exceed v_c, typically about 100 mm/s for porous media.

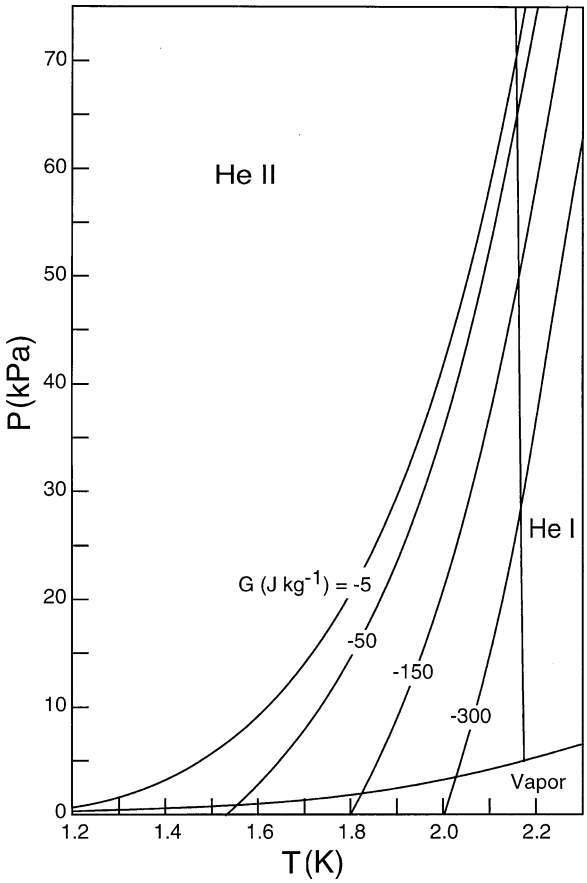

Fig. 7.30 He II phase diagram showing lines of constant chemical potential [48]

For a porosity of 30%, this velocity corresponds to an approach velocity of about 30 mm/s. Equation (7.80) can be rearranged in terms of the inlet conditions to yield,

$$\dot{m} = \frac{\dot{Q}}{(1 + C_p/s)\Delta p/\rho + s_i T_i} \tag{7.81}$$

where s_i is the entropy at the inlet to the fountain pump and Δp is the hydraulic pressure head.

Another limitation to the application of FEP is the overall low thermodynamic efficiency. For an ideal FEP, the ideal thermodynamic efficiency is given as,

$$\eta = \frac{\Delta p}{\rho q} = \frac{1}{1 + C_p/s} \cong \frac{1}{6.6} = 15\% \tag{7.82}$$

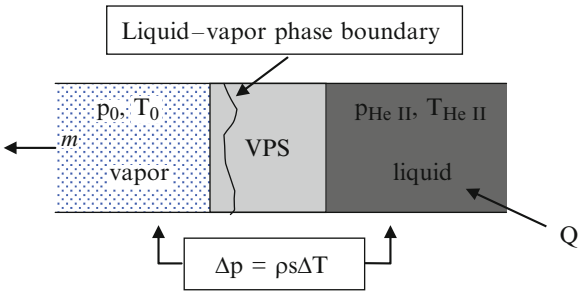

Fig. 7.31 Schematic of a vapor phase separator

However, this is an upper limit and real pumps have even lower performance. This efficiency should be compared to typical mechanical pump efficiencies which is of order 50%. Therefore, the main advantage of a fountain pump is in its ease of application. The pump consists of a heater and porous plug. There are no moving parts.

The design of practical FEPs goes beyond the above discussion. To maintain ideal flow conditions in the pump corresponding to an approach velocity below a few 10s mm/s, the pump surface area is frequently much larger than the pipe cross section in the attached flow circuit. If these conditions are exceeded, pump performance will degrade; however, the FEP will continue to pump the helium until the inlet temperature exceeds T_λ.

7.4.4 He II Vapor: Liquid Phase Separators

Another unique application for porous media is with He II- vapor phase separators (VPS) that have been developed for containment of He II in space applications. A VPS consists of a porous plug, frequently made from sintered stainless steel powder, which extracts the heat from a He II reservoir by allowing evaporation at the surface of the plug. In this application, the characteristic pore size is larger than for the FEP, because it is required to have some flow of the normal fluid component to ensure operation. A schematic of a VPS is shown in Fig. 7.31.

A He II-vapor phase separator provides a pressure difference across it given by the London equation (7.72). In use, the upstream side of the phase separator is wetted with He II while the downstream side is pumped to low pressure, lower than the saturated vapor pressure of the liquid. The phase separator works in the following way. Heat generated in the He II reservoir is carried through the porous plug by thermal counterflow to the liquid-vapor interface, which preferably occurs within the body of the plug. The heat is then removed by evaporation of the liquid at low pressure. The associated temperature difference across the plug provides the fountain pressure to hold the liquid within the He II reservoir. The total vapor mass flow is determined by this rate of heat generation, $\dot{m} = Q/h_{fg}$. To supply the vapor,

liquid must flow through the plug to the liquid-vapor interface. The heat flow in the liquid is also given by,

$$Q = \alpha A \rho s T (v_n - v) \tag{7.83}$$

where A is the plug cross section and α is the void fraction. Setting the two forms of the heat flow equal to each other and substituting $v = \dot{m}/\rho\alpha A$ one obtains an expression for the pressure drop as a function of v_n. Then assuming purely laminar flow in the phase separator, $v < v_c$, the critical velocity, the mass flow rate can then be written as,

$$\dot{m} = \frac{\rho K_{Dn}}{\beta \eta_n} \left(\frac{sT}{sT + h_{fg}} \right) \frac{\Delta p}{L} \tag{7.84}$$

where K_{Dn} is defined in (7.75). This relationship appears to fit experimental data for small mass flow rates. If the velocity within the plug exceeds v_c, turbulence in the superfluid degrades the performance and the mass flow increases more slowly with Δp.

The design of a porous plug phase separator is dependent on first knowing the mass flow needed to extract the heat load to the He II reservoir. The pressure drop across the plug is determined by the desired operating temperature of that reservoir. The physical dimensions and pore size of the porous plug follow by analysis of (7.84). Most phase separators developed for space applications consist of a sintered stainless steel structure with a typical pore size is between 1 and 10 μm [50, 51].

7.5 Kapitza Conductance

A very different problem of heat transfer in He II relates to that which occurs at an interface between a solid and the liquid. This process is in contrast to heat transport in the bulk fluid, which has been the subject so far. Surface heat transfer is more controlled by the interfacial character, including the properties of the solid state, rather than that of the bulk He II. In general, there are two regimes of surface heat transfer in He II as exemplified by the two positive slope portions of the heat transfer curve; see Fig. 7.1. At low ΔT, no boiling occurs and the heat transfer is controlled by a phenomenon called Kapitza conductance. At high ΔT and for heat fluxes greater than q^*, the surface is blanketed by a film of He I or vapor or both. In this region, the heat transfer is determined primarily by the character of the vapor film. The present section concerns itself with the first problem, that of heat transfer directly from the solid surface into the liquid He II or Kapitza conductance. Section 7.6 overviews the subject of film boiling heat transfer.

Thermal boundary conductance occurring at the interface between a solid and liquid He II was first studied by Kapitza [52] in 1941 during an experiment on the flow of heat around a copper block immersed in the liquid. Within the liquid helium

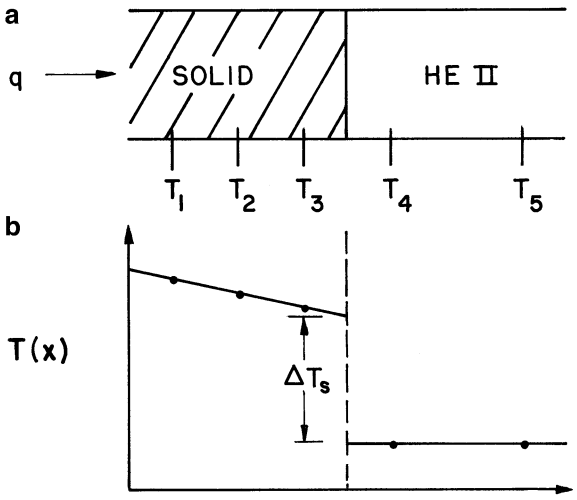

Fig. 7.32 Schematic of Kapitza conductance experiment: (**a**) temperature sensors located in the vicinity of a solid-He II interface and (**b**) temperature profile

the temperature gradients were seen to be negligible; however, a sizable temperature difference did occur between the copper block and the He II. This discovery spawned a considerable quantity of fundamental and applied research some of which is discussed in the present section. However, Kapitza conductance is also of great technical interest because it often results in the largest temperature differences in a He II heat transfer problem. For an order of magnitude comparison, a heat flux of 1 kW/m^2 can lead to a temperature difference of about 0.1 K across an interface due to this effect. Within turbulent He II the same heat flux would require about 1,000 m of one-dimensional channel to produce an equivalent temperature difference!

The general term Kapitza conductance has taken on much broader connotation over the years since its discovery. In particular, it now refers to the interfacial thermal boundary conductance which occurs between any two dissimilar materials where electronic transport does not contribute. Thus, Kapitza conductance occurs at the interface between a metal and water at room temperature. However, since the effect is strongly temperature dependent it makes a negligible contribution to the heat transfer coefficient except at low temperatures. For example, Kapitza conductance does contribute to the heat transfer process between a metal and He I at high heat flux, as is discussed in Chap. 5, but in general is neglected in classical fluid heat transfer because the thermal boundary layer dominates the process.

The measurement of Kapitza conductance is achieved by a method shown schematically in Fig. 7.32a. A solid of some finite thermal conductivity is in intimate contact with He II in a one-dimensional configuration. The temperature at various points within the solid and He II are measured as they vary with applied heat flux q. In the steady state, a temperature profile is obtained as shown schematically in Fig. 7.32b. The profile can be extrapolated to the He II-solid

interface to determine the surface temperature difference ΔT_s. By this method, the bulk properties of the two media can be eliminated from the measured temperature differences.

Kapitza conductance usually is given an empirical definition; ideally defined in the limit where q and ΔT_s are vanishingly small,

$$h_{K_0} = \lim_{\Delta T_s \to 0} \frac{q}{\Delta T_s} \tag{7.85}$$

where the 0 subscript refers to the limit as $\Delta T_s \to 0$. This quantity has a fairly strong temperature dependence going as T^n with n varying anywhere between 2 and 4. A more general definition of Kapitza conductance simply relates it to finite values of q and ΔT_s:

$$h_K = \frac{q}{\Delta T_s} \tag{7.86}$$

Because of its nonlinear nature, definition (7.86) is of more practical interest to engineering applications.

There are a number of applications for He II where knowledge of the Kapitza conductance is of substantial importance. In refrigeration involving He II, its value strongly impacts the proper design of components, particularly heat exchangers. Because of the strong temperature dependence, the importance of Kapitza conductance to heat transfer problems increases with decreasing temperature. In very-low-temperature dilution refrigeration the Kapitza conductance becomes the dominating heat transfer process. Knowledge of the Kapitza conductance of materials at higher temperatures, $T > 1$ K, is also important. Here the desire is to cool large devices such as superconducting magnets or space instruments. For proper design of these devices, it is necessary to have a good knowledge for the effective heat transfer coefficient.

Although Kapitza conductance is an experimentally defined quantity, there has been considerable theoretical work aimed at understanding this complex phenomenon. Therefore, before discussing the empirical behavior of h_K any further, a review of the physical theories used to explain its behavior is presented.

7.5.1 Phonon Radiation Limit

The first theory to successfully characterize the qualitative features of Kapitza conductance is referred to simply as the phonon radiation limit [53, 54]. The model is an overestimate of the true Kapitza conductance because it includes too many energy transport mechanisms. However, the theory does show the proper temperature dependence of h_K.

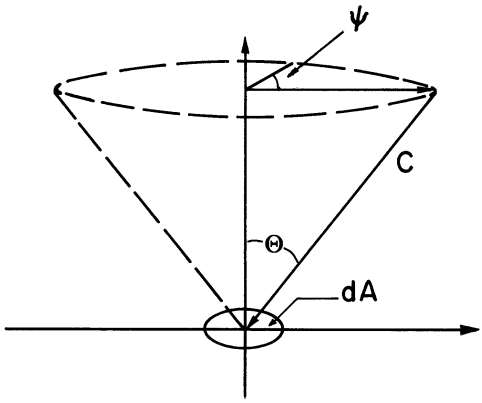

Fig. 7.33 Hemispherical region surrounding an elemental surface area for phonon heat transfer

A body above absolute zero contains thermal energy, which in the case of insulators is in the form of a phonon spectrum while for conductors it may be due partially to the electrons. Phonons are quantized lattice vibrations and are analogous to photons, which of course are quantized electromagnetic radiation. Ignoring for the moment any effect electrons may have on these concepts, it is reasonably straightforward to identify the phonon energy spectrum for a particular solid (see Chap. 2). Since the Kapitza conductance is mainly of interest at low temperatures, it is not a bad approximation to use the Debye theory to describe this energy spectrum. In the Debye model, the internal energy may be written as a temperature-dependent quantity,

$$E_{\text{ph}} = aT^4 \tag{7.87}$$

where $a = \frac{3}{5}\pi^4 (N/V)\, k_B/\Theta_D^3$ and $T \ll \Theta_D$, the Debye temperature. For most solids, the Debye temperature is in the range of several hundred Kelvin, making this approximation quite reasonable for the Kapitza conductance at helium temperatures.

To quantify the problem of phonon radiation between two media, assume there is a unit interfacial area dA on which phonons are incident at velocity c. A schematic of the hemispherical region surrounding this elemental area is shown in Fig. 7.33. The angle of incidence of the phonon is given in spherical coordinates by θ and Ψ, but only the perpendicular component of the incident phonon transmits the energy. More detailed theory discussed later includes the coupling of transverse phonons at the interface, but for simplicity the present treatment will neglect this effect. The perpendicular component of the velocity can be writtenin terms of the angle θ such that

$$c_\perp = c \cos\theta \tag{7.88}$$

The heat flux into the area dA is the then product of the energy density and perpendicular velocity component such that $dq = c_\perp E_{ph}$. It follows that the net heat

flux per unit area is obtained by integration of dq over the hemisphere in θ and Ψ. This procedure yields

$$q = \frac{1}{4\pi}\int_0^{2\pi} cE_{\text{ph}} \sin\theta \cos\theta d\theta = \frac{1}{4} cE_{\text{ph}} \tag{7.89}$$

In the Debye approximation, the speed of sound in a solid is given as

$$c = \frac{k_B \Theta_D}{\hbar}\left(\frac{6\pi^2 N}{V}\right)^{-1/3} \tag{7.90}$$

where for solids c is of the order of 3 km/s while for He II the speed of sound never exceeds 240 m/s. Substituting (7.90) and (7.87) into (7.89), we obtain an equation for the total heat flux carried by phonon radiation:

$$q = \sigma T^4 \tag{7.91a}$$

and

$$\sigma = \frac{\pi^4}{10\hbar}\left(\frac{k_B}{\Theta_D}\right)^2\left(\frac{3N}{4\pi V}\right)^{2/3} \tag{7.91b}$$

The reader who is familiar with radiation heat transfer should recognize this form to be analogous to the heat transported by photon radiation. Note that (7.91b) includes the variable material properties through the molar volume (N/V) and Debye temperature. The quantity σ can vary considerably between materials, which according to the theory leads to a quite different heat transfer coefficients. For example, since σ is inversely proportional to c^2, it follows that the ratio of heat fluxes by phonon radiation should differ by a factor of 100 between He II and solids at low temperatures. This is one of the major weaknesses of the phonon radiation theory in that it only considers the thermal character of the solid.

Now consider the radiation of phonons between two different media, between which there exists an interface. For the sake of discussion, assume there is no appreciable temperature gradient occurring in either bulk material and that the flow of heat from one side to the other produces an interfacial temperature difference ΔT_s. In order for this interface to be defined as a boundary between two bulk media, it must be confined to a thickness that is small compared to the characteristic phonon wavelength, $\lambda_D = hc/k_B\Theta_D$. For solids $\lambda_D \approx 100$ μm, which is large compared to most interfacial dimensions.

The net heat flux through the interface is actually a difference between two values, the radiant energy incident on the high-temperature side, $q(T + \Delta T)$, minus that incident from the low-temperature side, $q(T)$,

$$q_{\text{net}} = q(T + \Delta T) - q(T) \tag{7.92}$$

Assuming that both these quantities can be described in terms of the phonon heat flux expression (7.91a) and also that the coefficient σ is the same in either media, it follows that the net heat flux is a difference between the phonon radiation expressions of the two media:

$$q_{\text{net}} = \sigma(T + \Delta T)^4 - \sigma(T)^4 \tag{7.93a}$$

which can be expanded to

$$q_{net} = 4\sigma T^3 \Delta T \left[1 + \frac{3}{2}\frac{\Delta T}{T} + \left(\frac{\Delta T}{T}\right)^2 + \frac{1}{4}\left(\frac{\Delta T}{T}\right)^3\right] \tag{7.93b}$$

In the limit of small ΔT, (7.93b) gives an explicit definition for the phonon radiation limit Kapitza conductance in terms of σ:

$$h_K^p = 4\sigma T^3 \tag{7.94}$$

where the superscript p refers to the phonon radiation limit. The assumption that σ is independent of media clearly is not accurate, particularly when dealing with interfaces between solids and He II. However, it is argued that the smaller value of σ (that of the solid) controls the heat transfer because the net heat flux q_{net} must be in the direction from high to low temperature. As a reference point, the phonon radiation limit applied to copper ($\Theta_D = 343$ K, $N/V = 0.86 \times 10^{23}$ cm^{-3}) predicts a Kapitza conductance of

$$h_K^p = 4.4T^3 \text{ kW/m}^2 \cdot \text{K} \tag{7.95}$$

or 30 kW/m^2 K at 1.9 K. We now compare the Kapitza conductance predicted by the phonon radiation limit with experiment values.

Listed in Table 7.3 are calculated values from the phonon radiation limit and the highest values obtained experimentally for typical metals and nonmetals. It is important to note that the experimental values for the same material vary considerably, in some cases by as much as an order of magnitude. However, since the phonon radiation limit should represent an overestimate of h_K, it is most appropriate to compare it to the highest measured values. The first result gleaned from this comparison is that the phonon radiation calculation always gives values for h_K that are higher than experiment, sometimes by as much as an order of magnitude. This fact is consistent with the understanding that the phonon radiation limit overestimates h_K. Second, although it is not apparent from the tabular data, the general temperature dependence of h_K predicted by the phonon radiation limit is borne out. Recall that experiment yielded a form for $h_K \approx T^n$ with $2 < n < 4$. Finally, as with the phonon radiation limit, there is a measurable dependence of h_K on the value of Θ_D for the particular solid. This fact can be seen most clearly in Fig. 7.31, which is

Table 7.3 Comparison of highest experimental values for the Kapitza conductance with the phonon radiation limit (Compiled by Snyder [54])

Solid	Θ_D (K)	h_K^P (1.9 K) (kW/m^2·K)	h_K (1.9 K) (kW/m^2·K)
Hg	72	440	30
Pb	100	190	32
In	111	171	11
Au	162	155	8.8
Ag	226	55	6
Sn	195	54	12.5
Cu	343	30	7.5
Ni	440	19	4.0
W	405	18	2.5
KCI	230	22	6.9
SiO_2 (quartz)	290	19	5.7
Si	636	6.4	4.2
LiF	750	5.1	4.5
$A1_2O_3$	1,000	1.5	1.6

a log plot of h_K versus Θ_D^{-1}. The linear interpolation indicates there is a coloration of the form

$$h_K \propto \Theta_D^{-n} \tag{7.96}$$

where the phonon radiation limit predicts $n = 2$ and experiment, as shown in Fig. 7.34, yields values of $n \approx 1$.

There are a number of problems with the phonon radiation limit, particularly when it applies to solid–He II interfaces. It is clearly a crude approximation to a complex problem and is limited by the numerous factors incorrectly accounted for in the theory. These factors include:

1. A failure to distinguish adequately between the different media on either side of the interface. The Debye temperatures that enter the problems are associated with the solid media. Any correction to the theory should include the characteristics of both media.
2. An assumed coupling between both longitudinal and transverse phonon modes. This is particularly a problem for He II where transverse phonons cannot be sustained.
3. Reflections at boundaries are not considered, implying a perfect transmission coefficient. This assumption clearly overestimates the heat transport. A finite reflection coefficient at the interface would be expected, particularly for solid–He II interfaces where the phonon spectra are so different.
4. Crystal structure at the interface is ignored. This is potentially an important factor owing to the solid having long-range order while the liquid is not periodic.
5. Phonons are assumed to be the only heat transport mechanism. However, some experiments have shown that electrons in metals play a significant role in the heat transfer at the interface.

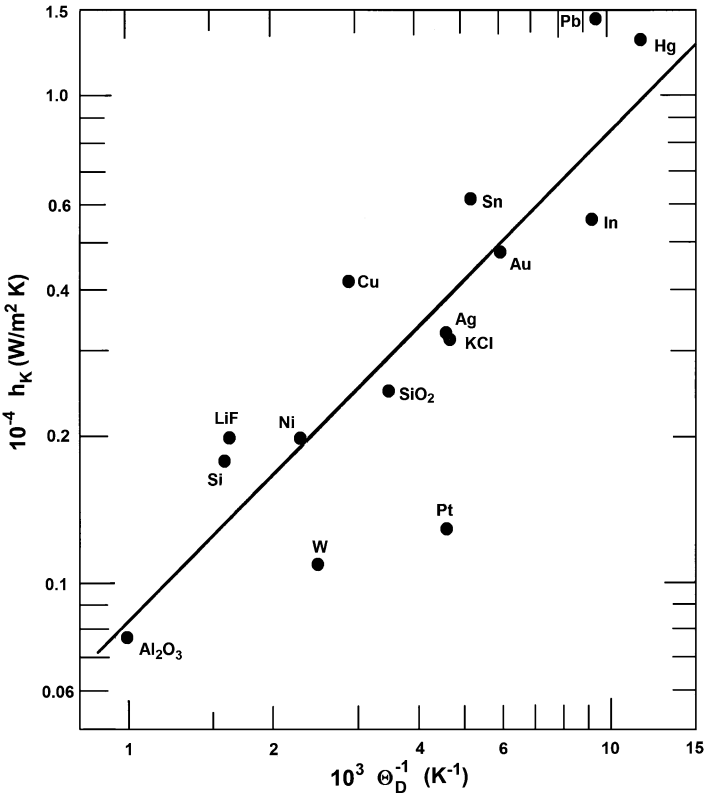

Fig. 7.34 Kapitza conductance at 1.5 K —largest values observed for each solid (Compiled by Challis [55])

6. The existence of interfacial films or impurities is not considered. Layers of adsorbed impurities can have substantial effect on the heat transfer from practical surfaces. However, even for clean surfaces the detailed character of the helium adjacent to the interface must be considered.

The above factors are part of improved theories of Kapitza conductances. The first such improvement was due to Khalatnikov in 1952 [56]. It basically addresses the first three objections to the phonon radiation limit as listed above.

7.5.2 Acoustic Mismatch Theory

The first real advance in the theory of Kapitza conductance was made by the development of the acoustic mismatch theory of Khalatnikov [56]. This theory is based on an analogy with classical acoustics or boundary scattering in optics.

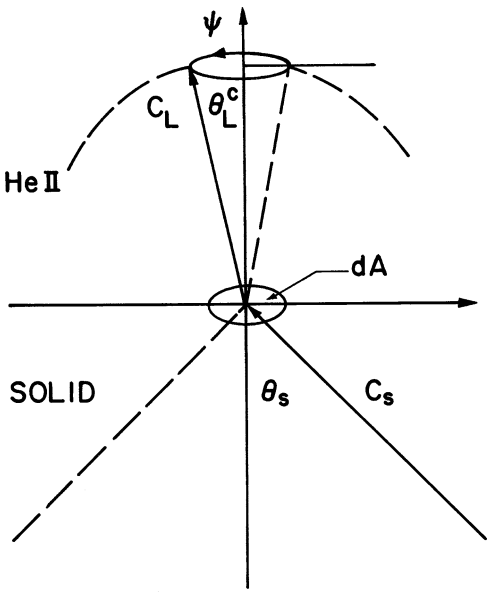

Fig. 7.35 Schematic of interface between solid and He II

In some ways the theory is similar to the phonon radiation limit except that it includes a very important additional mechanism; that of the finite reflection coefficient at the boundary between the two media. The basic approach involves the derivation of the phonon transmission coefficient using conservation of momentum and energy at the boundary. Because the acoustic mismatch theory explicitly accounts for the difference between the two media, it is expected to be a better description for the solid–He II case where the speed of sound differs by an order of magnitude on either side of the interface.

Consider an interfacial region between two media, for example, a solid and He II. This example is of current interest so it will be emphasized throughout the following discussion. The liquid is able to transmit only longitudinal phonons. A schematic of the interface is shown in Fig. 7.35. By analogy with optics, these regions can be thought of as a low-refractive-index solid adjacent to a high-refractive-index liquid. Because of the difference in refractive index, a phonon that is incident on the boundary from the liquid side would be reflected off the interface unless its angle of incidence is less than a critical value, θ_L^c. Within this angle the transmitted phonons are diffracted to an angle θ_s, on the solid side. The locus of maximum angles θ_L^c forms a cone of transmission which is determined solely by the speed of sound ratio in the two media:

$$\theta_L^c = \arcsin\left(\frac{c_L}{c_s}\right) \tag{7.97}$$

For interfaces between metals and He II, the ratio c_L/c_s is about 0.1, which corresponds to a critical angle of about 6°. The acoustic mismatch theory assumes

that phonons strike the interface between the two media at an angle θ_s, but only those that are scattered into an angle less than θ_L^c can be transmitted. All other phonons are reflected internally.

The above argument can be extended to describe the phonon heat transport across an interface. The total heat transport is determined by integration over the cone of transmission, much as was accomplished above for phonon radiation although now only angles less than θ_L^c are allowed:

$$q = \frac{1}{4\pi}\int_0^{2\pi} d\Psi \int_0^{\theta_L^c} c_L E_{\text{ph}} \sin\theta\cos\theta d\theta = \frac{1}{4} c_s E_{\text{ph}} \left(\frac{c_L}{c_s}\right)^3 \tag{7.98}$$

Note that (7.98) is similar in form to the phonon radiation limit result except that it is modified by the ratio $(c_L/c_s)^3$, which for solid–He II interfaces is of the order of 10^{-3}.

The above expression theoretically predicts the heat transport carried by phonons that are refracted into the angle θ_L^c. However, not all phonons that fall within this cone are actually transmitted, because there is a finite transmission coefficient for phonons incident on the boundary. This transmission coefficient t is given in terms of the acoustic impedance Z of each medium:

$$t = \frac{4Z_L Z_s}{(Z_L + Z_s)^2} \tag{7.99}$$

where $Z_L = \rho_L c_L$ and $Z_s = \rho_s c_s$. For the case concerning the solid–He II interface it is apparent that $Z_s \gg Z_L$ and (7.99) can be simplified such that

$$t = 4\frac{Z_L}{Z_s} = 4\frac{\rho_L c_L}{\rho_s c_s} \tag{7.100}$$

As an example, consider the interface between He II and copper. In this case $Z_s \approx 10^3 Z_L$, which corresponds to a transmission coefficient of approximately 0.5%.

Combining the equations for the heat flux (7.98) and the transmission coefficient (7.100), we find that an expression for the transmitted heat flux is

$$q_t = q \times t = \left(\frac{\rho_L c_L^4}{\rho_s c_s^4}\right) c_s E_{\text{ph}} \tag{7.101}$$

which is similar to the phonon radiation limit except for the extra term in the parentheses.

An additional aspect to the acoustic mismatch theory concerns the fact that the fluid can sustain only longitudinal phonons. Instead of the expression for the energy density used in the phonon radiation limit, in the acoustic mismatch theory the expression must include only longitudinal phonons. Thus, the corresponding form for the energy density is

$$E_{\text{ph}}^{L} = \frac{4\pi^5 k_B^4 T^4}{15\hbar^3 c_L^3} \tag{7.102}$$

Combining the energy density equation for longitudinal phonons (7.102) with the transmitted heat flux, we obtain q_t given by (7.101), a temperature-dependent expression for the transmitted heat flux:

$$q_t = \frac{4\pi^5 k_B^4 \rho_L c_L}{15\hbar^3 \rho_s c_s^3} T^4 \tag{7.103}$$

As with the phonon radiation limit it is possible to replace the prefactor in (7.103) by σ.

The net heat flux across the interface is obtained by subtracting the incident flux on either boundary. By suitably redefining σ it is possible to use (7.93) and (7.94) to predict the Kapitza conductance in the acoustic mismatch theory. For a small interfacial temperature difference, the result is

$$h_K^A = \frac{16\pi^5 k_B^4 \rho_L c_L}{15\hbar^3 \rho_s c_s^3} T^3 \tag{7.104}$$

where the superscript A refers to the acoustic mismatch theory. Note that the expression for the Kapitza conductance derived from the acoustic mismatch theory is determined by the properties of both media, a dependence left out of the phonon radiation limit. A more rigorous calculation in the acoustic mismatch theory replaces the sound speed in the solid, c_s, by its transverse component, c_t.

It is more convenient to have an expression for the Kapitza conductance in terms of the Debye temperature and other properties of the media. By replacing the transverse speed of sound c_t by its expression in terms of the Debye temperature Θ_D, a simplified expression is obtained:

$$h_K^A = \left(\frac{6\pi^4}{5}\right) \frac{RF\rho_L c_L T^3}{M\Theta_D^3} \tag{7.105}$$

where $R = 8.31$ J/mol K is the universal gas constant and M is the molecular weight. The multiplicative factor F, which is a function of the ratio c_t/c, is included, but for most solids, F is of the order of unity and so is not a particularly important factor in (7.105). For helium properties at saturation pressure and assuming $F = 1.6$, we can simplify to a useful form,

$$h_K^A = 5.5 \times 10^7 \left(\frac{T^3}{M\Theta_D^3}\right) \quad \left(\text{kW/m}^2 \cdot \text{K}\right) \tag{7.106}$$

where M is in units of g/mol. As is the case with the phonon radiation limit, the acoustic mismatch theory predicts a variation of h_K^A with the Debye temperature as $h_K^A \approx \Theta_D^{-3}$. This dependence is similar to that of the phonon radiation limit, $h_K^P \approx \Theta_D^{-2}$. However, both theoretical approaches overestimate the experimentally determined Debye temperature variation, $h_K \approx \Theta_D^{-n}$ where $n \approx 1$.

7.5.3 Small Heat Flux Kapitza Conductance ($\Delta T \ll T$)

Now consider the relationship between the above theoretical treatments and actual experimental data. Plotted in Fig. 7.35 are model calculations and experimental data for the Kapitza conductance of a He II-copper interface at temperatures above 1.3 K. As can be seen in the figure, the phonon radiation limit forms an upper bound to experimental data consistent with the model excluding boundary scattering effects. Similarly, the Khalatnikov acoustic mismatch theory predicts a Kapitza conductance about 200 times smaller than the phonon radiation limit. Insertion of numerical values for copper into (7.106) results in the expression for the Kapitza conductance,

$$h_K^A = 0.021T^3 \text{ kW/m}^2 \cdot \text{K} \tag{7.107}$$

The experimental data displayed in Fig. 7.35 show basically the same temperature dependence with some variations. The best fit to these data indicate h_K proportional to T^n with n ranging between 2 and 4. Perhaps more surprisingly from the experimental viewpoint is that the magnitude of h_K at a given temperature varies by at least an order of magnitude among samples. Part of this variation can be attributed to surface morphology. The upper shaded region in the figure is for copper surfaces that are cleaned carefully either chemically or mechanically and perhaps recrystallized at room temperature to reduce surface strain. On the other hand, lower values are generally obtained for dirty surfaces, indicated by the lower shaded region, for which less effort was made to maintain surface cleanliness. Based on the available experimental data, approximate forms for the Kapitza conductance in this temperature range are suggested:

$$h_K \simeq 0.9T^3 \text{ kW/m}^2 \cdot \text{K for clean surface} \tag{7.108}$$

$$\simeq 0.4T^3 \text{ kW/m}^2 \cdot \text{K for dirty surface} \tag{7.109}$$

with potentially as much as a factor of two variation in value.

It can be seen from Fig. 7.36 that although the theoretical treatments bracket the experimental data, neither does a particularly good job of predicting the results. Nevertheless, the physical interpretation contained in the acoustic mismatch theory generally is believed to be correct. In fact, the theory does a much better job of interpreting the magnitude of h_K in the very-low-temperature regime, $T < 0.3$ K [57].

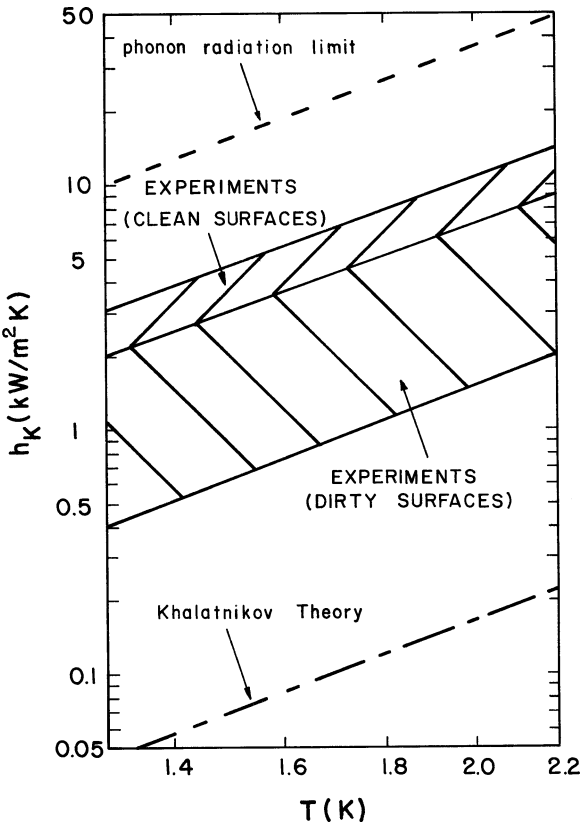

Fig. 7.36 Experimental values for the Kapitza conductance of copper between 1.3 K and T_λ (Compiled by Snyder [54])

Therefore, the problem with the theory appears to be that it does not include additional thermal coupling mechanisms which can make a large contribution, particularly at relatively high temperatures, $T > 1$ K.

A number of improvements to the acoustic mismatch theory have attempted to bring the calculations in closer agreement with experiment. One such improvement adds to the model a high-density helium layer at the interface between the solid and bulk liquid [57–60]. The existence of this layer has been demonstrated in helium adsorption studies, see Sect. 10.2. It occurs because the helium molecules are bound tightly to the surface by van der Waal interactions. Since the interfacial region consists of several components—the solid, perhaps two high-density atomic layers of solid helium, and then the liquid – it is possible to have boundary scattering occur at each of these interfaces. Finite phonon transmission and reflection coefficients can be assumed to occur at each boundary. Defining the phonon absorption coefficient v as the fraction of incident phonons that are absorbed, we can make this an adjustable parameter and fit the data to the best choice of $0 < v < 1$. This approach allows for a good fit to experimental data above 0.5 K [54].

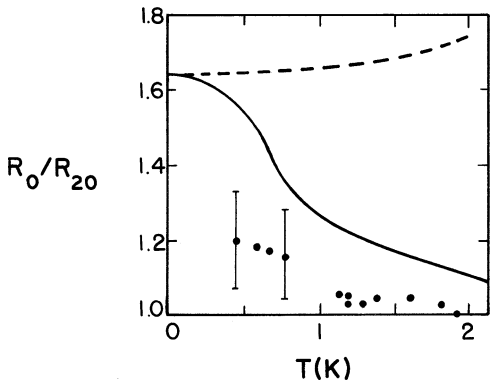

Fig. 7.37 The ratio of the Kapitza resistance under saturated vapor pressure and under a pressure of 2 MPa (R_0/R_{20}): •, experimental points; - - -, Khalatnikov theory; ——, dense-layer theory (From Wilks [61])

There are several additional features to the Kapitza conductance which are worth noting, partly because they prove the existence of additional physical processes but also because they relate to problems of applied interest. The first feature to consider is the dependence of the Kapitza conductance on externally applied pressure. Plotted in Fig. 7.37 are the ratio of the measured Kapitza resistance ($1/h_K$) at 2 MPa to that at saturated vapor pressure [58, 62]. Also displayed in the figure are two theoretical treatments, the Khalatnikov theory and the same theory modified to include the dense helium layer without finite reflection coefficients. Note first that the experimentally determined ratio is not much different from unity, particularly in the range of technical interest, above 1 K. The unmodified Khalatnikov theory on the contrary predicts a sizable effect for all temperatures, mostly due to the variation of the fluid properties with pressure. For the modified theory a smaller ratio is predicted, particularly at high temperatures, although it is still above the experimental results. Because the pressure dependence of the Kapitza conductance is not a large effect, it is generally not considered in practical calculations.

A second factor that leads to variations in h_K is the application of a magnetic field. This is an important physical observation for it indicates that there must be other heat transport mechanisms contributing at the interface. In particular, since electrons in the solid are affected by a magnetic field, there must be a coupling between electrons in the metal and phonons in the helium adding to the heat transport. Two types of experiment have been performed to investigate this effect. The first has shown a larger Kapitza conductance for a Type I superconductor for fields above B_C. For lead the ratio h_K (normal)/h_K (superconductor) has been shown to vary between 1.3 and 3 for different samples. This observation is probably the most direct evidence of some type of electron-phonon coupling at the interface. For normal metals such as copper, there have been fewer investigations of the effect of magnetic field on Kapitza conductance. Some reports have indicated h_K for normal metals increases by about 10% in a 1 T magnetic field. However, there is insufficient data available to predict this effect to higher magnetic fields.

Beyond the above two experimental features, there is evidence that the Kapitza conductance is affected strongly by the application of interfacial coatings to the solid, either in the form of applied materials or adsorbed gases. Generally, coatings decrease the apparent Kapitza conductance because they tend to the insulating materials with low thermal conductivities. The effect of a few monolayers of adsorbed gas has not been investigated thoroughly, although it has little importance for practical applications where the surfaces are not kept very clean.

7.5.4 Large Heat Flux Kapitza Conductance ($\Delta T \approx T$)

Up until this point, the theory and experiments associated with the Kapitza conductance for small ΔT have been emphasized. However, in applications of He II large heat fluxes can occur, which in turn result in large temperature differences across the interface such that $\Delta T \approx T$. Because of this occurrence, it is desirable to develop a method of handling the heat transfer process for finite ΔT. Returning to the simplest theories, either phonon radiation limit or acoustic mismatch for finite ΔT, the heat flux through the interface may be written as a sum of terms involving the ratio ($\Delta T/T$), (7.93). It follows that the Kapitza conductance for finite ΔT is larger than h_K, by the magnitude of this expansion,

$$h_K(\Delta T) = h_{K_0}\left[1 + \frac{3}{2}\frac{\Delta T}{T} + \left(\frac{\Delta T}{T}\right)^2 + \frac{1}{4}\left(\frac{\Delta T}{T}\right)^3\right] \tag{7.110}$$

where for $\Delta T/T \approx 0.5$, the bracketed quantity is approximately equal to 2. Note that the expansion given by (7.110) makes the initial assumption of an explicit T^3 dependence of h_{K0} consistent with theory. However, experimental measurements vary considerably from this exact form, obeying power laws varying between T^2 and T^4. Some additional characteristic to the Kapitza conductance may also be expected to occur when the surface temperature exceeds T_λ.

There have been several attempts [62–67] to correlate the Kapitza conductance for finite ΔT with the form of (7.110). These have not been entirely successful largely because of the deviation between the theory and experimental temperature dependence of this effect. An alternative correlation suggested [65] for practical applications is:

$$q_s = \alpha\left(T_s^n - T_b^n\right) \tag{7.111}$$

where a and n are adjustable parameters. Note that if one equation is able to fit the experimental data for one sample over the whole temperature difference range, then it should be possible to expand (7.111) consistent with the low heat flux temperature dependence. Similar to the behavior of the experimental data for small ΔT, the high ΔT Kapitza conductance also varies considerably with sample. Plotted in Fig. 7.38

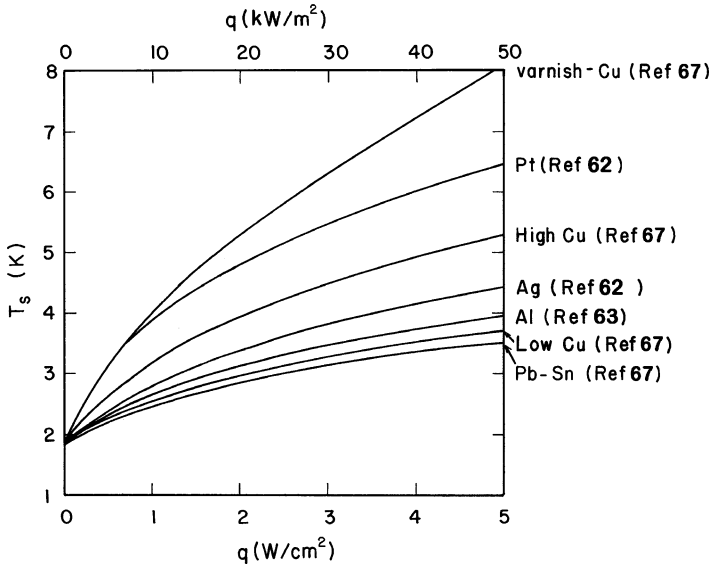

Fig. 7.38 Surface temperature versus heat flux for large ΔT Kapitza conductance

Table 7.4 High heat flux Kapitza conductance fitting parameters for metals at 1.8 K

Metal	Surface condition	T_s at 10 kW/m^2	α (kW/m^2·K^n)	n	References
Cu	As received	3.1	0.486	2.8	
	Brushed and baked	2.85	to		
	Annealed	2.95	0.2	3.8	[65]
	Polished	2.67	0.455	3.45	[67]
	Oxidized in air for 1 month	2.68	0.46	3.46	[67]
	Oxidized in air at 200°C for 40 min	2.46	0.52	3.7	[67]
	50-50 PbSn solder coated	2.43	0.76	3.4	[67]
	Varnish coated	4.0	0.735	2.05	[67]
Pt	Machined	3.9	0.19	3.0	[62]
Ag	Polished	2.8	0.6	3.0	[62]
Al	Polished	2.66	0.49	3.4	[63]

are measurements of T_s as it depends on q_s for different materials. A range of results for copper are shown which indicate the variation with surface preparation. Listed in Table 7.4 is a summary of published data for Kapitza conductance of pure metals at high ΔT. Displayed are the surface preparation, surface temperature at a heat flux $q = 10$ kW/m^2, and the best-fit functional form to these data. Note that most of the fits give values of $n = 3 \pm 0.5$, which is systematically lower than the theoretical value of $n = 4$. Also, the best fit to the coefficient in (7.111) is for $\alpha \simeq 0.05$ W/cm^2·K^{n+1} but with substantial variation. Finally, it is interesting to note that the variation in Kapitza conductances at large ΔT is not nearly as great as is obtained in the limit $\Delta T \to 0$, where an order-of-magnitude deviation in h_k is seen.

Example 7.3

Calculate the temperature of an "as received" copper surface when subjected to a heat flux of 5 kW/m^2 at 2.1 K using both the small ΔT approximation and the empirical correlation for large ΔT.

For small ΔT, the Kapitza conductance of as received (dirty) copper is given by the expression (7.109),

$$k_K = 0.4T^3 \text{ kW/m}^2 \text{ K} = 3.7 \text{ kW/m}^2 \text{ K}$$

$$T_s = T_b + q/h_K = 2.1 + 1.35 = 3.45 \text{ K}$$

For large ΔT, the empirical correlation is given by,
$q_s = a\left(T_s^n - T_b^n\right)$ where for "as received" samples $a = 0.486$ kW/m^2 K^n and $n = 2.8$.
Solving for T_s,

$$T_s = \left(\frac{q}{a} + T_b^n\right)^{\frac{1}{n}} = 2.82 \text{ K}$$

Note that this is about a factor of two difference in ΔT, being 1.35 K in the small ΔT approximation and 0.72 K in the large flux correlation.

In classical fluid heat transfer, the heat transfer coefficient usually increases with fluid velocity or Reynolds number, see Chap. 5. This is because the net flow velocity thins the boundary layer at the heater surface and induces convection. It is therefore reasonable to ask whether non-boiling heat transfer in He II can similarly be enhanced by flow. There have been several experimental investigations on this topic [68, 69].

At first glance, one would not expect enhancement to heat transfer in the Kapitza regime as long as the fluid remains below T_λ. This is because the heat exchange is controlled by phonon transport and that there is no significant thermal boundary layer contribution the heat transfer coefficient. Experiments have generally supported this position, however, the situation is not so simple when the helium locally transitions to He I by exceeding T_λ. In that case, since the fluid near the heater is either He I or vapor, the helium flow can significantly improve the process. Furthermore for local heat transfer within a tube, the action of the fluid flow will also tend to sweep the hot helium away from the heated region which will allow a more rapid recovery to the non-boiling state once the heat flux is reduced. This effect is in addition to the overall enhancement to the He II heat transport that can occur for relatively high fluid velocities, see Sect. 7.3.

7.6 Film Boiling Heat Transfer

Until now the existence of boiling phenomena in He II has been mentioned only as the condition reached when the critical heat flux q^* is exceeded. However, there are a number of complicated heat transfer processes that can occur above q^* that deserve more discussion. This regime of heat transfer is of significant technical importance for its occurrence can lead to catastrophic events in cryogenic systems where good heat transfer must be maintained continuously. Unfortunately, boiling heat transfer in He II is one of the least understood process in He II heat transfer.

In He II above the peak heat flux, the fluid in the region of heat transfer can contain several phases in coexistence. Consequently, the physical interpretation of the heat transfer processes is more difficult than in single-phase He II. For heat fluxes above q^* there occurs a discontinuous jump in the surface temperature. This transition marks the formation of a film of helium vapor, liquid He I, or both blanketing the heat transfer surface. These general characteristics of the transition to film boiling are best couched in the context of the surface heat transfer curve such as Fig. 7.1. In the film boiling state, the heat transfer is much less effective because of the low thermal conductivity vapor film insulating the surface from the bulk He II. Typical values for the film boiling heat transfer coefficient $h_{fb} = q/\Delta T_s$ are 10–100 times smaller than the Kapitza conductance coefficient. However, these values are strongly dependent of a number of physical parameters including heater configuration, bath temperature, pressure, and saturated versus subcooled liquid state. An additional feature in the heat transfer curve, also commonly observed in He I, is the occurrence of a recovery heat flux q_R that is less than q^*. The existence of $q_R < q^*$ causes hysteresis in the heat transfer curve, see Fig. 7.1. However, unlike pool boiling He I, this hysteresis is not observed universally in all He II heat transfer experiments.

There are three possible film boiling conditions that can exist in He II above q^*. To establish which condition is expected for a given set of externally imposed factors, it is necessary to consider the helium state in the vicinity of the heat transfer surface. The first condition corresponds to the local pressure at the heated surface being less than the saturation pressure at the λ-point, that is $p_\lambda = 5.04$ kPa. This is referred to as the saturation boiling condition. It is achieved by having a local temperature excursion above T_{sat}, the saturation temperature at the local pressure. The resulting boiling state is a coexistence of two phases; saturated vapor and He II.

The second condition occurs when the local pressure at the heat transfer surface is large enough to exceed p_λ at the heat transfer surface. A consequence of exceeding q^* is the production of a film of low-thermal-conductivity He I which covers the surface. If the heat flux q is not greater than the corresponding critical heat flux in He I for that configuration, the heat transfer process will be stable, allowing nucleate boiling to occur in the He I film and heat conduction in He II. Note that the boundary between the He II and He I is not clearly defined in this case because the phase transition from He I to He II is second order, allowing only a continuous density profile. It is important to be aware that, because q^* in He II is under most circumstances much higher than that in He I, the limiting of this process to two phases usually only occurs for temperatures near T_λ.

The third boiling condition occurs at the solid-helium interface when q^* is exceeded in subcooled He II for temperatures well below T_λ, that is $T_b < 2.1$ K. In this regime, the critical heat flux is greater than that in He I and the He I film becomes unstable and enters film boiling. The result is a triple-phase process consisting of vapor film blanketing the surface, a very thin He I film, and bulk He II. As with the second condition, the He I-He II boundary is not sharply defined. It is apparent that this third film boiling condition, although occurring commonly in engineering systems employing subcooled He II, is the most complex to understand because of the existence of multiphase processes.

There exists one additional type of boiling in He II which does not fall in any of the three above categories. This type of boiling occurs in the bulk fluid rather than at the interface. It can be achieved only in special configurations where the surface heat flux does not exceed q^* but the channel heat flux surpasses the local boiling condition. For example, this condition was discussed in the context of the design of static He II heat exchangers, Sect. 7.1.4. As a result, He I and vapor are nucleated in the bulk and the heat transport properties of the fluid are modified. This process is analogous to bulk boiling in ordinary fluids.

The fundamental description of the film boiling heat transfer clearly requires a more complex theoretical description than considered so far. Furthermore, it appears that there is no broadly applicable theory capable of handling the multiphase boiling processes. As a result, most research on this problem is of the category of engineering correlations combined with empirical evidence. Since the understanding of the process relies heavily on suitable experimental data, a review of measurements of film boiling heat transfer coefficients is presented first. Subsequently, a comparison is made between the available theories and experimental results. Finally, a description is included of some of the less understood heat transfer phenomena such as recovery from the film boiling state and time-dependent effects.

7.6.1 Film Boiling Heat Transfer Experiments

The film boiling heat transfer process depends strongly on several factors. The first of these has to do with the configuration of the heater. Experiments to date have mainly focused on two heater configurations, flat surfaces and round wires. In the case of the flat surfaces, some are placed at the end of a He II duct while others are in an open bath. Round wire heat transfer experiments are almost all done within an open bath. Recall that the onset of film boiling is determined by the integrated thermal gradient in the He II, thus in a one-dimensional linear geometry the duct length and cross section are important factors affecting q^*. On the other hand, in a cylindrical geometry, as discussed in Sect. 7.1.4, the thermal boundary layer is restricted to occur within a few radii of the heater. Thus, the heat transfer from cylinders can be studied in a large bath without loss of generality.

The experimental measurements of the film boiling heat transfer coefficient for various heater configurations have been extensive; however, they have also been rather restrictive in regime of investigation. The most obvious restriction is

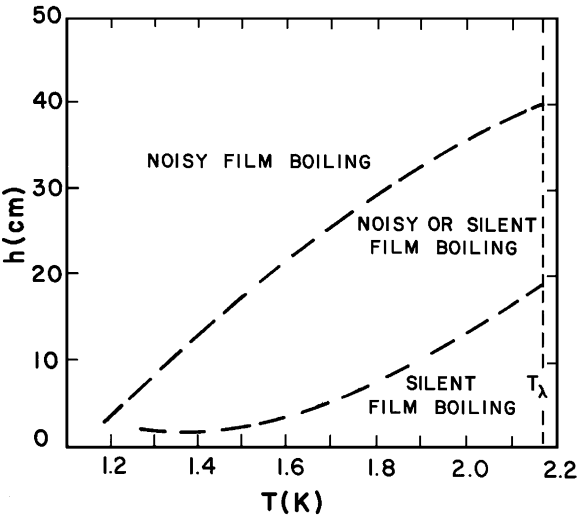

Fig. 7.39 Regimes of noisy and silent boiling from wire heaters in saturated He II (From Leonard [70])

associated with the total allowable heat transfer, which is a system limitation. Therefore, film boiling heat transfer surfaces are usually much less than 1 cm^2 in area, which places rather strict constraints on the sample. Historically, most experiments have been carried out in near saturated He II, leading to a boiling state consisting of vapor-He II coexistence. More recently, more measurements have been performed in subcooled He II primarily due to the interest in its application in large superconducting magnet systems. Thus, the second important factor impacting the film boiling heat transfer process is the state of the He II bath; mainly its temperature and pressure.

In near saturation He II, there exist two different regimes of film boiling heat transfer. These are referred to as "noisy" and "silent" boiling. Noisy boiling is apparent by the existence of audible sound emanating from the heat transfer region. Silent boiling, on the other hand, is film boiling without this audible sound. Frequencies observed in noisy boiling can vary anywhere from a few Hz to tens of kHz. The frequency is generally a function of heat flux although in no well-established pattern. The regions of noisy and silent boiling are seen to depend on bath temperature and depth of immersion.

Plotted in Fig. 7.39 is a map of these two regimes based on one set of data on wire heaters [70]. This map should not be construed as universally applicable. It appears from these results that noisy boiling occurs for larger immersion depths and lower temperatures. The occurrence of noisy or silent boiling also has a significant effect on the heat transfer coefficient h_{fb}. In regimes of overlap where either noisy or silent boiling is seen to occur, it is usually the case that a slightly higher heat transfer coefficient is measured during silent boiling. This effect, which appears systematic in published experiments, is nonetheless only of the order of 10–20% in the majority of reported results [71–75].

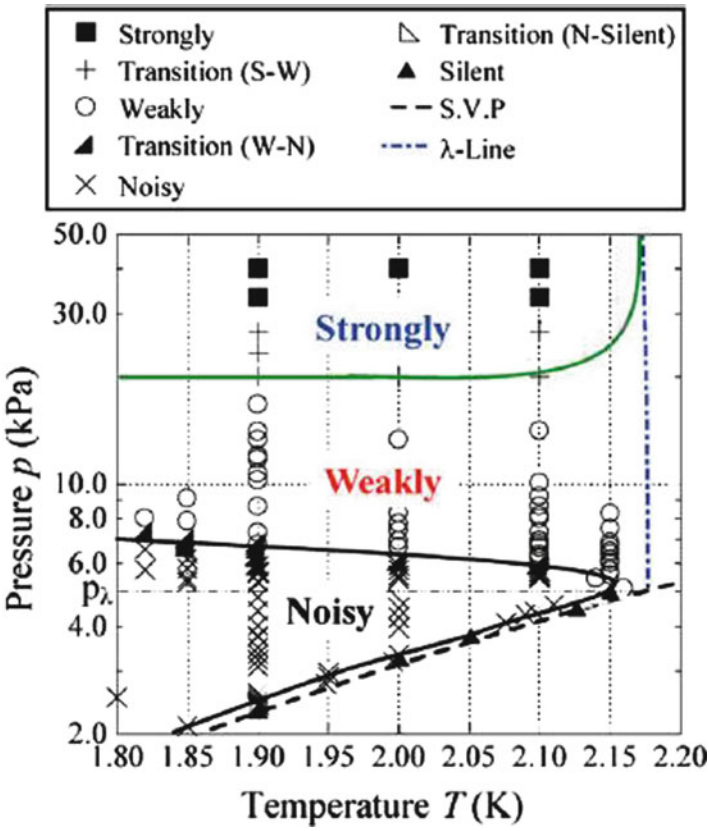

Fig. 7.40 Regimes of noisy and silent boiling from wire heaters in saturated He II. q = 10 W/cm^2 (From Nozawa et al. [76])

Recent experiments performed in saturated and subcooled He II have revealed the existence of four film boiling regimes in He II [76]. These are the two saturated boiling states, noisy and silent boiling and two new subcooled boiling states: strongly and weakly subcooled boiling. A map showing the regime of existence for these four states for a flate heater is given in Fig. 7.40. Note that the strongly and weakly subcooled boiling states only exist at pressures above p_λ.

The existence of the four film boiling states have been confirmed by a variety of measurement techniques including pressure and temperature fluctuations as well as visualization. In particular, Takada et al. [77] performed a series of visualization studies on film boiling on a 50 μm diameter round wire. This work revealed clear differences in the hydrodynamics of boiling as can be seen in Fig. 7.41. Of note is the periodic nature of the film boundary for silent and subcooled boiling states while the noisy boiling is more stochastic. These results can also be used to obtain an average vapor film thickness that can be correlated with the heat transfer coefficient.

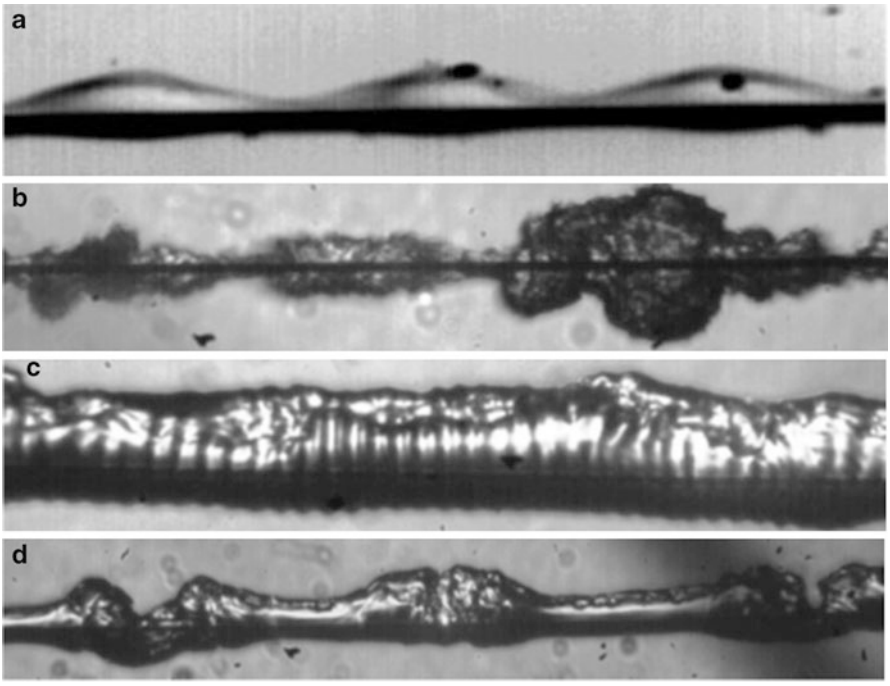

Fig. 7.41 Visualization of four boiling states in He II heat transfer from a round wire: (**a**) silent boiling at 2 K under saturated vapor pressure, q = 19.3 kW/m^2; (**b**) noisy boiling at 2.1 K and 5.3 kPa, q = 373 kW/m^2; (**c**) weakly subcooled boiling at 2.1 K and 16 kPa, q = 601 kW/m^2; (**d**) strongly subcooled boiling at 2.1 K and 100 kPa, q = 396 kW/m^2 (From Takada et al. [77])

We now consider the film boiling heat transfer coefficient. Table 7.5 lists some typical values for h_{fb} under different conditions and for different configurations. There is a notable wide range of values of h_{fb} depending on surface temperature, fluid pressure and heater configuration. However, a few trends are immediately evident from the data in Table 7.5. First, h_{fb} is generally largest for small diameter wires such that there occurs approximately a factor of two increase in value with an order-of-magnitude decrease in heater diameter, d_H. As is discussed below, this behavior can be interpreted in terms of a fairly simple vapor film conduction model. In addition to the diameter dependence, h_{fb} for cylindrical heaters as well as for flat plates is also a function of depth of immersion in the saturated helium or externally applied pressure. Any theoretical effort to model the film boiling heat transfer coefficient therefore must consider these issues.

As mentioned above, the film boiling heat transfer coefficient is seen to depend on diameter in a significant way. Plotted in Fig. 7.42 is typical behavior of h_{fb} for fixed bath temperature and a specific hydrostatic head [72]. The general tendency is for h_{fb} to increase with decreasing diameter. Also, plotted in Fig. 7.43 are typical heat transfer coefficients for heated wires as a function of hydrostatic head h and

Table 7.5 Typical film boiling heat transfer coefficients

Sample	T_b (K)	T_s (K)	Δp (kPa)[a]	h (kW/m^2·K)	References
Wire ($d = 25$ μm)	1.8	150	0.56	2.2	[79]
Wire ($d = 50$ μm)	2.1	80	100	3.6	[77]
	2.1	50	10	6.2	"
Wire ($d = 76$ μm)	1.8	150	0.42	1.1	[79]
Wire ($d = 200$ μm)	2.05	150	0.14	0.66	[74]
Cylinder ($d = 1.45$ mm)	1.78	80	0.06	0.22	[75]
Cylinder ($d = 14.6$ mm)	1.88	40	0.10	0.2	[73]
	2.14	40	0.10	0.2	"
Flat plate					
Flat rectangular plate	1.8	75	0.14	0.22	[72]
(39 mm × 11 mm)	1.8	75	0.28	0.3	"
	1.8	75	0.84	0.55	"
Flat surface ($d = 13.7$ mm)	2.01	40	0.13	0.69	[4]
	2.01	25	0.237	0.98	"

[a]1 kPa = 7.5 torr = 703 mm He II

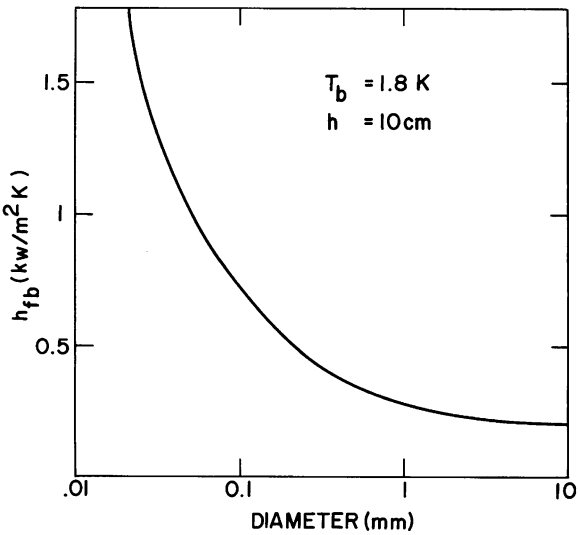

Fig. 7.42 Film boiling heat transfer coefficients as a function of heater diameter for constant hydrostatic head ($h = 10$ cm)

surface temperature, T_s. In general, the heat transfer coefficient increases with helium head and decreases with surface temperature. At small depths, the relationship is roughly linear with h [72].

The situation that occurs in subcooled He II, where the boiling is associated with multiphase phenomena, is generally more complex. In addition, there have been fewer experiments performed under these conditions so data are less prevalent.

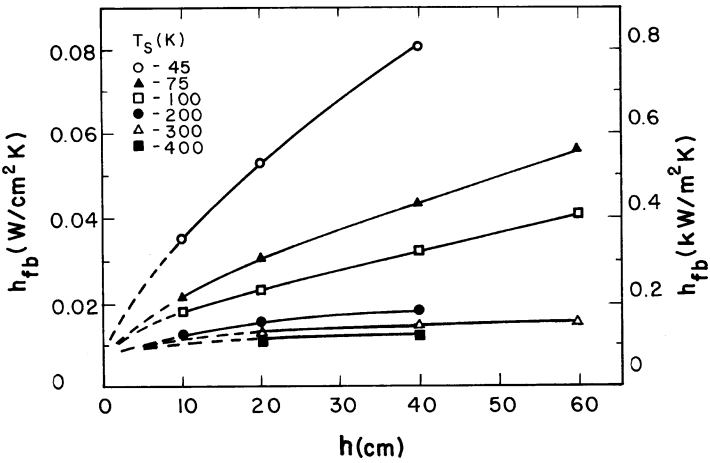

Fig. 7.43 Film boiling heat transfer coefficients versus immersion depth (From Betts and Leonard [72])

However, in general it is observed that the film boiling heat transfer coefficient is higher in the subcooled condition compared to that at saturation. Furthermore, higher pressures on subcooled He II tend to increase h_{fb}. This latter effect may be caused by the increased thermal conductivity of the helium vapor film for higher pressures. Few investigations of the dependence of h_{fb} on heater diameter have been reported for subcooled He II.

7.6.2 *Theoretical Models for Film Boiling Heat Transfer*

A simple model can be constructed to show the origin of the diameter dependence to the film boiling heat transfer. The model is based on an assumption that heat is transported through the vapor film by thermal conduction only. The conceptual picture therefore would represent a stable vapor film of constant thickness δ surrounding the heat transfer surface. Consider a cylindrical heater of radius r as shown in Fig. 7.43. An estimate of the vapor film thickness δ can be obtained from the relationship

$$\delta = \frac{\overline{k}}{h_{fb}} \tag{7.112}$$

where the mean thermal conductivity $\bar{k}$ is taken over the temperature range between the bath T_b and surface T_s. As an example, in Table 7.5 the heat transfer coefficient for a 76 mm diameter wire is about 1.1 kW/m^2 K, obtained for a surface temperature of 150 K. The average thermal conductivity of helium gas in this temperature

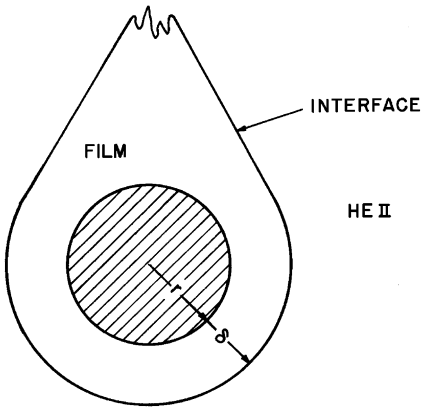

Fig. 7.44 Schematic of cylindrical beater surrounded by a vapor film

range is $\bar{k} \approx 0.06$ W/m K, which corresponds to $\delta \sim 50$ μm. This thickness is fairly large compared to typical heater wire diameter. Also, note that the mean free path in the vapor is of the order of 1 μm, which is much shorter than the film thickness so this thermal conduction model could provide a reasonable approximation.

The simple heat conduction model can be used to interpret the diameter dependence of h_{fb} shown in Fig. 7.42. Making one further assumption that the vapor film thickness does not vary appreciably with heater radius, a relationship can be derived for the ratio of heat transfer coefficients by simply integrating the conduction heat transfer through the film (Fig. 7.44):

$$\left.\frac{h(r)}{h_0}\right|_{fb} = \frac{\delta/r}{\ln(1+\delta/r)} \tag{7.113}$$

where h_0 refers to the film boiling heat transfer coefficients obtained for flat plates. Thus, as the radius of the heater decreases the film boiling heat transfer coefficient is expected to increase purely as a result of radial heat conduction. Generally, such a result is borne out by experiment, see Fig. 7.42.

An alternative model suggested by Takada et al. [77] is based on the steady state heat transport equation in cylindrical coordinates (7.13). The basis of the model is to assume that the heat flux through the surface of the vapor film is equal to the heat conducted through the bulk He II. The stable thickness of the vapor film is then set by the condition that the heat flux in the He II is q^*. Therefore, as the heat generated in the wire increases, the outer radius of the vapor film must increase to limit the heat flux. The thicker film would have a lower average thermal conduction, which would translate to a lower overall heat transfer coefficient. Such a trend can be seen in Fig. 7.43 as the average heat transfer coefficient decreases with increasing heater temperature.

A more detailed theoretical attempt to correlate film boiling heat transfer is due to Rivers and McFadden [78]. This work treats film boiling heat transfer in saturated He II in terms of a boundary layer model. The equations that describe

the problem are conservation of mass, momentum, and energy for two-dimensional, steady-state heat transfer. In rectangular coordinates these equations may be written

$$\frac{\partial u}{\partial x}+\frac{\partial v}{\partial y}=0 \tag{7.114}$$

$$u\frac{\partial u}{\partial x}+v\frac{\partial v}{\partial y}=\frac{1}{\rho_f}F_b+\frac{\mu_f}{\rho_f}\frac{\partial^2 u}{\partial x^2} \tag{7.115}$$

and

$$u\frac{\partial T}{\partial x}+v\frac{\partial T}{\partial y}=\frac{k_f}{\rho_f C_{pf}}\frac{\partial^2 T}{\partial x^2} \tag{7.116}$$

where the body force F_b represents the buoyancy of the vapor film. The solution of this set of equations has been accomplished by assuming fourth-order polynomials for the temperature and velocity profiled and matching boundary conditions at the wall and the vapor–He II interface. The result is a dimensionless form to the Nusselt number,

$$\text{Nu Gr}^{-1/4}=f(Q_b,\text{Gr},H_i,\text{Pr}) \tag{7.117}$$

where the Prandtl number for the film is

$$\text{Pr}=\frac{\mu_f C_{pf}}{k_f} \tag{7.118}$$

and the Grashof number,

$$\text{Gr}=\frac{g\,D^3\rho_f\left(\rho_b-\rho_f\right)}{\mu_f^2} \tag{7.119}$$

describes the heat transfer process. To determine the exact form of (7.117) for a given problem it is necessary to apply numerical integration. The end product of this analysis is a solution for the Nusselt number and steady-state film thickness as a function of the interfacial heat flux. Two regimes become evident in this result. The transition between these two regimes occurs at a value of $Q_b\,\text{Gr}^{-1/4}\approx 1$, where Q_b is the dimensionless interfacial heat flux,

$$Q_b=\frac{Dq_b}{k_f\Delta T_f} \tag{7.120}$$

For values of $Q_b\ \mathrm{Gr}^{-1/4} < 1$, the heat transfer is dominated by convection. In this regime, the heat transfer coefficient is a function of the integral enthalpy which can be normalized to the form

$$H_i = \frac{\Delta h_i}{C_{pf}\Delta T_f} \tag{7.121}$$

For values of $Q_b\ \mathrm{Gr}^{-1/4} > 1$, the heat transfer is via conduction mechanisms. Comparison between experiment and the theory described above is only partially successful.

An alternative approach to the theory of film boiling heat transfer has been suggested by Labuntzov and Ametistov [79]. This theory is based on the idea that film boiling is a nonequilibrium process involving heat and mass transfer at the vapor–He II interface. Thus, it is essential to account for the processes of vaporization and condensation. These processes have been investigated theoretically in detail; the following relationships for the dimensionless fluxes of mass, momentum, and heat have been obtained:

$$\Delta\tilde{p} - 2\sqrt{\pi}\frac{1-0.4\beta}{\beta}\tilde{j} = 0.44\tilde{q} \tag{7.122a}$$

where

$$\Delta\tilde{p} = \frac{p'' - p_s}{p_s} \tag{7.122b}$$

$$\bar{q} = \frac{q}{p_s(2R'T_i)^{1/2}} \tag{7.122c}$$

$$\tilde{j} = \frac{j}{\rho_s(2R'T_i)^{1/2}} \tag{7.122d}$$

In the above equations R' is the gas constant for helium ($R' = R/M = 2{,}079$ J/kg • K), T_i is the temperature of the liquid helium at the interface, β is the condensation coefficient, ρ_s and p_s are the equilibrium density and pressure corresponding to T_i, and p'' is the vapor pressure corresponding to the helium vapor film at the interface. The derivation of (7.122a) is beyond the scope of the present treatment although it is obtained analytically from the Boltzmann kinetic equation [80]. Equation (7.122a) can be applied to the solution of interface mass and heat transfer for ordinary liquids as well as He II. However, for ordinary liquids heat transfer is controlled by convective processes in the bulk. For He II these convective processes are enhanced by two-fluid internal convection which dominates the heat transfer in most cases. The form of (7.122a) is approximate since it is assumed that $\Delta\tilde{P} \ll 1, \tilde{j} \ll 1$. If this is not the case, it is necessary to use the full nonlinear solutions.

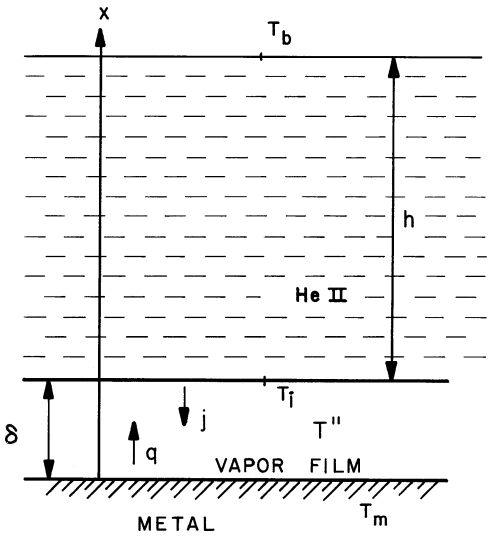

Fig. 7.45 Heat mass transfer process in film boiling He II

Now consider the existence of a film boiling state as shown schematically in Fig. 7.45. In the steady state the vapor film is of constant thickness δ, and consequently $j = 0$. There is no net mass flow across the He II–vapor interface. Under these conditions, (7.122a) can be simplified to

$$\Delta\tilde{p} = 0.44\tilde{q} \tag{7.123}$$

or for a given hydrostatic head

$$q = 2.27\rho gh(2RT_i)^{1/2} \tag{7.124}$$

The physical meaning of (7.124) is that it represents the heat flux necessary to establish a stable vapor film in He II. Note that this is a considerably different interpretation for the critical heat flux than that based on the peak temperature difference within the bulk fluid. Thus, there is some contradiction between the results of Sect. 7.1 and (7.124). There are several possible resolutions for this contradiction.

The first explanation is to imagine conceptually that the film boiling state can be obtained spontaneously anytime the condition described by (7.124) is satisfied. However, this argument is contradictory to experiment, particularly for critical heat fluxes in one-dimensional channels. On the other hand, there is some disagreement between experiment and the He II peak heat flux predicted by turbulent heat transport in cylindrical geometries. It is possible that the condition described by (7.124) is a clue to this discrepancy; however, this point has yet to be analyzed.

As an alternate explanation [80], it is to suggest that the film boiling state once established obeys the kinetic relationship derived above. This idea is not contradictory to the peak heat flux being the point where the helium temperature near the

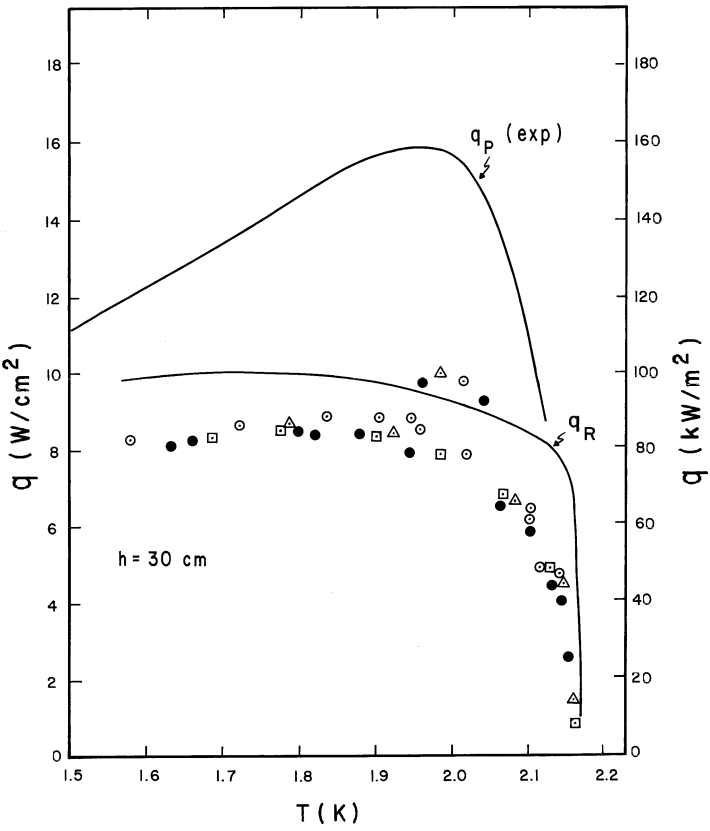

Fig. 7.46 Comparison of calculations using the kinetic theory with experimental results (From Kryukov and Van Sciver [81])

interface reaches T_{sat} or T_λ. However, once this film is established it will remain stable against collapse until the heat flux falls below the value given by (7.124), provided it is less than the applied heat flux. Thought of in this manner, the molecular kinetic theory provides a mechanism of interpreting the minimum film boiling heat flux in He II, that is q_R.

The connection between these two alternate concepts for recovery from film boiling has been investigated analytically for heated cylinders in saturated He II. The comparison of this model with experiment has been carried out for the few configurations where minimum film boiling heat flux data are available [81]. The best agreement occurs with data acquired on small-diameter wires. Plotted in Fig. 7.46 are the experimentally measured peak and minimum film boiling heat fluxes versus temperature for a cylindrical wire of diameter 76.2 μm [82]. The theoretical plot for q_R is also shown to provide quite close agreement with experiment. Unfortunately, the correspondence between theory and experiment for other

configurations of larger dimension is not nearly as close. Consequently, there is still considerable disagreement as to the correct mechanism needed to describe the film boiling state in He II.

An alternate approach for the recovery from the film boiling state has been suggested by experiments that have shown a correlation between the minimum film boiling heat flux and the film boiling heat transfer coefficient. For a specific configuration consisting of a flat plate at the end of a duct, the value of q_R was shown to increase monotonically with h_{fb}. This condition was observed to prevail in both saturated and subcooled He II. Furthermore, the ratio q_R/h_{fb} was found to take on an essentially constant value of about 23 K, suggesting the existence of a critical temperature difference for recovery from film boiling. This critical temperature difference should be related in some fundamental way to the collapse of the vapor film.

7.6.3 Transient Film Boiling Heat Transfer

Typically, the heat transfer process to He II is transient in nature with associated time dependent phenomena. This occurs when film boiling is caused by a rapid transient disturbance such as might happen when a superconducting magnet quenches or a He II cryostat has a loss of vacuum accident. Understanding the heat transfer in this regime is helpful with the design and safe operation of large scale He II systems.

We consider the case where film boiling has been established by exceeding the critical heat flux followed by a reduction of the heat flux to some lower value. If the heat flux is reduced below the minimum film boiling flux q_R, recovery to the nonboiling state should begin. This dynamic process is governed by transient heat transfer within the system.

We first consider the time dependent recovery from the film boiling state. It is assumed that at time $t = 0$ the film boiling state is initiated and that a steady heat rate Q is applied for a time Δt_f. Since Q is greater than the peak heat flux, the temperature of the surface will increase dependent on the mass and heat capacity of the heated section. For long times, this process would lead to a steady temperature based on the balance between the heat rate and film boiling heat transfer. After Δt_f, the heat generation ceases ($Q = 0$) and the recovery process begins. Empirically, the recovery process is found to take a length of time Δt_R which is a function of Δt_f before the vapor film collapses [83]. It is assumed further that the controlling mechanism for recovery is the enthalpy stored within the heated sample and the film boiling heat transfer coefficient is a constant, h. The fluid simply acts as a constant temperature bath. Using the Debye approximation to the specific heat, we can show that the above assumptions lead to a correlation between Δt_f and Δt_R which can be written explicitly as

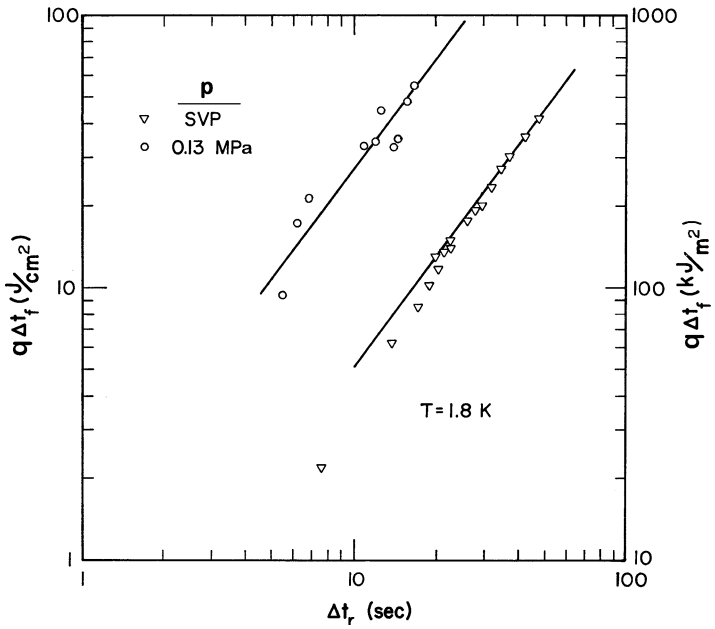

Fig. 7.47 Correlation between the energy applied to a film boiling heat transfer sample and the time to recovery

$$Q\Delta t_f = 0.176\Theta_D \left(\frac{M}{mR}\right)^{1/3} (hA\Delta t_R)^{4/3} \left(1 + \frac{4}{5}\alpha + \frac{4}{6}\alpha^2 + \ldots\right) \tag{7.125}$$

where $\alpha = hT_m/Q \leq 1$ with T_m being the maximum temperature of the heat transfer surface. The total mass of the heat transfer sample is m and its cooled surface has area A. The properties of the heat transfer sample enter through its molecular weight M and Debye temperature Θ_D.

The correlation suggested by (7.125) has shown reasonable agreement with experiment. By allowing the heat transfer coefficient h to be a constant adjustable parameter, one can fit experimental data for the relationship between Δt_f and Δt_R. This fit is shown in Fig. 7.47. By establishing the correlation based on only the leading term in (7.125), the best-fit heat transfer coefficients are $h = 0.18$ kW/m^2 K at SVP and $h = 0.62$ kW/m^2 K at 0.13 MPa. It is interesting to note that these values of h are roughly 60% of typical steady-state film boiling heat transfer coefficients for flat plates.

The other problem of interest is to the understand transient recovery in subcooled He II. This problem has more to do with the time-dependent heat transport in the bulk fluid than film boiling heat transfer. Rather than correlating the time to recovery based on the thermal capacity of the heater, the approach here is to determine the maximum steady-state heat flux which allows recovery after an intense short-duration heat pulse is applied to a heat transfer sample. The short-duration heat pulse is assumed to be larger than the maximum energy flux to locally

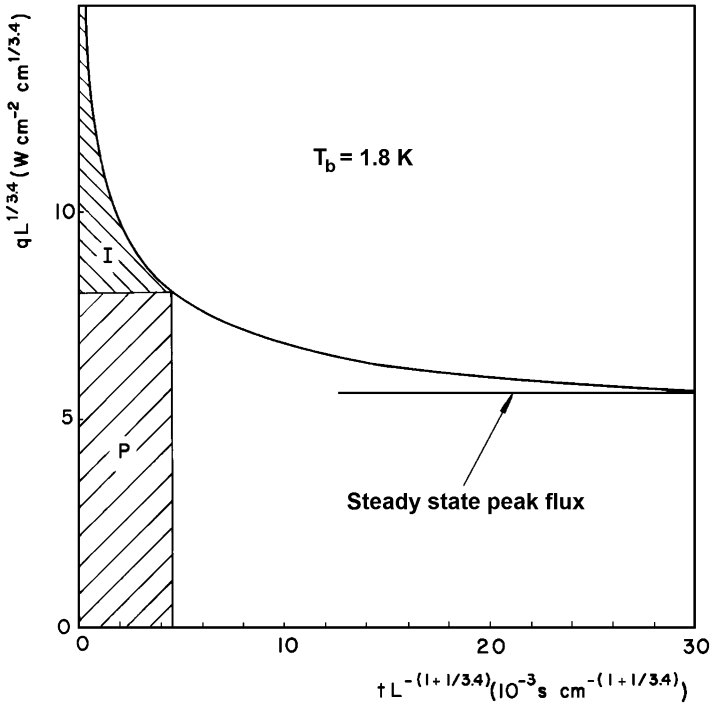

Fig. 7.48 Schematic description of the transient recovery process in He II with post-heating (From Seyfert [30])

bring the He II to T_λ and thus break down heat transfer. Consequently, the heat transfer at the solid-helium interface breaks down and further heat is stored in the solid or in the helium adjacent to the heater. After the heat pulse, the excess heat can be transferred through the He II by the established transient heat transfer mechanisms. Now if the steady-state heat flux is not too large, the combination of it with the remaining excess energy being released from the heat transfer sample will not exceed the maximum transient energy flux in the He II. The result is a temporary recovery to the non-boiling state. Recovery is temporary only if the steady-state heat flux is larger than the maximum steady-state heat flux in He II for that particular configuration.

The above set of conditions are illustrated graphically in Fig. 7.48, which is a normalized transient heat transfer plot for He II at 1.8 K. The solid curve represents the maximum heat flux that can be applied for a given time before breakdown of He II heat transfer occurs. This condition is established according to Sect. 7.2. Now consider a short-duration, high-level heat pulse applied to the heat transfer sample. Since this energy is larger than that transferable by the He II, the excess is stored in the heat transfer sample. The total energy contained in the pulse is shown by region I in the figure. Subsequent to the pulse, the heat flux is dropped to a lower level q_p which is still above the maximum steady-state meat flux q^*. However, temporary recovery will occur because the transient heat transfer mechanism can continue.

Thus, the sum of the two areas I and P determines the length of time before unrecoverable thermal breakdown occurs. This model has been compared successfully to transient heat transfer experiments in He II [60]. The problem is of significant practical interest to superconducting magnet technology.

Example 7.4

For the rectangular flat plate film boiling heat transfer data at T = 1.8 K and Δp = 0.14 kPa in Table 7.5, estimate the thickness of the vapor film assuming that heat is carried only by gaseous conduction. Compare the calculated thickness to the mean free path in the vapor.

In this case, the average thermal conductivity can be approximated by$k_{He}(40)$K = 0.4W/m K. The approximate thickness of the film is then,

$$t = \bar{k}/h_{fb} = 0.4 \text{ W/m K}/220 \text{ W/m}^2 \text{ K} = 2 \text{ mm}$$

The mean free path is calculated by
The mean free path is calculated by,

$$l \approx \frac{1}{n\sigma} \sim \frac{k_B T}{\pi d^2 p} = \frac{1.38 \times 10^{-23} J/K \times 40K}{\pi\left(2.56 \times 10^{-10} m\right)^2 \times 1600 Pa} = 1.67 \ \ \mu\text{m}$$

Questions

1. Heat transfer from a solid surface to a bath of He II does not have a nucleate boiling regime. Why?
2. One method to increase the heat transfer coefficient in the Kapitza regime would be to roughen the surface, thereby increasing the effective area. What are the practical limits to this approach? [Two points to keep in mind are that the surface material has a finite thermal conductivity and the phonon coupling is over a certain range.]
3. Assume that you wish to design a He II heat exchanger that consists of a U-tube immersed in a pressurized He II reservoir. The upper ends of the tube empty into a saturated bath of He II maintained at a constant 1.7 K. For these conditions, draw a sketch of the temperature profile along the U-tube from one end to the other.
4. For Question 3 above, suppose that you wanted to enhance the performance of the heat exchanger. Would there be a benefit to putting a pump in the line to force the He II through the U-tube. List the design constraints on selecting the parameters for the circulation system.

Problems

1. Consider a sphere of radius r_0 in a large bath of He II. Derive an expression for the steady-state temperature gradient as a function of radial coordinate r.

Determine the peak heat flux as it depends on bath temperature. Assume that mutual friction is the only important interaction and the ambient pressure is 0.1 MPa. [Hint: This problem is analogous to that of heat transfer in cylindrical geometries discussed in Sect. 7.1.4.]

2. Estimate the maximum surface heat flux q_0 for a cylindrical wire of diameter 1 mm in He II at 1.8 K, 0.1 MPa. What would be the effect of increasing the external pressure to 1 MPa?
3. Show that the transient heat transfer solution given by (7.52) for the fixed energy deposition obeys the heat conductivity equation for He II.
4. Estimate the Kapitza conductance at 1.9 K of aluminum for small ΔT, by each of the following methods:

   a. Phonon radiation limit.
   b. Acoustic mismatch theory.
   c. Experimental results listed in Table 7.3.

5. Show that the variation of the film boiling heat transfer coefficient with heater radius may be written in the form given by (7.113). For the data listed in Table 7.5 from Ref. [79] (d = 25 and 76 μm), estimate the film thickness δ and the limiting heat transfer coefficient h_0 for large radii.
6. A metallic copper heater is located at the bottom of a 50 cm long vertical channel containing He II at 1.9 K. Assume the pressure at the top of the channel is saturation and that heat flow is governed by mutual friction.

   a. Find the peak heat flux q^*. [Note: Although (7.10) is valid for this case, it is more accurate to use tabulated vapor pressure of helium].
   b. Estimate the heater surface temperature just below q^*.

7. Consider a 2 m long, 5 mm ID smooth tube which contains 1.8 K He II flowing at a mass flow rate of 20 gm/s. Calculate the total pressure drop across the tube assuming the flow is fully developed and turbulent. Estimate the total temperature rise in the He II flow due to the Joule Thomson effect. [Hint: you may use the simplified form for the JT coefficient of an incompressible liquid].
8. Derive (7.84) for the mass flow through an ideal vapor – He II phase separator.

References

1. W. F. Vinen, Mutual Friction in a Heat Current in Liquid Helium II. I. Experiments on Steady State Heat Currents, *Proc. R. Soc. London* **A240**, 114 (1957).
2. V. Arp, Heat Transport through Helium II, *Cryogenics* **10**, 96 (1970).
3. C. E. Chase, Thermal Conduction in Liquid Helium II I: Temperature Dependence, *Phys. Rev.* **Vol. 127**, 361 (1962).
4. S. W. Van Sciver, Kapitza Conductance of Aluminum and Heat Transport through Sub-cooled He II, *Cryogenics* **18**, 521 (1978).
5. G. Bon Mardion, et al, Steady State Heat Transport in Superfluid Helium at 1 Bar, *Proc. 20th Intern. Cryog. Engn. Conf.*, IPC Technology Press, London (1978) pp. 214–222.

6. W. F. Vinen, Mutual Friction in a Heat Current in Liquid Helium II. III. Theory of Mutual Friction, *Proc. R. Soc. London* **A242**, 493 (1957).
7. A. Sato, et al, Normalized Representation for Steady State Heat Transport in a Channel Containing He II Covering Pressure Range up to 1.5 MPa, *Proc. 7th Intern. Cryog. Engn. Conf.*, Beijing, China (2004) pp. 849–52.
8. A. Sato, et al, Steady State Heat Transport in a Channel Containing He II at High Pressures up to 1.5 MPa, *Adv. Cryog. Engn.* **Vol. 49**, 999 (2004).
9. A. Sato, et al, Temperature Dependence of the Gorter-Mellink Exponent *m* Measured in a Channel Containing He II, *Adv. Cryog. Engn.* **Vol. 51A**, 387 (2006).
10. M. Maeda, et al, Heat Transport Near the Lambda Line in a Channel Containing He II, *Adv. Cryog. Engn.* **Vol. 51A**, 379 (2006).
11. P. Seyfert, Practical Results on Heat Transfer to Superfluid Helium, in *Stability of Superconductors*, pp. 53–62, International Institute of Refrigeration Commission A 1/2, Saclay, France, 1981.
12. C. Linnet and T. H. K. Frederking, Thermal Conditions at the Gorter-Mellink Counterflow Limit between 0.01 and 3 Bar, *J. Low Temp. Phys.* **Vol. 21**, 447 (1975).
13. S. R. Breon and S. W. Van Sciver, Boiling in Subcooled and Saturated He II, Advances in Cryogenic Engineering **31**, 465 (1986) and Boiling Phenomena in Pressurized He II Confined to a Channel, *Cryogenics* **26**, 682 (1986).
14. A. C. Leonard and M. A. Clermont, Correlation of the Vaporization Onset Heat Flux for Cylinders in Saturated Liquid Helium II, in *Proc. 4th Intern. Cryog. Engn. Conf.*, IPC Science and Technology Press, London, 1972, pp. 301–306.
15. J. S. Goodlang and R. K. Irey, Nonboiling and Film Boiling Heat Transfer to a Saturated Bath of Liquid Helium, *Adv. Cryog. Eng.* **14**, 159 (1969).
16. T. H. K. Frederking and R. L. Haben, Maximum Low Temperature Dissipation Rates of Single Horizontal Cylinders in Liquid Helium II, *Cryogenics* **8**, 32 (1968).
17. S. W. Van Sciver and R. L. Lee, Heat Transfer to He II in Cylindrical Geometries, *Adv. Cryog. Eng.* **25**, 363 (1980).
18. S. W. Van Sciver and R. L. Lee, Heat Transfer from Circular Cylinders in He II, in *Cryogenic Processes and Equipment in Energy Systems*, ASME Publication No. H00164, 1981, pp. 147–154.
19. S.W. Van Sciver, Heat Transfer through Extended Surfaces Containing He II, *ASME Journal of Heat Transfer* **Vol. 121**, 142 (1999).
20. A. Bezaguet, J. Casas-Cubillos, P. Lebrun, M. Marquet, L. Tavian, and R. van Weelderen, The superfluid helium model cryoloop for the CERN Large Hadron Collider, *Adv. Cryog. Engr.* **Vol. 39**, 649 (1994).
21. G. Horlitz, T. Peterson and D. Trines, A 2 Kelvin Helium II Distributed Cooling System for the 2x250 Gev e + e- Linear Collider TESLA, *Cryogenics* **Vol. 34** (Supplement), 131 (1994).
22. S. W. Van Sciver, Heat and Mass Transfer Processes in Two Phase He II/Vapor, *Cryogenics* **Vol. 39**, 1039 (1999).
23. Y. Xiang, B. Peterson, S. Wolff, S. W. Van Sciver , and J. G. Weisend II, Numerical Study of Two-Phase Helium II Stratified Channel Flow with Inclination, *IEEE Trans. On Applied Superconductivity* **Vol. 10**, 1530 (2000) and Y. Xiang, N. N. Filina, S. W. Van Sciver, J. G. Weisend II and S. Wolff, Numerical Study of Two-Phase He II Stratified Channel Flow, *Adv. Cryog. Engn.* **Vol. 45B**, 1001 (2000).
24. Ph. Lebrun, L. Serio, L. Tavian and R. van Weelderen, Cooling Strings of Superconducting Devices Below 2 K: the Helium II Bayonet Heat Exchanger, *Adv. Cryog. Engn.* **Vol. 43A,** 419 (1998).
25. B. Rousset, L. Grimaud, A. Gauthier, Stratified Two-Phase Superfluid Helium Flow: I*Cryogenics* **Vol. 37**, 733 (1997) and L. Grimaud, A. Gauthier, B. Rousset, J. M. Delhaye, Stratified Two-Phase Superfluid Helium Flow: II, *Cryogenics* **Vol. 37**, 739 (1997).
26. L. Dresner, Transient Heat Transfer in Superfluid Helium, *Adv. Cryog. Eng.* **27**, 411 (1982).

27. L. Dresner, Transient Heat Transfer in Superfluid Helium-Part II, *Adv. Cryog. Eng.* **29**, 323 (1984).
28. L. Dresner, *Similarity Solution of Non-Linear Partial Differential Equations*, Pitman Publishing, Boston, MA, 1983.
29. S. W. Van Sciver, Transient Heat Transport in He II, *Cryogenics* **19**, 385 (1979).
30. P. Seyfert, J. Lafferranderie, and G. Claudet, Time Dependent Heat Transport in Subcooled Superfluid Helium, *Cryogenics* **22**, 401 (1982).
31. S. W. Van Sciver, Heat Transport in Forced Flow He II: Analytic Solution, *Adv. Cryog. Eng.* **29**, 315 (1984).
32. R. Srinvasan and A. Hofmann, Investigations on Cooling with Forced Flow of He II, *Cryogenics* **25**, 641 (1985).
33. A. Kashani and S. W. Van Sciver, Steady State Forced Convection Heat Transfer in He II, *Adv. Cryog.* Eng. **31**, (1986).
34. W. W. Johnson and M. C. Jones, Measurements of Axial Heat Transport in Helium II with Forced Convection, *Adv. Cryog. Eng.* **23**, 363 (1978).
35. S. Fuzier and S. W. Van Sciver, Steady-State Pressure Drop and Heat Transfer in He II Forced Flow at High Reynolds Number, *Cryogenics* **41**, 453 (2001) and S. Fuzier, S. Maier and S. W. Van Sciver, Pressure Drop in Forced Flow He II at High Reynolds Numbers, in *Proc. 19th Intern. Cryog. Engn. Conf.*, Grenoble, France July, 15, 2002, pp. 755–8.
36. P.L. Walstrom, J.G. Weisend II, J.R. Maddocks, and S.W. Van Sciver, Turbulent Flow Pressure Drop in Various He II Transfer System Components, *Cryogenics* **Vol. 28**, 101 (1988).
37. M.A. Daughterty and S.W. Van Sciver, Pressure Drop Measurements on Cable-in-Conduit Conductors of Various Geometries, *IEEE Trans. on Magnetics* **27**, 2108 (1991).
38. A. Hofmann, A. Khalil and H.P. Kramer, Operational Characteristics of Loops, *Adv. Cryog. Engn.* **33**, 471 (1988).
39. B. Rousset, G. Claudet, A. Gauthier, P. Seyfert, P. Lebrun , M. Marquet , R. Van Weelderen and J. Duchateau, Operation of a Forced Flow Superfluid Helium Test Facility and First Results, *Cryogenics (Supplement)* **Vol. 3,** 134 (1992).
40. P. L. Walstrom, Joule-Thomson Effect and Internal Convection Heat Transfer in Turbulent He II Flow, *Cryogenics* **Vol. 28**, 151 (1988).
41. A. Kashani, S.W. Van Sciver, and J.C. Strikwerda, Numerical Solution of Forced Convection Heat Transfer in He II, *J. Num Heat Transfer*, *Part A*, **Vol. 16**, 213 (1989).
42. L. Bottura and C. Rosso, Finite Element Simulation of Steady-State and Transient Forced Convection in Superfluid Helium, *Intern. J. Numerical Methods in Fluids*, **Vol. 30**, 1091 (1999).
43. Rousset B., Claudet G., Gauthier A., Seyfert P., Martinez A., Lebrun P., Marquet M. and Van Weelderen R., Pressure Drop and Transient Heat Transport in Forced Flow Single Phase Helium II at High Reynolds Numbers, *Cryogenics (Supplement)* **Vol. 34**, 317 (1994).
44. S. Fuzier and S. W. Van Sciver, Experimental Measurements and Modeling of Transient Heat Transfer in Forced Flow He II at High Velocities, *Cryogenics* **Vol. 48**, 130 (2008).
45. R. Maekawa and B. Baudouy, Heat Transfer through Porous Media in the Counterflow Regime, *Adv. Cryog. Engn.* **Vol. 41**, 983 (2004).
46. M. Dalban-Canassy and S. W. Van Sciver, Steady Counterflow He II Heat Transfer Through Porous Media , *Adv. Cryog. Engn.* **Vol. 55**, 1327 (2010).
47. B. Baudouy, et al, Heat Transfer through Porous Media in Static Superfluid Helium, *Adv. Cryog. Engn.* **Vol. 51**, 409 (2006).
48. B. Maytal, J. A. Nissen and S. W. Van Sciver, Iso-chemical Trajectories in the P-T Plane for He II, *Cryogenics* **Vol. 30**, 730 (1990).
49. P. Kittel, Losses in Fountain Effect Pumps, in *Proc. 11th Intern. Cryog. Engn. Conf.*, Butterworth, UK (1986) pp. 317–322.
50. A.R. Urbach, J. Vorreiter and P. Mason, Design of a Superfluid Helium Dewar for the IRAS Telescope, in *Proc. 7th Intern. Cryog. Engn. Conf.*, IPC Science and Technology Press, UK (1978) pp. 126–133.

51. D. Petrac and P. V. Mason, Evaluation of Porous-Plug Liquid Separators for Space Helium Systems, in *Proc. 7th Intern. Cryog. Engn. Conf.*, IPC Science and Technology Press, UK (1978) pp. 120–5.
52. P. L. Kapitza, The Study of Heat Transfer on Helium II, *J. Phys. (USSR)* **4**, 181 (1941).
53. T. H. K. Frederking, Thermal Transport Phenomena at Liquid Helium II Temperatures, *Adv. Cryog. Heat Transfer* **64**, 21 (1968).
54. N. S. Snyder, Heat Transport through Helium II: Kapitza Conductance, *Cryogenics* **Vol. 10**, 89 (1970).
55. L. J. Challis, Experimental Evidence for a Dependence of the Kapitza Conductance on the Debye Temperature of a Solid, *Phys. Lett.* **26A**, 105 (1968).
56. M. Khalatnikov, *Introduction to the Theory of Superfluidity*, Chap. 111, W. A. Benjamin, New York, 1965.
57. R. E. Peterson and A. C. Anderson, The Kapitza Thermal Boundary Resistance, *J. Low Temp. Phys.* **11**, 639 (1973).
58. L. J. Challis, K. Dransfeld, and J. Wilks, Heat Transfer Between Solids and Liquid Helium II, *Proc. R. Soc. London* **A260**, 31 (1961).
59. D. Cheeke and H. Ettinger, Macroscopic Calculation of the Kapitza Resistance Between Solids and Liquid ^{4}He, *Phys. Rev. Lett.* **37**, 1625 (1976).
60. P. H. E. Meijer and J. S. R. Pert, New Kapitza Heat Transfer Model for Liquid ^{4}He, *Phys. Rev. B* **22**, 195 (1980).
61. J. Wilks, *The Properties of Liquid and Solid Helium*, Chap. 14, Clarendon Press, Oxford, 1967.
62. B. W. Clement and T. H. K. Frederking, Thermal Boundary Resistance and Related Peak Flux During Supercritical Heat Transport from a Horizontal Surface Through a Short Tube to a Saturated Bath of Liquid Helium II, *Liquid Helium Technology, Proceedings of the International Institute of Refrigeration*, Commission I, Boulder, CO, Pergamon Press, Oxford, 1966, pp. 49–59 (see also Ref. 29).
63. K. Mittag, Kapitza Conductance and Thermal Conductivity of Copper, Niobium, and Aluminum in the Range from 1.3 to 2.1 K, *Cryogenics* **13**, 94 (1973).
64. S. W. Van Sciver, Kapitza Conductance of Aluminum and Heat Transport from a Flat Surface through a Large Diameter Tube to Saturated He II, *Adv. Cryog. Eng.* **23**, 340 (1977).
65. G. Claudet and P. Seyfert, Bath Cooling with Subcooled Superfluid Helium, *Adv. Cryog. Eng.* **27**, 441 (1981).
66. S. W. Van Sciver, Developments in He II Heat Transfer and Applications to Superconducting Magnets, *Adv. Cryog. Eng.* **27**, 375 (1981).
67. A. Kashani and S. W. Van Sciver, Kapitza Conductance of Technical Copper with Several Different Surface Preparations, *Cryogenics* **25**, 238 (1985).
68. H. P. Kramer, Heat Transfer to Forced Flow Helium II, in *Proc. 12th Intern. Cryog. Engn. Conf.*, Southampton, UK, Butterworth, UK, 1988, pp. 299–304.
69. J. G. Weisend II and S. W. Van Sciver, Surface Heat Transfer Measurements in Forced Flow He II, in *Superfluid Helium Heat Transfer*, ASME HTD-Vol. 134 ed. J. P. Kelly and W. J Schneider, 1990, pp 1–7.
70. A. C. Leonard, Helium I Noise Film Boiling and Silent Film Boiling Heat Transfer Coefficient Values, in *Proc. 3rd Intern. Cryog. Engn. Conf.*, pp. 109–114, ILIFFE Science and Tech. Publications, Guilderford, Surrey, U.K., 1970.
71. R. K. Irey, Heat Transport in Liquid Helium II, in *Heat Transfer at Low Temperatures*, W. Frost (Ed.), Plenum Press, New York, 1975.
72. K. R. Betts and A. C. Leonard, Free Convection Film Boiling from a Flat, Horizontal Surface in Saturated He II, *Adv. Cryog. Eng.* **21**, 282 (1975).
73. J. S. Goodling and R. K. Irey, Non-Boiling and Film Boiling Heat Transfer to a Saturated Bath of Liquid Helium, *Adv. Cryog. Eng.* **14**, 159 (1969).
74. R. C. Steed and R. K. Irey, Correlation of the Depth Effect on Film Boiling Heat Transfer in Liquid Helium I, *Adv. Cryog. Eng.* **15**, 299 (1970).

75. R. M. Holdredge and P. W. McFadden, Boiling Heat Transfer from Cylinders in Super-fluid Liquid Helium II Bath, *Adv. Cryog. Eng*. **11**, 507 (1966).
76. M. Nozawa, N. Kimura, M. Murakami and S. Takada, Thermo-fluid Dynamics of Several Film Boiling Modes in He II in the Pressure Range between Atmospheric Pressure and Saturated Vapor Pressure, *Cryogenics* **Vol. 49**, 583 (209).
77. S. Takada, M. Murakami, and N. Kimura, Heat Transfer Characteristics of Four Film Boiling Modes Around a Horizontal Cylindrical Heater in He II, *Adv. Cryog. Engn.* Vol. 55A, 1355 (2010).
78. W. J. Rivers and P. W. McFadden, Film-Free Convection in Helium II, *Trans. ASME, J. Heat Transfer*, **88C**, 343 (1966).
79. D. A. Labuntzov and Ye. V. Ametistov, Analysis of Helium II Film Boiling, *Cryogenics* **19**, 401 (1979).
80. P. L. Bhatnager, E. P. Gross, and M. Krook, A Model for Collision Processes in Gases. I. Small-Amplitude Processes in Charged and Neutral One-Component Systems, *Phys. Rev*. **94**, 511 (1954).
81. A. P. Kryukov and S. W. Van Sciver, Calculation of the Recovery Heat Flux from Film Boiling in Superfluid Helium, *Cryogenics* **21**, 525 (1981).
82. G. D. Lemieux and A. C. Leonard, Maximum and Minimum Heat Flux in Helium II for a 76.2 μm Diameter Horizontal Wire at Depths of Immersion Up to 70 cm, *Adv. Cryog. Eng*. **13**, 624 (1968).
83. S. W. Van Sciver, Correlation of Time Dependent Recovery from Film Boiling Heat Transfer in He II, *Cryogenics* **21**, 529 (1981).

Further Readings

F. P. Incropera and D. P. Dewitt, *Fundamentals of Heat Transfer*, Wiley, New York, 1981.
G. E. Myers, *Analytical Methods in Conduction Heat Transfer*, McGraw-Hill, New York, 1971.
S. W. Van Sciver, He II (Superfluid Helium), Chapter 10 in *Handbook of Cryogenic Engineering*, ed. J. G. Weisend II, Taylor & Francis, Washington, DC (1998), pp. 445–483.
J. Wilks, *The Properties of Liquid and Solid Helium*, Chap. 14, Clarendon Press, Oxford, 1967.